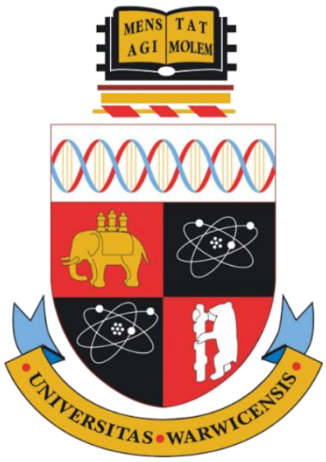

Photoelectric Processes in Ferroelectric/Multiferroic Materials

by

Mingmin Yang

Thesis

Submitted to the University of Warwick

For the degree of

Doctor of Philosophy

Department of Physics

January 2018

To my family, especially my wife and our new born baby Yiyi.

Contents

Acknowledgements

I would first like to thank Prof. Marin Alexe for giving me the opportunity to initiate my PhD in his group at the University of Warwick and for introducing me into the field of ferroelectric semiconductors. The present thesis might not be possible without his expert guidance and generous support. I am so fortunate to work in such a group that independence and innovation are so emphasised that cultivate me to be a creative researcher. The knowledge, skills and the attitude taught by him in the last three years would definitely guide me in my future career.

I also would like to thank Dr. Akash Bhatnagar who guided my research work in the early stage of my PhD. Talking and discussion with him about life and science was of great fun and of course, beneficial. I am grateful to Dr. Dong-Jik Kim for the cooperation and discussion of our nice work regarding the flexo-photovoltaic effect. I want to mention here my friends and colleagues including Zhengdong Luo, Alan Brunier, Dr. Geanina Apachitei, Dr. Deasung Park, Dr. Haiyuan Wang for giving a great company within work and warm friendship during the PhD journey. It is also lucky to have Michael Crosbie as technician in our group who builds, repairs and improves our research facilities. My research life would be harder without his supports. I wish all of you a happy life and successful career.

I also appreciate the time and effort put into training and discussion by Dr. David Walker (XRD), Mark Crouch (cleaning room and equipment therein). Also I would like acknowledge the help from administrative staff in Physics Department and financial support from University of Warwick.

At last, I would like to express my deep gratitude to my dear wife Danqing for giving me a home and having our first baby. Without you, my life in UK would be nothing but lonely and boring. I am also grateful to my parents, my father and mother in law, my sister for their extensive support, care and encouragement. I love you all.

Declarations

I declare the content of this thesis is my own work except where stated otherwise. The research reported here has not been previously submitted, either fully or in part, for admission to a higher degree.

The $BiFeO_3$ single crystals studied in Chapter 4 were grown by Prof. Marin Alexe at Max Planck Institute for Microstructure Physics in Halle Germany. All the $BiFeO_3$ thin films were fabricated by pulsed laser deposition at the University of Warwick as well as all the structural and electronic characterization. The strain and strain gradient calculation presented in Chapter 8 was performed by Dr. Dong-Jik Kim. All the other data and interpretation have been carried out by the author

Mingmin Yang

January 2018

Several articles based on this research have been published or have been submitted for publication:

1. **Mingmin Yang**, Akash Bhatnagar and Marin Alexe, Electronic Origin and Tailoring of Photovoltaic Effect in $BiFeO_3$ Single Crystals, *Adv. Electron. Mater*.**1**, 1500139(2015).

2. **Ming-Min Yang**, Zheng-Dong Luo, Dong Jik Kim and Marin Alexe, Bulk Photovoltaic Effect in Monodomain $BiFeO_3$ Thin Films, *Appl. Phys. Lett*. **110**, 183902(2017).

3. **Ming-Min Yang**, Akash Bhatnagar, Zheng-Dong Luo & Marin Alexe, Enhancement of Local Photovoltaic Current at Ferroelectric Domain Walls in $BiFeO_3$, *Sci. Rep.* **7**, 43070(2017).

4. **Ming-Min Yang** and Marin Alexe, Light-induced Reversible Control of Ferroelectric Polarisation in $BiFeO_3$, *Adv. Mater.*1704908 (2018)

5. **Ming-Min Yang**, Dong-Jik Kim and Marin Alexe, Flexo-Photovoltaic Effect, *Science* aan3256 (2018).

Abstract

Photoferroelectrics, which is defined as the interaction of ferroelectric materials with light, has attracted renewed attention recently and emerged as a topic of both fundamental interest and technological importance. It not only provides potential applications in sensors and photovoltaic devices but also offers a fertile playground to gain insight into the physics of ferroelectricity. As a prominent example, the bulk photovoltaic effect manifested in the ferroelectric materials under illumination gives rise to an anomalous open-circuit photovoltage exceeding the bandgap as well as a light polarisation-dependent photocurrent, offering an alternative approach to boost the solar energy conversion efficiency. Although it has been established for decades, the field is still in its fancy and many fundamental issues remain to be resolved to fully exploit its potential.

In the first part of this thesis, we focus on the photoelectric processes in the bulk photovoltaic effect of bismuth ferrite to unravel respectively the essential role of the sub-bandgap levels, its correlation with ferroelectric polarization and role of domain walls in conduction of photovoltaic current. Results demonstrate the sub-bandgap levels is at the electronic origin of the bulk photovoltaic effect in bismuth ferrite. The activity of the sub-bandgap levels in the photoelectric processes can be effectively utilized to tailor the ferroelectric photovoltaic performance. Also, contrary to the common intuition, we prove the independence of the bulk photovoltaic effect on the ferroelectric polarization. We also found that the ferroelectric domain walls can facilitate the conduction and collection of the photocurrent originated in the bulk photovoltaic effect despite its adverse effect on the photovoltage.

Inspired by the abundant phenomena in the photoferroelectric field, we explored the light-induced reversible manipulation of the ferroelectric polarization in a deterministic way. This interesting issue is successfully addressed in this thesis by utilizing a combination of the bulk photovoltaic effect and a nanoscale electrode. The collection of photocurrent by an atomic force microscope tip generates a giant electric field locally, enabling ferroelectric switching. By tuning the direction of the photocurrent via either illumination areas or light polarization, the ferroelectric polarization can be reversibly controlled.

At the last part of the thesis, we creatively generalised the bulk photovoltaic effect, which was originally constrained to the non-centrosymmetric materials, to a universal effect allowed in all the semiconductors irrespective of their symmetry by the mediation of the flexoelectric effect. This new photovoltaic effect, termed as flexo-photovoltaic effect, may offer a new mechanism to enhance solar cell efficiency. The research works studied in this thesis not only provide fundamental insights into the interactions of ferroelectrics with light but also largely expand the scope of photoferroelectrics into centrosymmetric materials.

Abbreviations

APV	Anomalous Photovoltaic Effect
BPV	Bulk Photovoltaic Effect
FPV	Flexo-photovoltaic Effect
PV	Photovoltaic
FE	Ferroelectric
DW	Domain wall(s)
V_{OC}	Open-circuit voltage
I_{SC}	Short-circuit current
I_{PV}	Local Photovoltaic Current
XRD	X-ray Diffraction
RSM	Reciprocal Space Mapping
SPM	Scanning Probe Microscopy
AFM	Atomic Force Microscopy
PFM	Piezoresponse Force Microscopy
PhAFM	Photoelectric Atomic Force Microscopy
PLD	Pulsed Laser Deposition
λ	wavelength
E_g	Bandgap
E_{Fn}	Quasi-Fermi Level
BFO	$BiFeO_3$
BFMO	$BiFe_{0.95}Mn_{0.05}O_3$
TSO	$TbScO_3$
STO	$SrTiO_3$
SRO	$SrRuO_3$

Chapter 1. Overview

Ferroelectrics are defined as materials possessing reversible spontaneous electric polarisation the magnitude and direction of which can be sensitively tuned by varying temperature, strain, electric field, pressure or chemical component[1]. An intriguing trait of ferroelectric materials, which has spurred continuous interests in academic community and industry in the last half century, is the coupling of ferroelectric polarisation, more generally, the non-centrosymmetric structures, to external stimuli and other physical properties[2]. For instance, the coupling between electric polarisation and mechanical strain in ferroelectric-ferroelastic materials leads to outstanding electromechanical response to external electric field/mechanical force with numerous applications in sensors and actuators[3]. Another widely pursued material class is the multiferroics, which exhibit coexistence and coupling of ferroelectric, ferroelastic and (anti-)ferromagnetic order parameters[4-6]. The coupling of different ferroic orders enables electrical control of magnetic moments and/or magnetic control of electric polarisation, leading to potential applications in electronic and spintronic applications.

Additionally, the interaction of ferroelectrics with light also results in fascinating phenomena, not only providing wider potential applications for ferroeletrics but also offering a playground to get fundamental insight into the physics of ferroelectricity[7,8]. The materials that are both photosensitive and ferroelectric define a field termed photoferroelectrics, which has been established for over 50 years but been largely overlooked[9]. One of the intriguing effects in the photoferroelectric field is the bulk photovoltaic effect generating an above bandgap open-circuit photovoltage under illumination[10]. Recent report of the anomalous photovoltage in domain-engineered bismuth ferrite ($BiFeO_3$) thin films has largely revived this field and offers an alternative path to boost the solar energy conversion efficiency[11]. An advantage of $BiFeO_3$ in terms of the application in the photovoltaic field is its moderate bandgap of ~2.7 eV, which lies in the visible light range and is considerably lower than the bandgap of other ferroelectric materials like $BaTiO_3$, $PbTiO_3$ and $LiNbO_3$. As proven by Bhatnagar *et al*., the anomalous photovoltage manifested in $BiFeO_3$ thin films originates from the bulk photovoltaic effect as in the case of other ferroelectrics, such as $BaTiO_3$, $LiNbO_3$ and $KNbO_3$[12].

Apart from the photovoltaic effect, the interaction of photo-induced effects upon the ferroelectric and multiferroic properties is also of large interest. It has been demonstrated

that light generated non-equilibrium carries in ferroelectrics decrease the Curie temperature and narrow the hysteresis width[7]. A recent progress in this aspect is the observation of a large photostriction effect in $BiFeO_3$ single crystals, which can be described in ferroelectrics as the combination of photovoltaic and piezoelectric effects[13]. The photovoltaic effect creates an internal electric field, which in turn leads to significant deformation by the inverse piezoelectric effect. Due to the innate coupling of multiple degree of freedoms in this material class, light may behave as an effective parameter to control physical properties of ferroelectric and multiferroic materials in addition to other external stimuli, such as electric field.

The main objective of this Thesis is to study and understand the electronic process of the bulk photovoltaic effect and the interaction of light with the electric polarisation by using $BiFeO_3$ as our research system. After recalling the basics of ferroelectric semiconductors, the mechanism of the bulk photovoltaic effect is introduced in Chapter 2. Also, the physical properties of $BiFeO_3$ are outlined in this chapter in terms of its ferroelectricity, domain walls and antiferromagnetism, etc. In Chapter 3, various techniques and tools will be introduced that have been employed in the present work. The technical protocol employed in the present Thesis, including fabrication of highest quality samples, performing structural and domain analysis with subsequent ferroelectric and electronic characterizations on both macroscopic and nanoscale levels, is to ensure the effects observed experimentally are generic and not stemming from some sample particularities.

In Chapter 4, the electronic origin of the bulk photovoltaic effect in $BiFeO_3$ is studied and elaborated with particular interest in the role of sub-bandgap levels. $BiFeO_3$ single crystals with different crystal orientations, domain patterns and growth runs are utilized to reveal the correlation between anomalous photovoltage and the activity of sub-bandgap levels. Moreover, Chapter 4 also demonstrate how the electronic origin can be used to tune the photovoltaic effect.

In Chapter 5, we work on the fundamental relation between the bulk photovoltaic effect and the ferroelectric polarisation in ferroelectric photovoltaic devices. To resolve this issue, we prepared monodomain $BiFeO_3$ thin films consisting of a single ferroelectric variant. The simple polarisation configuration in monodomain $BiFeO_3$ films explicitly excludes the possible contribution from domain walls and interfaces, providing an ideal system to study this topic. The temperature and light polarization dependent photovoltaic

effect of the monodomain ferroelectric device is studied to decipher the possible correlation.

In Chapter 6, we focus on the effective role of the domain walls in the conduction of the short-circuit current generated by the bulk photovoltaic effect in $BiFeO_3$ thin films. To this end, we developed a home-built photoelectric atomic force microscope to study the electronic and photovoltaic effect with a spatial resolution of tens of nanometres. Spatially-resolved photovoltaic current and photoconductivity are imaged by this microscopy to unravel the effect of domain walls on the photocurrent.

In Chapter 7, we turn our focus to the optical control of the ferroelectric order parameter at room temperature, which can be regarded as the ultimate interaction of light with ferroelectric materials. We demonstrate optically-induced reversible switching of ferroelectric polarisation in $BiFeO_3$ thin film by utilizing a combination of the bulk photovoltaic effect and a nanoscale electrode.

In Chapter 8, we propose and demonstrate a new photovoltaic effect termed the flexo-photovoltaic effect, which turns the bulk photovoltaic effect, which is originally constrained to the non-centrosymmetric crystals, into a universal effect allowed in all semiconductors by mediation of the flexoelectric effect. Thus, the devices based on this flexo-photovoltaic effect can be fabricated with silicon or any other semiconductor to enhance the solar energy conversion efficiency.

In Chapter 9, all the results will be summarized and an outlook will be presented.

Chapter 2. Theoretical Background

Basic background pertaining to the researches of the thesis is introduced here. The content is arranged as follows. The basic knowledge and research regarding the ferroelectric semiconductor are firstly reviewed. As the main subject of this thesis, the ferroelectric photovoltaic effect is then reviewed with special details focusing on the bulk photovoltaic effect. The flexoelectric effect is also briefly introduced. At last, a detailed description of the bismuth ferrite is given, the major material of interest of this work, in terms of its structure, ferroelectricity, domain walls, etc.

2.1 Ferroelectric Semiconductors

2.1.1 Introduction to Ferroelectrics

Ferroelectrics, established by Valasek in 1921, refer to materials that exhibit a spontaneous electric polarisation that can be reversed by applying an electric field[2,14]. This peculiar feature is characterized by a polarisation-electric field (*P*-*E*) hysteresis loop wherein switching happens at a critical field (E_C) termed coercive field, as depicted in Fig. 2-1. Most technologically important ferroelectrics, such as $BaTiO_3$ and (Pb, Zr)TiO_3, are perovskite oxides, of chemical composition ABO_3. They usually take cubic structure, also known as prototype phase, at high temperatures with a small B-site cation at the centre of an octahedral cage of oxygen ions and a large A-site cation at the unit cell corners (Fig. 2-2a). By decreasing temperature over the Curie temperature T_C, the centrosymmetric phase transforms to a non-centrosymmetric structure, giving rise to the electric dipole since the barycentre of the positive charges and the negative charges separate from each other (Fig. 2-2b, c).

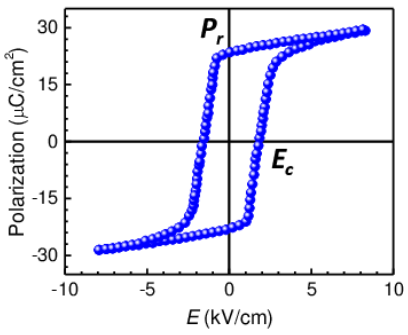

Figure 2-1. P-E hysteresis loop typical of a ferroelectrics with remnant polarisation P_r and coercive field E_c

By virtue of switchable spontaneous polarisation and non-centrosymmetric structure, ferroelectric materials have played an active role in nowadays electronic industry[15]. Being intrinsically piezoelectric, ferroelectric materials possess a substantial piezoelectric

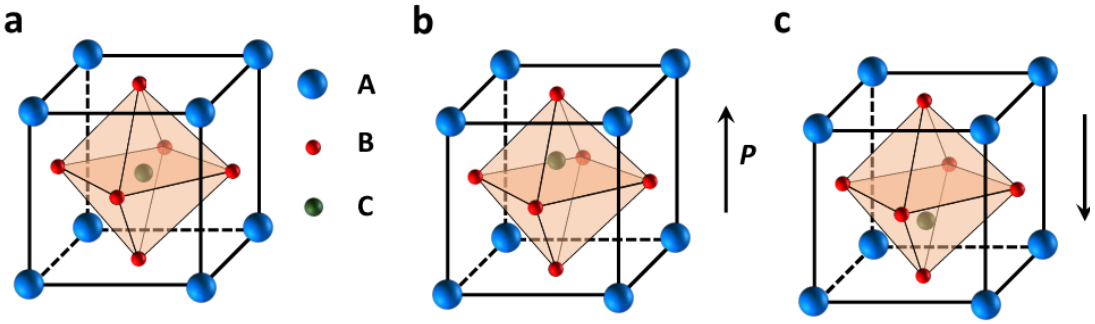

Figure 2-2. (a) Schematic of an ABO_3 perovskite structure above its Curie temperature with centrosymmetric symmetry. With decreasing temperature, ABO_3 transforms into noncentrosymmetric structures with electric polarisation pointing (b) upwards and (c) downwards.

constant, i.e. coupling between electric field and mechanical strain. This makes ferroelectrics widely used in microelectromechanical devices, such as ultrasonic sensors, actuators and acoustic filters[16]. As a subgroup of pyroelectricity, ferroelectric materials exhibits outstanding pyroelectric performance as compared to non-ferroelectric pyroelectrics, leading to extensive applications in infrared sensors[17]. Finally, the dielectric nature and the switchable polarisation of ferroelectrics have led to the recent spate of investigations of ferroelectric tunnel junctions and ferroelectric memristors, paving ways for the integration into high density data storages[18-20].

2.1.2 Ferroelectric Semiconductors

Although ferroelectricity has been traditionally considered as a property of the dielectric insulators, semiconductor physics of ferroelectrics, such as electron subsystems and carrier conduction, plays an important role in determining their ultimate properties and device performance[7]. This is first of all related to the coexistence in these materials of ferroelectricity and semiconducting nature. Being the first perovskite ferroelectrics, the discovery of ferroelectricity in $BaTiO_3$ possessing a moderate bandgap ($E_g \simeq 3.4eV$) started the investigation of the ferroelectric semiconductor properties. It is now well established that ferroelectricity not only exists in wide-bandgap materials, such as lithium niobate, but also in narrow-bandgap semiconductors, e.g. SbSI. The contribution of free energy of the electron subsystem to the lattice free energy and its interaction with the ferroelectric soft mode significantly affect the ferroelectric properties, especially at temperatures close to the phase transition[7]. For instance, the light-generated nonequilibrium carriers shift the Curie temperature of $BaTiO_3$ single crystal to a lower

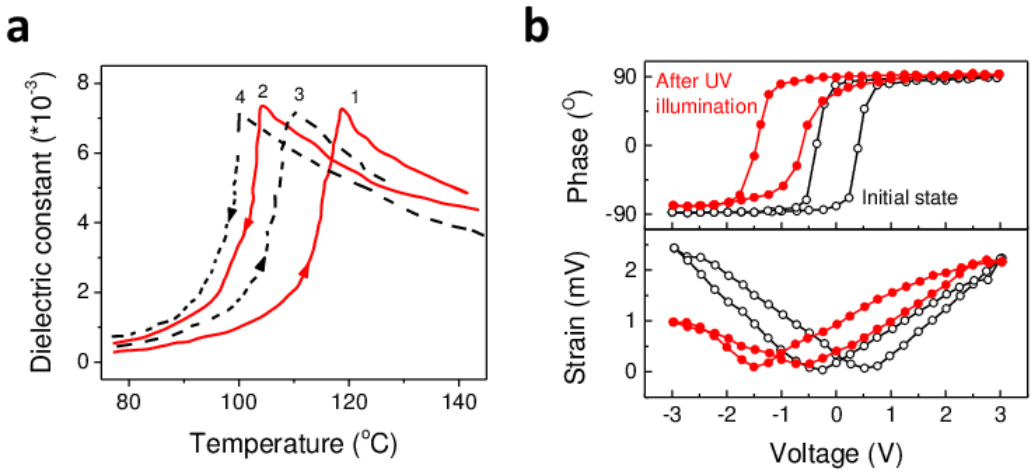

Figure 2-3. (a) Effect of illumination on the phase transition in $BaTiO_3$. (1, 2) Heating and cooling of the crystal in darkness; (3, 4) heating and cooling of the crystal with illumination[7]. (b) Phase and amplitude PFM loops of a negatively polarized grain before and after UV illumination[23].

value by ~5 ℃ and decrease the temperature hysteresis of the phase transition by about −3.3 ℃ (Fig. 2-3a)[7]. Meanwhile, trapping of nonequilibrium carriers also modifies the surface screening effect of the spontaneous polarisation, resulting in imprint and reduced remnant polarisation (Fig, 2-3b)[21-23].

The coexistence and coupling of ferroelectricity and semiconductor physics not only provide an intriguing approach to study the nature of ferroelectricity itself but also offers a fertile and rich playground to explore the new functionalities of ferroelectrics and to develop related technical applications. One of these phenomena is the ferroresistive switching wherein the electronic conduction properties of ferroelectric capacitors can be continuously tailored by controlling the ferroelectric polarisation switching process[19,24,25]. This allows non-destructive readout of the ferroelectric polarisation state and the associated multiple controllable resistive states offer a new path to develop the memristor for data storage (Fig. 2-4). Another important example is the ferroelectric domain walls, which possess intriguing functionalities different from that of the domain matrix, such as enhanced conductivity[26-28] and magnetism[29]. The domain wall conductivity along with their capability to be written/erased and moved by external electric or strain field without disruption of the host lattice has spawned world-wide interest in exploring novel domain wall-based concepts in memory and spintronic application (Fig. 2-5). Though remaining disputable, Rakita *et al.*[30] demonstrated the ferroelectricity in the tetragonal methylammonium lead triiodide ($MAPbI_3$), which is a metal–organic hybrid perovskite

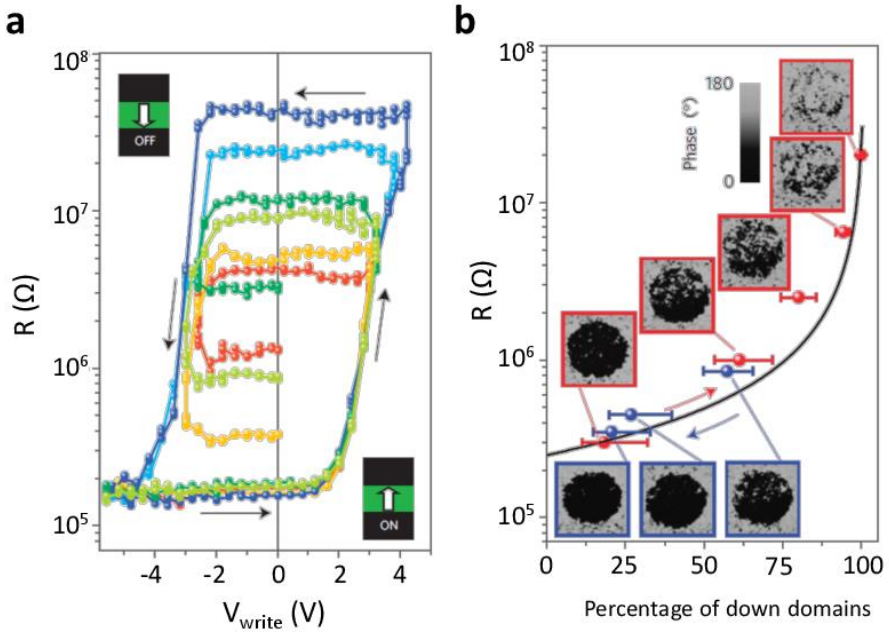

Figure 2-4. (a) Dependence of the Au/Co/$BaTiO_3$/$La_{0.67}Sr_{0.33}MnO_3$ capacitor resistance measured at 0.1 V after application of 20 ns voltage pulses (V_{write}) of different amplitude. (b) Variation of the capacitor resistance with the relative fraction of down domains[7].

known mainly for its remarkable electronic[31,32] and optical properties[33] as an outstanding light absorber in the next generation of solar cells. This opens the door for the realisation of multiple functionalities derived from ferroelectric behaviour and a wide range of devices that can be enabled by the juxtaposition of ferroelectricity and excellent semiconducting and electronic structure properties of the metal-organic hybrid perovskites[34]. Thus, it is important and rewarding to study the ferroelectric properties in the semiconductor realm to obtain deep understanding and to fully exploit their potential applications.

Last but not least, owing to their non-centrosymmetric structures, ferroelectric materials intrinsically exhibit photovoltaic effect under illumination, termed the bulk photovoltaic (BPV) effect originating from the asymmetric distribution of the light-generated nonequilibrium carriers in *k*-space. Combination of the BPV effect and semiconductor physics will further enrich this scientific community.

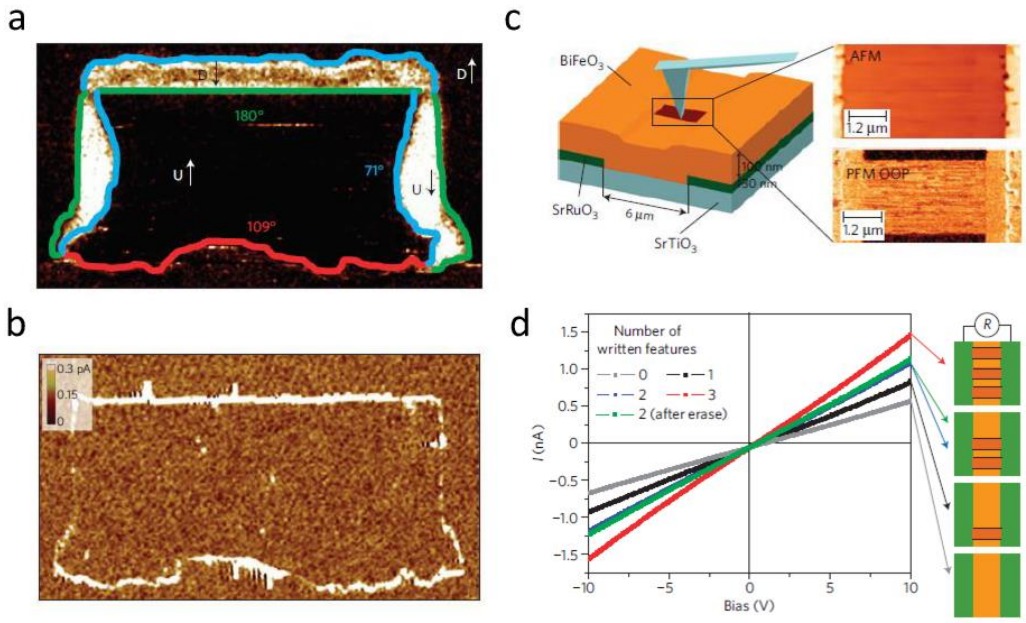

Figure 2-5. (a) In-plane PFM image of a written domain pattern in a monodomain $BiFeO_3$ (110) film and (b) Corresponding c-AFM image showing conduction at both 109° and 180° domain walls. (c) Schematic showing a ferroelectric in-plane device wherein 180° domain walls can be controllably written by PFM tip. (d) Current-voltage curves of the BFO device with increasing number of domain walls.[26]

2.2 Ferroelectric Photovoltaic Effect

During the last half century, ferroelectric materials have been extensively studied as a potential alternative to conventional semiconductor-based materials for photovoltaic applications, not only due to their multiple charge separation mechanisms but also the intriguing coupling and interactions between light and ferroelectric properties[7,8,35]. Research in this field started with the discovery of the photovoltaic current by Chynoweth in paraelectric $BaTiO_3$ crystal under illumination[52]. Later, in the 1974, the report by Glass of the ultrahigh photovoltage in $LiNbO_3$ under illumination established the field of the bulk photovoltaic (BPV) effect[36]. A recent report of the BPV effect in domain engineered BFO thin film has largely revived this field[37]. Before introducing the BPV effect, we briefly introduce the interface-based Schottky type PV effect in ferroelectric capacitors. At last, a brief introduction is given to the tip-enhanced PV effect in ferroelectrics, whereby a small electrode with reduced dimensions probes the PV current generated by the BPV effect.

2.2.1 Interface-based Photovoltaic Effect

As a wide bandgap semiconductor, a Schottky barrier forms at the interface between a ferroelectric material and most metallic electrodes[38,39]. The built-in field developed within the depletion region of the barrier can separate photo-excited carriers leading to a spontaneous PV current under illumination[40,41]. This Schottky type PV effect shares a similar characteristic of the conventional solar cells based on *p-n* junctions that the ultimate V_{OC} is restricted by the bandgap of the ferroelectric semiconductors. On the other hand, this PV effect exhibits an intriguing feature that the direction of its PV current can be reversibly switched by applying an external voltage due to the inherent correlation between the barrier profile and the ferroelectric polarisation charges, as depicted in Fig. 2-6[41,42].

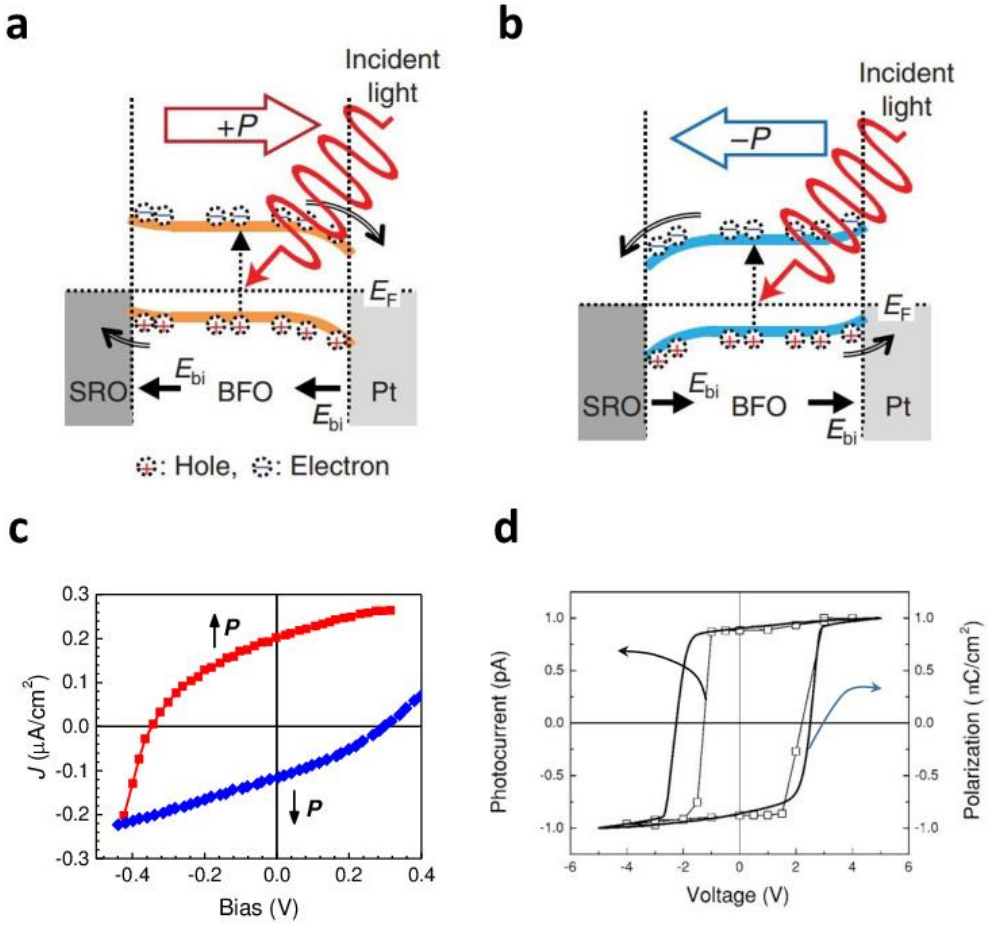

Figure 2-6. Schematic description of the photovoltaic effect for (a) the upward and (b) downward polarisation states in $Pt/BiFeO_3/SrRuO_3$ capacitor[42]. (c)Ferroelectric polarisation dependent current-voltage hysteresis loop of $Pt/BiFeO_3/SrRuO_3$ capacitor[42]. (d) Hysteresis type voltage dependent photovoltaic current and polarisation in $PbZr_{0.2}Ti_{0.8}O_3$ thin films[41].

2.2.2 Bulk Photovoltaic Effect

The BPV effect gives rise to a spontaneous current in the absence of any external voltage, in homogenous materials lacking inversion symmetry under uniform illumination[10]. The BPV effect has two characteristic features distinctive from other charge separation mechanisms. First, the magnitude and direction of the short-circuit photocurrent depend on the light polarisation direction with respect to the crystallographic geometry[10]. Second, the open-circuit photovoltage is not restricted to the bandgap of the illuminated materials, which can reach as large as several tens of thousands of volts[36]. The photocurrent originating in the BPV effect can be phenomenologically described by a third-rank tensor, which is given as[10]:

$$J_i = I_{light}\boldsymbol{\beta}_{ijk}\boldsymbol{e}_j\boldsymbol{e}_k \tag{2-1}$$

where J_i is the photocurrent density along a crystallographic direction, $\boldsymbol{\beta}_{ijk}$ is a third rank BPV tensor and I_{light} the light intensity, $\boldsymbol{e}_j$ and $\boldsymbol{e}_k$ the projection of the electrical field of the light. Accordingly, the photocurrent J_i exhibits an angular dependence on the light polarisation with a period of 180°. Note that only the linear bulk photovoltaic effect is considered in this thesis. For the information on the circular photovoltaic effect please refer to *Ref.* 10. The open-circuit voltage (V_{OC}), which compensates the photocurrent under illumination, corresponds to

$$V_{OC} = \frac{J_i d}{\sigma_d + \sigma_{ph}} \tag{2-2}$$

where d is the spacing between electrodes, σ_d and σ_{ph} are the dark and photo-conductivity. In most ferroelectric materials, photoconductivity is orders of magnitude larger than its dark conductivity. Thus, above equation can be simplified to

$$V_{OC} = \frac{J_i}{\sigma_{ph}} d \tag{2-3}$$

Clearly in above equation the value of V_{OC} can be easily increased by increasing the electrodes spacing distance or decreasing crystal conductivity via, for example, decreasing temperature, enabling V_{OC} to exceed the bandgap.

The BPV effect is associated with the excitation in a noncentrosymmetric crystal of the nonthermalized (hot) carriers, leading to asymmetric distribution of nonthermalized carrier momentum and a violation of the Boltzmann principle of detailed balance[10]. As

depicted in Fig. 2-7, the light-generated hot carriers lose the energy and descend to the band bottom with a shift distance of l_0. This shift distance l_0, also referred as thermalization length, results in the spontaneous movement of excited carriers towards a specific crystallographic direction, which can be expressed as:[43]

$$J_i = e\alpha I_{light}\left(\hbar\omega\right)^{-1}\phi\xi^{ex}l_0 \quad (2\text{-}4)$$

where *e* is the electron charge, α is the absorption coefficient, $\hbar\omega$ is the incident photon energy, ϕ is the quantum yield and ξ^{ex} is the parameter characterizing the excitation asymmetry. The value of the thermalization length is about tens of nanometres, e.g. $l_0 \approx 10-100$ nm for $BaTiO_3$ single crystals[44].

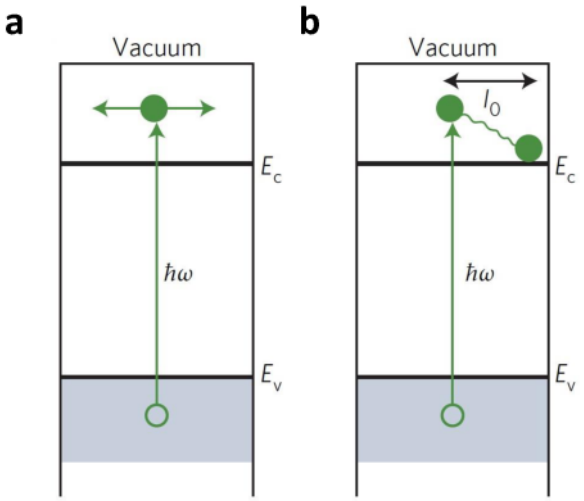

Figure 2-7. Schematic illustrating the photoexcitation processes in (a) centrosymmetric crystal and (b) non-centrosymmetric crystal[43].

In order to determine and evaluate the necessary conditions for the manifestation of the BPV effect, Ruppel et al. analysed the Boltzmann transport equation and discussed the role of asymmetry in *k*-space[45]. Under steady-state conditions, the distribution of electrons, i.e. the current $I(f)$, in terms of real space ***r***, momentum ***k*** and time *t* can be described by a distribution function $f(r,k,t)$, which satisfies the relation:

$$I(f) = \frac{\partial f}{\partial t} + \upsilon_k \nabla_r f - \frac{eE}{\hbar}\nabla_k f = G + R + S \quad (2\text{-}5)$$

where k is the wave vector of an electron, υ_k is the electron velocity which equals

$$\upsilon_k = \frac{\nabla_k \varepsilon_k}{\hbar} \quad (2\text{-}6)$$

where $\varepsilon_k = \varepsilon_{-k}$ is the electron energy. The electric field *E* in Eq. 2-5 is given as

$$E = -\nabla_r \phi(r,t) \quad (2\text{-}7)$$

where ϕ is the electric potential. In Eq. 2-5, $\upsilon_k \nabla_r f$ represents the diffusion currents due to spatial variation of carrier concentration, $\frac{eE}{\hbar}\nabla_k f$ represents the electric field driven current. The collision integral has been separated into three terms in the right side of Eq. 2-5, respectively G is the generation rate, R is the recombination rate and S is the scattering rate.

In the thermal equilibrium state, the distribution function *f* is given as the Fermi distribution:

$$f_{eq}(r,k) = f_{eq}(\varepsilon_k - E_F) = \frac{1}{1+\exp\left(\varepsilon_k - E_F \big/ kT\right)} \tag{2-8}$$

where E_F is the Fermi level energy. In thermal equilibrium, the distribution function is symmetric, i.e. $f_{eq}(k) = f_{eq}(-k)$ and there will be no electric current with equilibrium distribution described in Eq. 2-8. To generate a current, an asymmetric part $f^{as}(r,k)$ in the distribution function is required, which results in a current given as

$$J(r) = -\frac{2}{V}\sum_k e\upsilon_k f^{as}(r,k) \tag{2-9}$$

The asymmetric part $f^{as}(r,k)$ in the distribution function may results from the optical excitation which gives rise to a distribution function $f_{ph}(r,k)$ different from the $f_{eq}(r,k)$. This new distribution function $f_{ph}(r,k)$ consisting of a quasi-equilibrium distribution and a deviation is of the form:

$$f_{ph}(r,k) = f_{eq}\left[\varepsilon_k - E_F(r)\right] + \delta f(r,k) \tag{2-10}$$

The deviation part can be approximated as

$$\delta f(r,k) = \tau G(r,k) + \frac{\partial f_{eq}(\varepsilon_k - E_F)}{\partial(\varepsilon_k - E_F)}\upsilon_k \nabla_r E_F(r) \tag{2-11}$$

where τ is the relaxation time. In a homogeneous non-centrosymmetric crystal, the quasi-Fermi level is constant over the whole bulk. Thus the deviation part can only originate from the generation $G(r,k)$. In non-centrosymmetric materials, the generation rate $G(+k) \neq G(-k)$ in *k*-space, leading to an asymmetric deviation of the distribution function

$$\delta f^{as}(k) = \frac{\tau}{2}\left[G(+k) - G(-k)\right] = G^{as}\tau \tag{2-12}$$

under the condition that the recombination processes are different from the generation processes. From the above discussion it can be concluded that there are primarily two requirements for the existence of a BPV effect: first, the non-centrosymmetric structure and second, the recombination processes must proceed in ways that are different from the carrier excitation processes. The latter can be fulfilled by the mediation of the trapping levels in the sub-bandgaps which will be explicitly elucidated in Chapter 4.

2.2.3 Tip-enhanced Photovoltaic Effect

Reported by Alexe in 2010, the tip-enhanced photovoltaic effect was first discovered in the BFO single crystal where a nanoscale contact between the conductive AFM tip and the BFO surface collects similar amount of short-circuit photocurrent as that in the macroscopic coplanar electrodes. Owing to the reduced dimension at the AFM tip contact area, the tip-enhanced PV effect gives rise to a dramatically enhanced photocurrent density at the nanoscale contact, as illustrated in Fig.2-8[46].

A a of the tip-enhanced photovoltaic effect is that it enables to probe local photoelectric properties with nanometre resolution, such as local non-equilibrium carrier generation and recombination rate[47]. However, the tip-enhanced photovoltaic effect remains largely

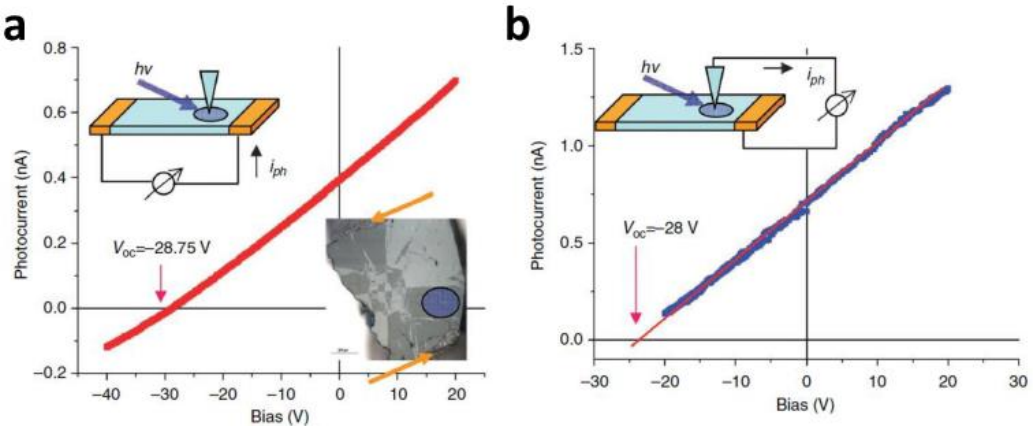

Figure 2-8. Photocurrent–voltage characteristics. (a) Measured macroscopically across the entire crystal by illumination in the region marked in the lower right inset, and (b) measured by probing with the AFM tip in the middle of the illuminated area. The upper left inset in (a) schematically shows the measurement setup and the connection to the macroscopic measurement; the lower right inset in (a) shows the crystal with silver electrodes marked by arrows and approximately the illuminated area by the laser spot. The inset in (b) shows the measurement[46].

a mystery in the field of photoferroelectrics. As this effect has so far only been manifested in BFO crystals, is it possible to observe it in BFO thin films? What is the origin of this tip-enhanced photovoltaic effect? Is it the BPV effect or the Schottky junction between the AFM tip and BFO surface? Could other ferroelectric materials exhibit this tip-enhanced PV effect as well? Is the quantum efficiency really enhanced by orders of magnitude? All these questions remains to be resolved and will be discussed in Chapters 6&7.

2.3 Flexoelectric Effect

Flexoelectricity is an electromechanical property defining a coupling between an electric polarisation and a strain gradient, which is allowed by the symmetry in all materials[48-50]. As illustrated in Fig. 2-9, a strain gradient breaks the structural centrosymmetry resulting in a strain-induced polarisation with a preferred direction whereas a homogeneous strain only deforms the shape without changing the inversion symmetry. The flexoelectric effect has been proven to significantly impact the physical properties of solid state materials, such as polarisation switching and local polarisation distribution[50,51], and shows potential applications in electromechanical transducers[52]. Although flexoelectricity has been largely studied in the field of electromechanical coupling, its core definition that strain gradient induces non-centrosymmetry indicates its potential applications in other fields, as illustrated in Fig. 2-10. For instance, keeping in perspective the definition of the flexoelectricity, one can perceive the possibility to

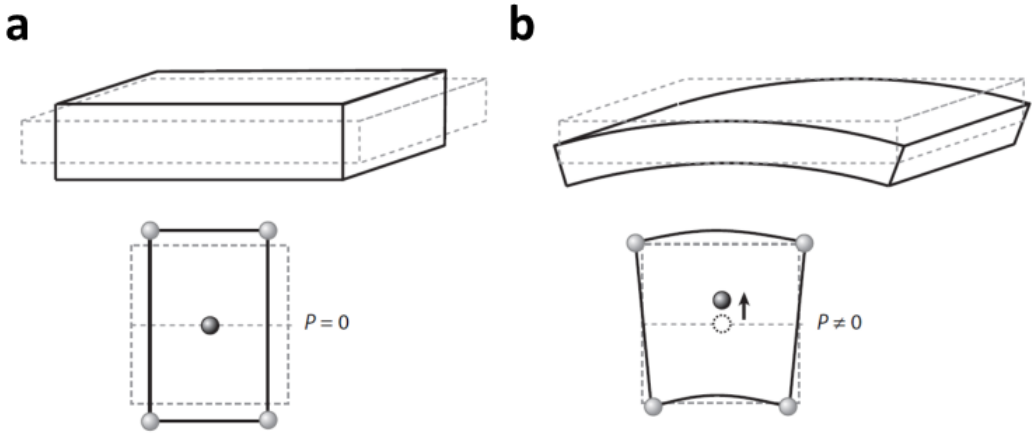

Figure 2-9. Schematic illustrating microscopic mechanism behind flexoelectric effect. (a) A homogeneous strain (e.g., induced by uniaxial compressive force) cannot modify the inversion symmetry. (b) An inhomogeneous strain induced, for example, by bending, breaks the centrosymmetry inducing an electrical polarisation[48].

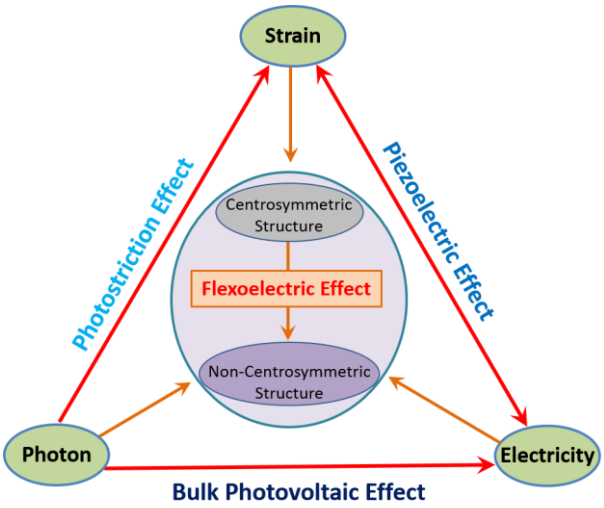

Figure 2-10. Schematic diagram showing the flexoelectricity mediated correlation between electricity, strain and photon. The strain gradient breaks local centrosymmetric structure into non-centrosymmetry, enabling a universal electromechanical coupling between electricity and strain (converse- and flexoelectric effect), conversion from photon energy into electricity (flexo-photovoltaic effect), and mechanical response to the light (flexo-photostriction effect).

develop a local non-centrosymmetric structure in centrosymmetric semiconductors via a strain gradient, which allows the manifestation of the BPV effect. Due to the universal nature of the flexoelectricity, this flexoelectricity-induced BPV effect (termed Flexo-photovoltaic effect in this thesis) is supposed to be allowed by all symmetries where the photo-excited carriers are separated by the local noncentrosymmetry instead of a built-in field. This flexo-photovoltaic effect will be discussed and demonstrated in Chapter 8.

2.4 Bismuth Ferrite

Bismuth ferrite ($BiFeO_3$, BFO), the only single-phase multiferroic material exhibiting unambiguous magnetoelectric coupling at room temperature, has received tremendous attention in the last 15 years as it provides a fertile platform to discovery of new fundamental physics and design exciting potential applications in data storage, spintronics and high frequency devices[15,53]. It exhibits large ferroelectric polarisation with a Curie temperature of ~1103 K as well as G-type antiferromagnetism with the Neel temperature of ~673 K. Additionally, its moderate bandgap ($E_g \simeq 2.7$ eV) endows an opportunity to study the interplay of ferroelectricity and semiconductor physics, such as the photovoltaic effect and its associated effect on ferroelectricity. Thus, we exploited

BFO as the research systems in both single crystal and thin film form to study the photo-induced effects in ferroelectric materials.

2.4.1 Structure and Ferroelectricity

Bulk BFO is rhombohedral belonging to the point group of *R3c*[54]. Its perovskite-type unite cell has a lattice parameter of 3.965 Å and a rhombohedral angle of ca. 89.3-89.4° with the ferroelectric polarisation along $[111]_{pc}$ at room temperature (pc denotes the pseudocubic index)[55]. The BFO unit cell can also be described in the terms of a hexagonal lattice with the hexagonal *c*-axis parallel to the diagonals of the perovskite cube, as depicted in Fig. 2-11. Each BFO hexagonal unit cell consists of two distorted perovskite unit cells connected along their body diagonals. As the tolerance factor of the BFO structure is smaller than one, which is defined as $t = (r_{Bi} + r_O)/\sqrt{2}(r_{Fe} + r_O) \sim 0.88$, the oxygen octahedra buckle to fit into the small cell[56]. As a result, the two oxygen octahedra in the hexagonal cell rotate in opposite directions by $\pm 13.8°$ around the $[111]_{pc}$ axis with the Fe ions shifted by 0.135 Å away from the oxygen octahedra[54,57,58], and the Fe-O-Fe angle, which is crucial to the magnetism and electronic properties, buckles to a value of ca. 154-156° [54].

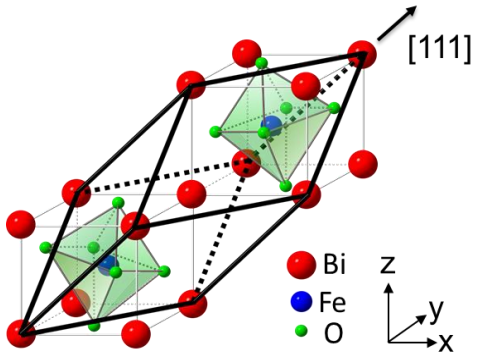

Figure 2-11. Schematic illustrating the crystal structure of perovskite $BiFeO_3$[58].

By diminish the leaky current problem, BFO single crystals[59], ceramics[60] and thin film[61] all exhibit the largest switchable ferroelectric polarisation in comparison with other perovskite oxides, i.e. ca. 60 μC/cm^2 along $[001]_{pc}$ direction and 100 μC/cm^2 along $[111]_{pc}$ direction. The BFO ferroelectricity mainly originates from the hybridization between stereochemical activity of the large Bi^{3+} 6s lone-pair electrons and O^{2-} p electrons[62-64]. In conjugation with its high Curie temperature (T_C~1100 K), the ferroelectric polarisation magnitude in BFO is almost temperature independent over a large temperature range (10-800 K)[65].

2.4.2 Domains and Domain Walls

In a real ferroelectric material, the ferroelectric polarisation *P* varies at locations where defects exist, especially at the sample surface where *P* decreases abruptly to zero, giving rise to a depolarisation field and substantial electrostatic energy. To minimize this unfavourable energy, different regions in a ferroelectric material generally polarize in different directions. Each volume of uniform polarisation is referred to as a domain and the boundaries separating domains are referred to as domain walls. Owing to the varied lattice symmetry and associated local elastic strain, there is a certain amount of energy associated with domain walls. Then, the final domain configuration is determined by minimizing the total free energy[2]. Normally, as described by the Kittel law, domain size scales with the square root of the sample thickness[66].

In terms of bismuth ferrite, its rhombohedral structure described by *R3c* space group allows its polarisation to point along the eight diagonal directions, i.e. $<111>_{pc}$, as illustrated in Fig. 2-12a. Because P_i^+ and P_i^- (i=1, 2, 3, 4) share the same structural distortion, there are four variants of the ferroelastic orders in BFO (Fig. 2-12b). Correspondingly, there are three types of domain walls in BFO defined by the angle between the polarisations of adjacent domains, respectively 71°, 109° and 180°. As shown in Fig. 2-13, the 71° domain walls exists in the (101) planes at 45° with respect to the $(001)_{pc}$-oriented surface whereas the 109° domain walls stay in the (100) planes running perpendicular to the $(001)_{pc}$ surface. Owing to its importance in exploring emergent physics from domain boundaries and designing ferroelectric-based devices, control of ferroelectric domain structures during thin film deposition has received much

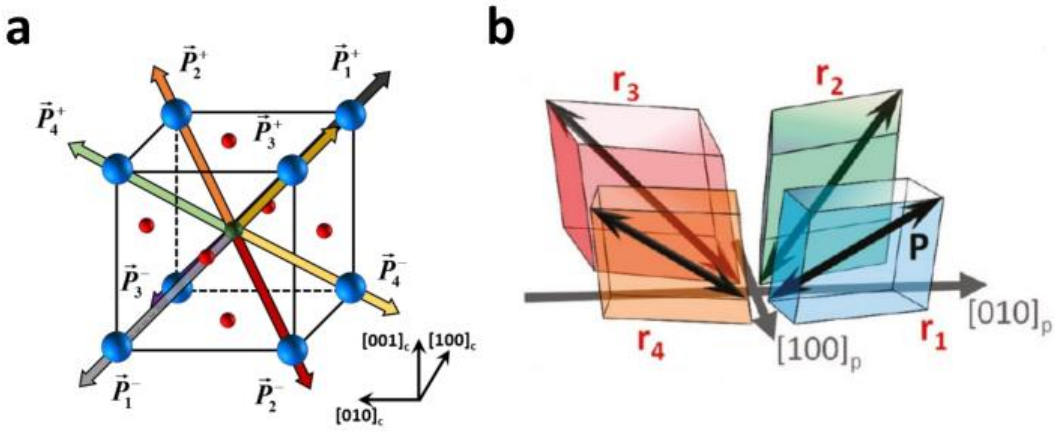

Figure 2-12. (a) Ferroelectric and (b) ferroelastic variants in $BiFeO_3$[74].

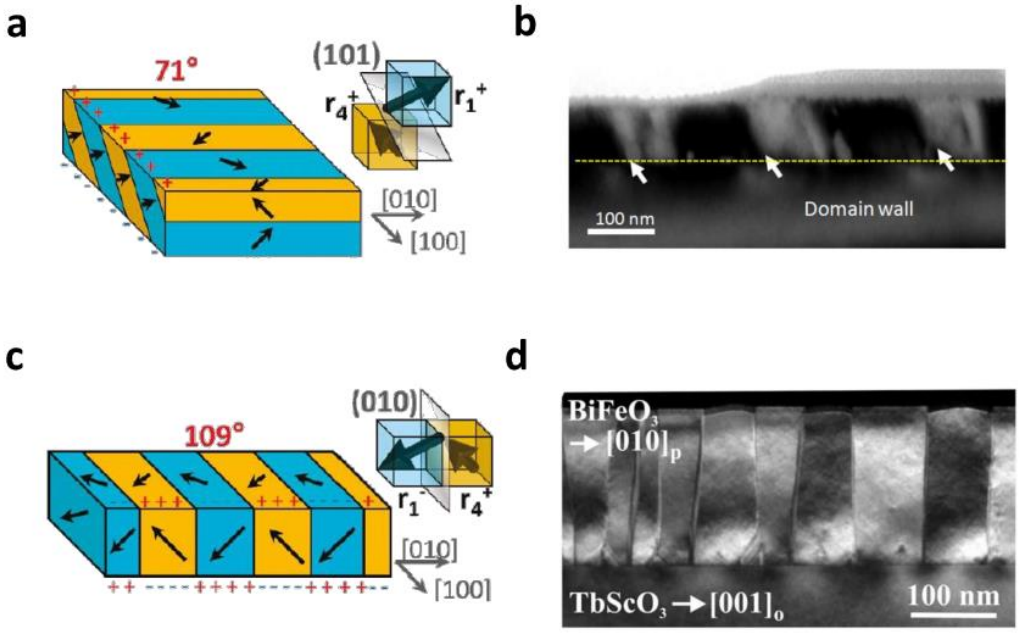

Figure 2-13. (a) Schematic showing the arrangement of 71° domain walls and (b) the TEM image of a $BiFeO_3$ sample with 71° domain walls. (c) Schematic showing 109° domain walls and (d) the TEM image showing 109° domain walls[73]. (a) and (c) are taken from *Ref.* 74. (d) is from A. Bhatnagar's thesis[75].

attention within the last one decade. Nowadays, it is possible to selectively control the as-grown domain structure and domain wall type by tuning the boundary conditions, such as substrate symmetry, miscut and substrate surface termination[67-71]. For instance, Solmaz et al. reported controlled ordering of domains in BFO thin films as well as controlled selection between 71° and 109° domain walls by modifying the substrate termination[70]. Chen et al. report the ordered arrangement of 180° domain walls in (110)-oriented BFO thin films (thickness < 32 nm) grown in insulating $GdScO_3$ $(010)_O$ substrate[72].

2.4.3 Anti-ferromagnetism

In addition to its outstanding ferroelectric properties, bismuth ferrite also exhibits G-type antiferromagnetism with a Neel temperature of 643 K, wherein neighboring Fe spins couple ferromagnetically within pseudocubic (111) planes and antiferromagnetically between neighboring (111) planes[76]. In fact, the neighbouring Fe spins are not perfectly antiparallel due to the magnetoelectric interaction with ferroelectric polarisation, giving rise to a net magnetization and a weak ferromagnetic moment of the Dzyaloshinskii-Moriya type[77]. This weak magnetization is further cancelled by a long-range superstructure (λ=64 nm) consisting of an incommensurate spin cycloid of the

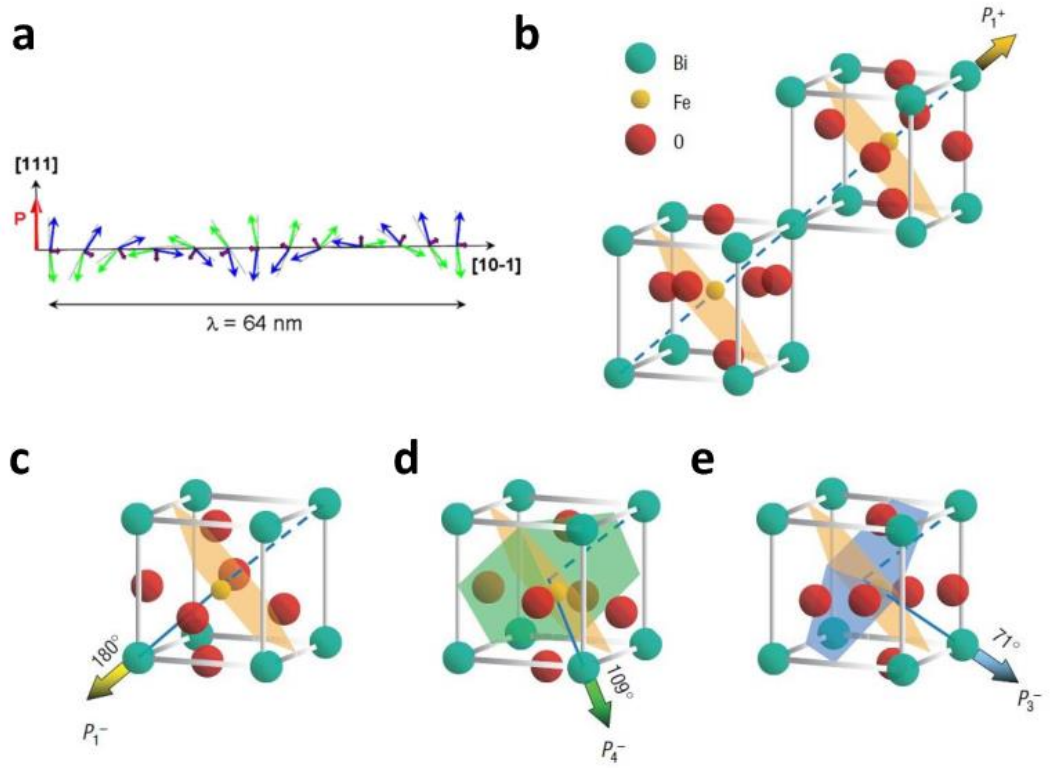

Figure 2-14. (a) Schematic representation of the spin cycloid. The canted antiferromagnetic spins (blue and green arrows) give rise to a net magnetic moment (purple arrows) that is specially averaged out to zero due to the cycloidal rotation[58,60]. (b-e) Schematics showing the coupling between ferroelectric polarisation and magnetic easy plane in $BiFeO_3$[47]. Ferroelectric polarisation is switched by (c) 180°, (d) 109° and (e) 71°. It shows that only ferroelastic switching, i.e. 109° and 71° switching is able to rotate the magnetic easy plane in bismuth ferrite.

antiferromagnetically ordered sublattices (see Fig. 2-14a)[78]. The spin cycloid can be suppressed, resulting in a net non-zero moment, by the application of a large magnetic field or by epitaxial strain in thin films[79,80]. The antiferromagnetism in BFO is intrinsically coupled to the ferroelectric polarisation through ferroelastic distortion. Specifically, the magnetic moments rotate within the plane defined by the ferroelectric polarisation ($[111]_{pc}$ direction) and the cycloid propagation direction ($[10\text{-}1]_{pc}$ direction), as depicted in Fig. 2-14a. As a result, once the polarisation is switched by an electric field by 71° or 109°, the magnetic easy plane switches as well (see Fig. 2-14b-e)[65]. As a result, BFO could serve as an elegant platform to fulfil electric control of multiple degrees of freedom, as well as promising multiple functionalities.

Chapter 3. Experimental and Characterization Methods

In this chapter, the experimental techniques used in the study of ferroelectric photoelectric effects are presented, starting from the fabrication processes to the determination of crystallographic structures and nanoscale characterization of electronic properties. Scanning probe-based local characterization techniques are highlighted to illustrate their working principles and applications, as they are widely used in the research presented in this thesis.

3.1 Thin Film Deposition

In the present work, the BFO and $SrRuO_3$ (SRO) thin films were epitaxially grown on insulating crystalline substrates with defined orientations by pulsed laser deposition. For the electrical measurements, metallic electrodes with designed geometries were patterned on top of the BFO surface by e-beam evaporation.

Pulsed laser deposition (also known as PLD) is a physical vapour deposition process where materials are ablated from targets by laser pulses and then deposited on a substrate. During the deposition process, a pulsed laser with sufficiently high energy density is focused onto a target of the materials to be deposited, which ablates a small amount of materials creating a plasma plume. This ablation plume provides the material flux for film growth and moves towards the heated substrates. Then, materials are crystallized at the substrates, as schematically shown in Fig. 3-1.[81] Owing to its attractive features including

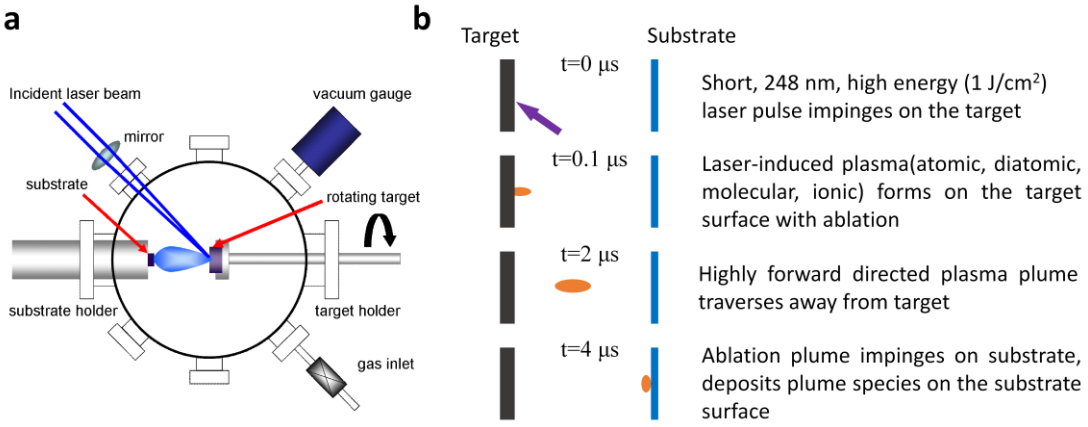

Figure 3-1. Schematics of PLD process. (a) Schematic setup of a PLD system. (b) The ablation process. [81]

stoichiometric transfer, excited oxidizing species and simplicity, PLD has now emerged as one of the most competitive technique in the complex oxide thin-film research area. The growth parameters for BFO and SRO are summarized in Table 3-1. Both BFO and SRO targets are chemically stoichiometric.

Table 3-1. Growth parameters of $BiFeO_3$ and $SrRuO_3$ in NELE PLD chamber

	$BiFeO_3$	$SrRuO_3$
Temperature (°C)	620	670
Oxygen Pressure (mbar)	0.15	0.15
Laser Fluence (J/cm^2)	1	1
Frequency (Hz)	10	5
Target-to-Substrate Distance (cm)	5	4

3.2 Structure Characterization

The crystallographic structures of the BFO films grown by PLD are characterized by both X-ray diffraction (XRD) 2θ-ω scans and reciprocal space mapping (RSM) methods. The former method is able to show the possible parasitic phase, such as Bi_2O_3 and Fe_2O_3 while the RSM is able to show the structural variants of the epitaxial BFO film, which are intrinsically correlated with ferroelastic and ferroelectric order parameters.

3.2.1 XRD 2θ-ω scan

The x-ray diffraction (XRD) is one of the standard techniques for characterizing material structures, such as crystallinity, phase, orientation and defects, via the interaction between incident X-ray photons and regularly arranged atoms. As schematically shown in Fig. 3-2a, this interaction can be described by Bragg's Law, which is given as:

$$2d_{hkl}\sin\theta_{hkl} = n\lambda \tag{3-1}$$

where d_{hkl} is distance between (hkl) planes, θ_{hkl} is the diffraction angle, n is an diffraction order and λ is the wavelength of the X-rays (1.5406 A).

In this work, the XRD measurements on the BFO thin films were performed by a Philips Analytical diffractometer in which the position of the samples can be aligned in 3D dimensions, as schematically shown in Fig. 3-2b. To do the $2\theta-\omega$ scan on a specific plane, such as (002), firstly, the sample is oriented, by mainly tuning ω and Φ, to align

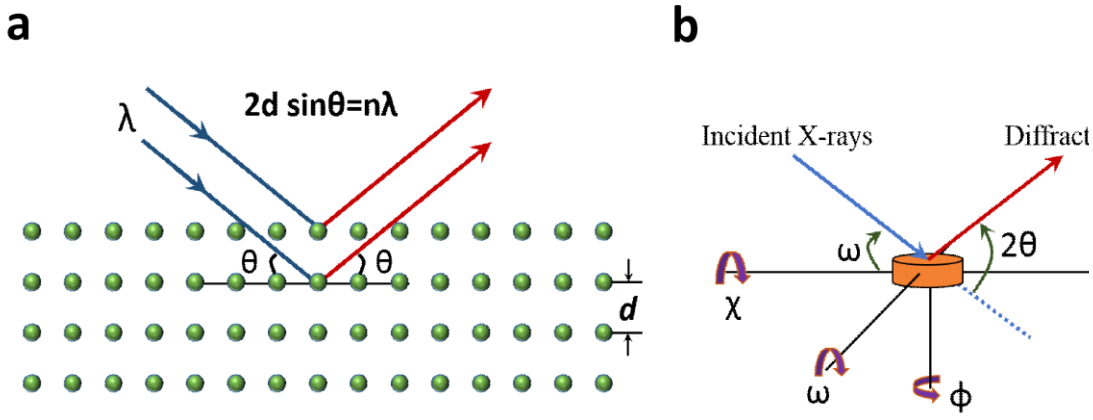

Figure 3-2. Schematics of XRD measurement. (a) Schematic of the Bragg's diffraction law. (b) The angles associated with the diffractometer movement.

the measured plane perpendicular to the plane made by the incident and diffracted X-ray. Then the offset Δω between 2θ and 2ω has to be calibrated before performing the scan. While doing the scanning, the value of 2θ and ω changes by 2Δθ and Δθ each step, respectively, to retain the offset constant. The peak positions in the $2\theta - \omega$ scan give the information on the spacing between the diffracting faces according to Eq. (3-1).

3.2.2 Reciprocal Space Mapping

Apart from the $2\theta - \omega$ scan, we also performed reciprocal space mapping (RSM) around some diffraction peaks of the BFO films, such as (002) face and {113} faces, to further characterize the crystallographic structures in terms of strain relaxation, structural variants and lattice parameters, etc.

The reciprocal lattice for the crystal of interest is a Fourier transformation of its real lattice, which is represented by dots, as schematically shown in Fig. 3-3. The position of a reciprocal lattice point represents a real lattice plane, defined by the distance from the origin that is $1/d_{hkl}$, and the direction with respect to the origin that is the real lattice plane normal. Experimentally, the RSM is performed by combining 2θ scan and ω-steps covering a range of divergence. At each incident angle ω, 2θ scan is carried out spanning a range of Δ2θ. The area of the reciprocal space mapped by Δω-Δ2θ combination is represented by the red shadow in Fig. 3-3. The correlation of the reciprocal space coordinates $\mathbf{s}_x$ and $\mathbf{s}_z$ to the incident angle ω and diffraction angle 2θ is given as[82]:

$$s_x = \frac{1}{\lambda}\{\cos\omega - \cos(2\theta - \omega)\} \tag{3-2}$$

$$s_z = \frac{1}{\lambda}\{\sin\omega + \sin(2\theta - \omega)\} \quad (3\text{-}3)$$

The number and shape of the diffraction peaks contains information on the atom arrangement in the structure as well as distribution and volume of the regions possessing this interplanar spacing. In terms of BFO, it is possible to have four structural variants due to the rhombohedral distortion of its perovskite structure. The type and relative volume of these structural variants can be determined by the RSM technique.

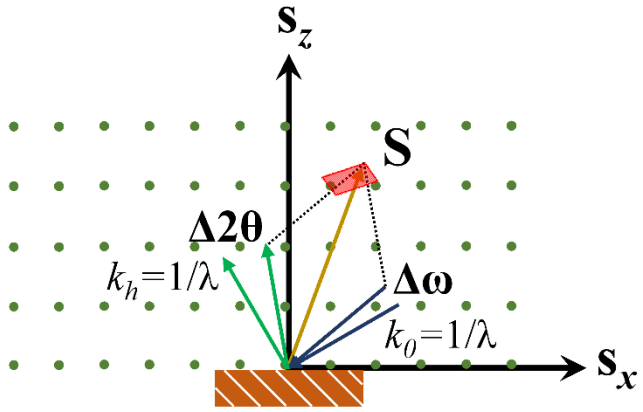

Figure 3-3. The mapped region of reciprocal space covered by a range of incident angle and diffraction angle.

3.3 Scanning probe microscope based local characterization

Scanning probe microscope (SPM) based tools have been widely used in the research works presented in this thesis to characterize and modulate local topography, ferroelectric, electric and photoelectric properties. The main operating principle of a SPM is based on the interaction between a nanoscale sharp tip, which is mounted at the end of a soft silicon (or silicon nitride) cantilever, and the material surface to be analyzed. As the tip scans along a sample surface, the variation of surface topography gives rise to a cantilever deflection, revealing information about the surface morphology. For a ferroelectric material stimulated by an external AC voltage, the converse piezoelectric effect induced local surface oscillation forces the contacted tip along with the cantilever to vibrate with the same frequency. The phase and amplitude of the cantilever vibration contain information about the local ferroelectric/piezoelectric properties. Additionally, the conducting SPM tip can also act as a nanoscale electrode, enabling to probe local electric properties. Once assisted with a light source illuminating upon the sample surface of interest, local photoelectric properties, such as photoconductivity and photovoltaic effect, can be unraveled as well.

3.3.1 Atomic Force Microscope

The atomic force microscope, also known as AFM, has been used in a wide range of research fields, such as solid state physics, semiconductor science and technology and bio-materials, to investigate local morphology and related physical properties. As schematically shown in Fig. 3-4a, the AFM system consists of a cantilever with a sharp tip at its end that is used to scan the specimen surface. When the tip is approached close to the sample surface, a force induced by the interaction between the tip and sample surface leads to the deflection of the cantilever according to, in a first approximation, Hooke's law. The cantilever deflection, respectively the magnitude of the force exerted on the tip, is monitored by an optical system consisting of a laser or a LED and a Position Sensitive Photo Detector (PSPD). The signal detected by the PSPD is compared with a preset value, and the difference is termed the error signal. The error signal is then fed into a proportional-integral-differential (PID) feedback controller that regulates the vertical position of the cantilever to minimize the error signal. By processing spatially-distributed PID output signal while scanning the tip on the surface, a three-dimensional map of the surface topography is obtained.

Based on the type of interaction between the tip and studied surface, i.e. attraction or repulsion, the AFM technique can be categorized into three modes: contact mode, non-contact mode and tapping mode. As depicted in Fig. 3-4b, when the tip approaches to the sample surface, it first senses a long-range attractive force. This region of the force curve is used for the non-contact mode. This attractive force is usually the van der Waals force but other types of forces may contribute to some extents depending on the surface and tip

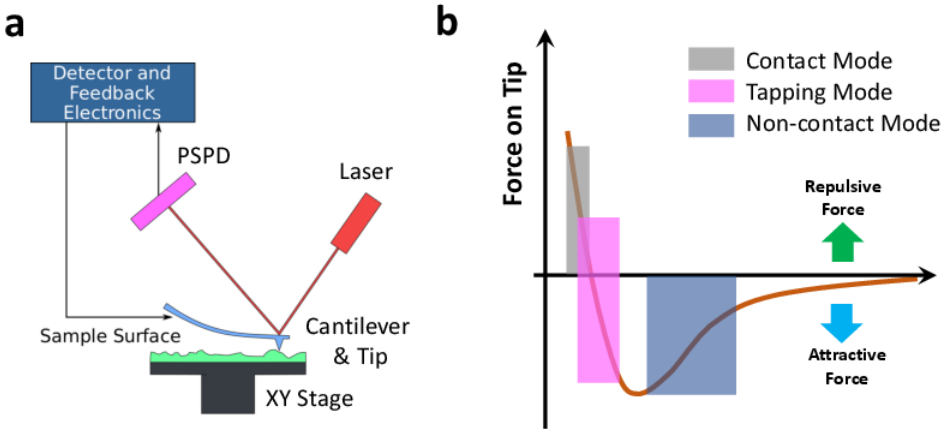

Figure 3-4. (a) Schematic of AFM setup. (b) The force vs tip-sample distance.

properties. Further approaching the tip to the surface, the interaction gives rise to a repulsive force. It is in this range that the contact mode works. For the tapping mode, the cantilever is driven to oscillate up and down at or near its resonance frequency, experiencing an attractive force when tip moves away from the surface but repulsive force once it oscillates towards the surface. In this thesis, we use the contact mode to characterize sample surface morphology along with other physical properties.

3.3.2 Piezoresponse Force Microscope

The piezoresponse force microscope, in short PFM, is a variant of the AFM that allows to characterize and modulate the ferroelectric/piezoelectric domains. This is achieved by bringing a conductive AFM tip into contact with the surface of a ferroelectric material of interest and applying an external AC bias to the tip or sample to trigger local mechanical vibrations in the ferroelectric materials due to the converse piezoelectric effect. The ferroelectric surface oscillation is then detected by the cantilever with the help of the PSPD system and demodulated by a lock-in amplifier, as schematically shown in Fig. 3-5. In this way, both surface morphology and ferroelectric domain structures of the same area can be mapped simultaneously with nanometer resolution.

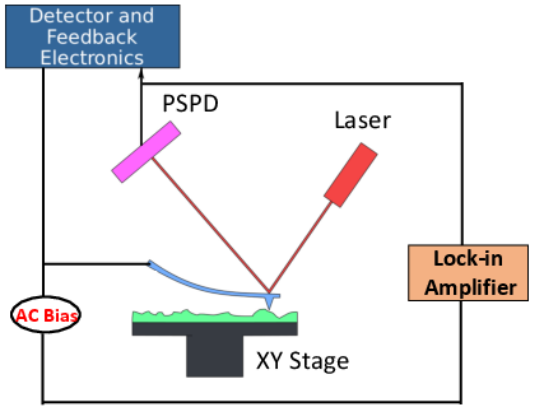

Figure 3-5. Schematic of PFM setup

As mentioned above, the mechanism behind the PFM is the converse piezoelectric effect, which describes a linear coupling between the applied electric bias E_k and the induced mechanical strain ε_i. This correlation can be described as:

$$\varepsilon_i = d_{ki} E_k \tag{3-4}$$

where d_{ki} is the piezoelectric tensor. In the case of the BFO possessing *R3c* symmetry, above equation can be elaborated in the rhombohedral coordinate as[83]:

$$\begin{pmatrix}\varepsilon_1\\ \varepsilon_2\\ \varepsilon_3\\ \varepsilon_4\\ \varepsilon_5\\ \varepsilon_6\end{pmatrix}=\begin{pmatrix}0 & -d_{22} & d_{31}\\ 0 & d_{22} & d_{31}\\ 0 & 0 & d_{33}\\ 0 & d_{15} & 0\\ d_{15} & 0 & 0\\ -d_{22} & 0 & 0\end{pmatrix}\begin{pmatrix}E_1\\ E_2\\ E_3\end{pmatrix} \tag{3-5}$$

The resultant strain components are

$$\begin{pmatrix}\varepsilon_1\\ \varepsilon_2\\ \varepsilon_3\end{pmatrix}=\begin{pmatrix}-d_{22}E_2+d_{31}E_3\\ d_{22}E_2+d_{31}E_3\\ d_{33}E_3\end{pmatrix} \tag{3-6}$$

As illustrated by Fig. 3-6, the strain component ε_1 and ε_2 give rise to a local shear deformation of the ferroelectric surface, which in turn exerts a torsional force on the AFM tip. The resultant lateral deflection of the cantilever, defined in the PSPD as $[(B+D)-(A+C)]/(A+B+C+D)$ and demodulated by the lock-in amplifier, reveals information about the in-plane ferroelectric domains. On the contrary, the component ε_3 induces a vertical surface deformation and modulates the cantilever deflection signal $[(A+B)-(C+D)]/(A+B+C+D)$, which unravels the out-of-plane ferroelectric domain properties.

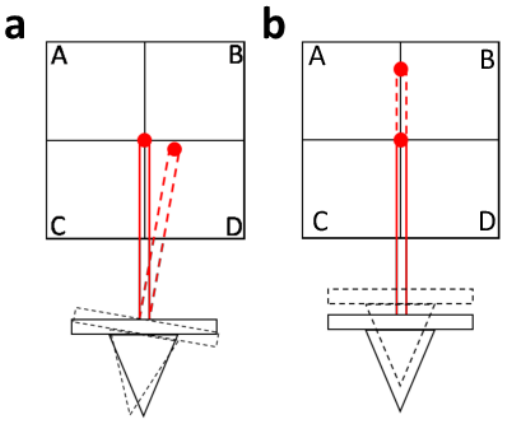

Figure 3-6 (a) In-plane torsional strain and (b) vertical strain induced cantilever deflection with related signal on PSPD. Original figure is from Wikipedia.

The orientation of the local ferroelectric polarisation is characterized by the phase signal between the local surface deformation and AC voltage applied to the tip. As depicted in Fig. 3-7, ferroelectric domains with opposite polarisation directions give rise to 180° phase shift of the piezoresponse with respect to the AC driving voltage. This phase variation can be ready extracted by the lock-in amplifier along with the local piezoresponse amplitude.

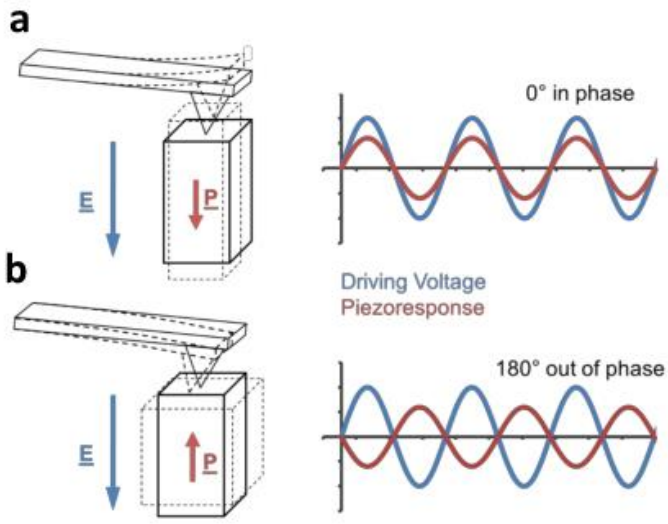

Figure 3-7. Piezoresponse with electrical field (a) parallel and (b) antiparallel to ferroelectric polarisation. Original figure was token from Wikipedia.

The BFO thin film is of rhombohedral structure with ferroelectric variants pointing to eight ⟨111⟩ directions, giving rise to polarisation components in both in-plane and out-of-plane directions. In order to characterize the BFO domain structures all-round, angle-resolved PFM method is imperative as schematically shown in Fig. 3-8. By placing the cantilever along two orthogonal directions, four in-plane ferroelectric components can be readily revealed by in-plane PFM phase signal. Along with the out-of-plane phase signal, the distribution of eight ferroelectric variants can be distinguished.

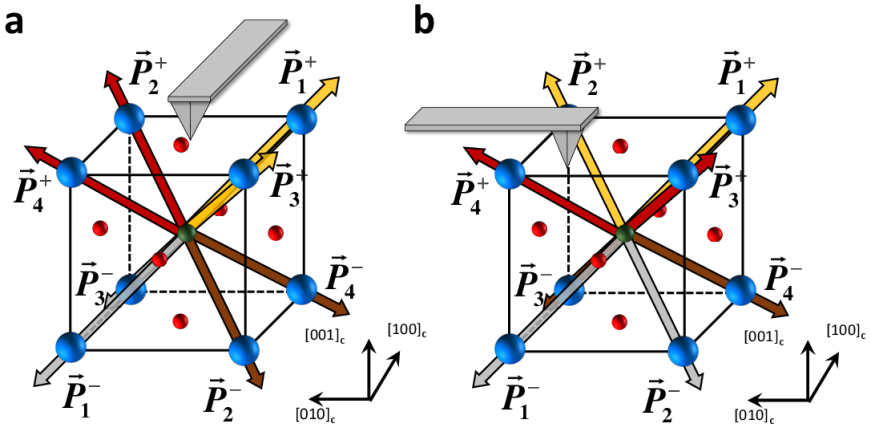

Figure 3-8. Schematics for angle-resolved PFM measurement on $BiFeO_3$ thin films. The cantilever is oriented along (a) $BiFeO_3$ $[100]_{pc}$ direction and (b) $[010]_{pc}$ direction.

3.3.3 Photoelectric Atomic Force Microscope

The photoelectric atomic force microscope, also termed PhAFM, is a home-built SPM system to characterize local photoelectric properties, e.g. photoconductivity and photovoltaic effects, of BFO crystals and thin films. As depicted in Fig. 3-9, PhAFM consists of an AFM-based system (XE-100, Park) modified by a current amplifying circuit and an optical system. The latter allows illumination of the sample surface with tunable light polarisations by employing a half-wave plate. The current probed by the conductive AFM tip, either originated from the photovoltaic effect or driven by an external voltage, was first read by a transimpedance amplifier (Femto, DLPCA-200) with a gain of 10^8 V/A. The voltage signal was further amplified 10 times and filtered by a low pass filter with a cut-off frequency of 300 Hz and 12dB. Afterwards, the final voltage signal was fed back to the AFM system and recorded simultaneously with the topography signal. To complete the current circuit with the PhAFM system, another grounded electrode is also prepared, which is either the conductive film underneath the BFO film or a stripe platinum electrode on top of the BFO surface.

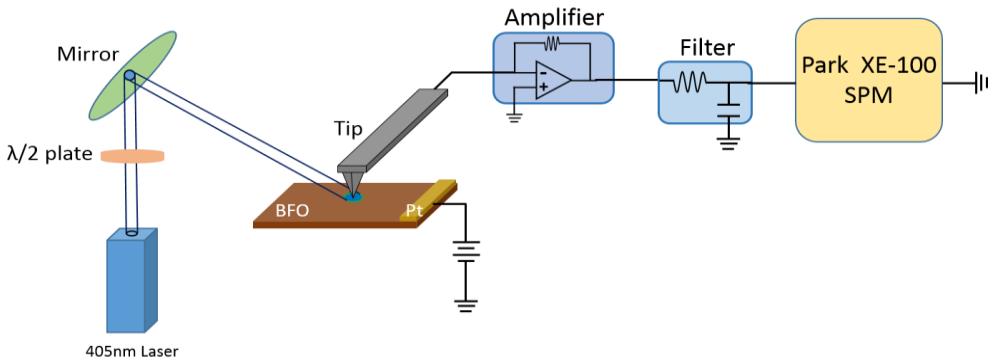

Figure 3-9. Schematic of the PhAFM system.

3.4 Photoelectric Property Characterization

The photoelectric properties of materials of interests, i.e., photoconductivity and photovoltaic effects, are characterized on both macroscopic and nanoscale levels. On the macroscopic level, a pair of stripe electrodes are evaporated on the surface of the BFO crystals and thin films, running parallel to a specified BFO crystallographic direction (see Fig. 3-10). Two main types of characterization are performed on the BFO samples, respectively temperature-resolved and wavelength-resolved photoelectric

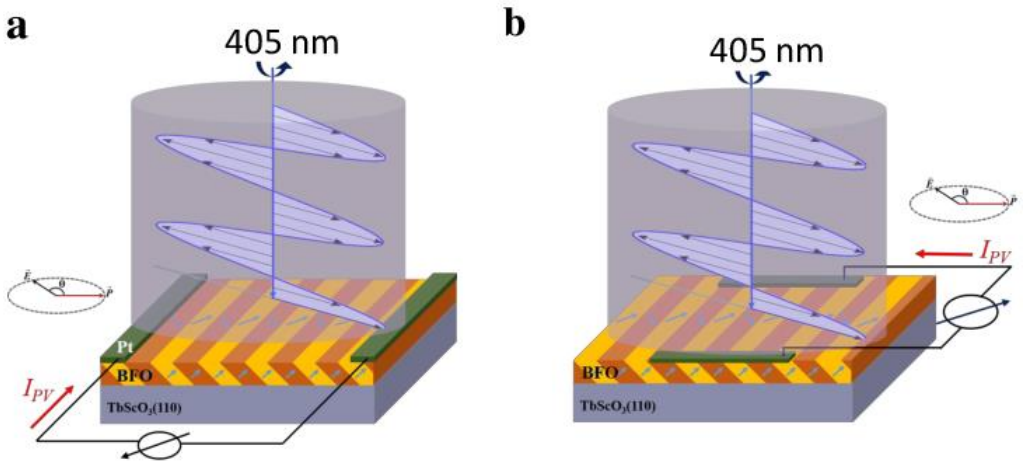

Figure 3-10. In-plane electrode geometry and illumination geometry for macroscopic measurements. Electrodes aligned a) parallel to and b) perpendicular to 71^{O} domain walls.

characterization. For the former one, linearly polarized light with a wavelength of 405 nm illuminates the BFO surface between the coplanar electrodes along the surface normal direction. Then, current-voltage characteristics and light polarisation dependence of the photovoltaic effect were characterized at various temperatures.

For the latter measurement, we have used a white light source, viz. a 100 W Xe lamp, and a monochromator (Oriel Cornerstone 130) to illuminate the sample. The wavelength of the light was sequentially varied from 700 nm to 300 nm with a 5 nm spectral resolution. The white light source was calibrated beforehand by measuring its spectral power distribution using a silicon photodiode (Hamamatsu). The spectral distribution of the photocurrent was obtained after subtracting the values of the dark current from the photocurrent and dividing the result by the lamp spectral power distribution. Finally, in order to compare the photo-response for all samples, the spectral distribution was normalized to its maximum value.

The photoelectric properties at the nanometre levels are characterized by the home-built PhAFM.

Chapter 4. Electronic Origin of the Bulk Photovoltaic Effect

The existence of the anomalous photovoltaic effect in $BiFeO_3$ single crystals, respectively a large short-circuit photocurrent and open-circuit photovoltage significantly larger than the band gap, is directly correlated to the presence of photoelectrically active sub-band gap levels situated between 2.0 eV and 2.5 eV. These levels, which are showing a strong activity in the photoconductive mode, are largely damped in the photovoltaic mode. The correlation between the photoelectric activities of the levels situated around 2.2 eV in the band gap and the existence of the anomalous photovoltaic effect suggests that these sub-band levels are at the electronic origin of the anomalous photovoltaic effect in $BiFeO_3$. The photoelectric activity of sub-band gap levels shows strong temperature dependence. We also found that through thermally and electrical treatments to pump these sub-band levels, both photocurrent and photovoltage could be effectively tuned.

4.1 Introduction

The recent discovery of the anomalous photovoltaic effect (APV) in epitaxial BFO films has largely revived the field of photoferroelectric materials[8,84]. Initial reports attributed the APV effect in BFO films to an efficient separation of photo generated carriers at the domain walls[11], but subsequent studies performed at microscopic and macroscopic scale revealed the actual mechanism behind the APV is the BPV effect[12,47]. The BPV effect in the past has been studied in other non-centrosymmetric materials, which are also ferroelectrics, such as $BaTiO_3$ [85], $LiNbO_3$ [36] and $KNbO_3$[86]. As stated previously, theoretical studies based on an analysis of the Boltzmann transport equation [45] and first principles calculations[87] predict primarily two conditions for the manifestation of the BPV effect. Firstly, an asymmetric generation of charge carriers in *k*-space is required that is realized due to the non-centrosymmetric structure of ferroelectric materials. Secondly, the recombination processes must proceed in ways that are different from the carrier excitation processes. In other words, the recombination processes must occur in ways that do not involve mere band-band transitions[45]. The activity of sub-band gap levels can play a crucial role in fulfilling the second condition. Hence, it is rather essential to study the presence and activity of these levels within the BFO band gap. Studies have shown the existence of sub-band gap levels in BFO[88-90] but their activity and influence on transport properties have been largely overlooked. Nevertheless, the effect

of these levels on the generation and recombination time constants of the photogenerated carriers in microscopic scale has been previously explored[47].

The APV effect has been extensively studied in BFO thin films but there are relatively fewer reports on single crystals. Also, the reports are contradictory regarding the primary characteristic of APV effect, i.e. appearance of an above bandgap V_{OC} under illumination. Most of the reports on single crystals showed values of V_{OC} that are well below the energy of the band gap (~ 2.7 V)[40,91,92] and only a few show values that are significantly above the band gap[46]. Moreover, the previous studies pertaining to the switchable photocurrent and the V_{OC} primarily attributed the effect to switching of polarisation[11] and interfacial effects[91-93]. Thus the question about the origin of this effect and the discrepancies between different explanations is obvious and must be answered to exploit the true potential of this effect. The present work addresses precisely this issue by studying the spectral distribution of the photoconductivity and photovoltaic effect along with their temperature dependence. We focus on the sub-band gap features and correlate their activity to APV effect in BFO single crystals that were obtained from different growth processes and sources. We eventually demonstrate that the short-circuit photocurrent I_{SC} and V_{OC} can be effectively tuned by pumping the sub-band gap levels via thermal and electrical field treatments.

4.2 $BiFeO_3$ Single Crystal Preparation

The crystals were grown from a Bi_2O_3/B_2O_3 flux and stoichiometric $BiFeO_3$ corresponding to the 0.8/4/1 $B_2O_3/Bi_2O_3/Fe_2O_3$ mole ratio. The starting mixture (+99.999% pure) was homogenized in a platinum crucible for 12 hours at 1170 K and subsequently cooled at a rate of 0.01K/min through the liquidus temperature of 897 K to 893 K, followed by cooling to the ambient temperature at a rate of 0.1K/min. Except crystal C5 in Table 4-1, which was a (110)-grown crystal as described in *Ref.* 94, all in-house crystals were rosette-like millimetre large single crystals grown on top of the melt.

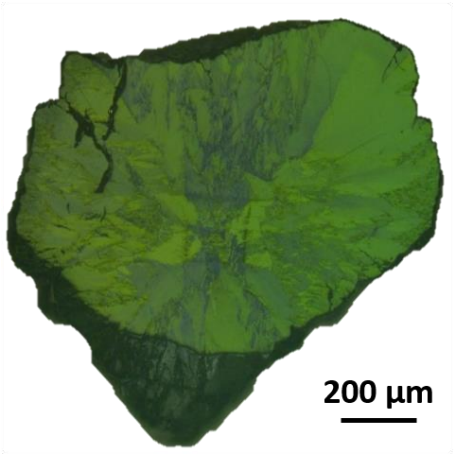

Figure 4-1. An example of the $BiFeO_3$ single crystal used in this study.

The crystals were harvested from the flux using diluted (10%) HNO_3 and further processed by polishing (see Fig. 4-1). The structural properties and domain pattern of typical crystals have been previously reported[94]. Crystal C4 is similar (same batch and processing) to the crystal used in *Ref*. 46. Crystal C3 was grown by Colson/Viret, as given in *Ref.* 95. Crystal C5 was among the first BFO crystals grown by Kubel and Schmid[94]. Both C3 and C5 crystals were largely single domain and details related to the structure and domain pattern are given in the respective cited papers. Photoelectric measurements were performed using in-plane silver electrodes with a defined gap of about 250 μm. The thickness and material of electrodes were proven not to have a major influence on the photoelectric properties.

4.3 Results and Discussion

4.3.1 Role of Sub-bandgap Levels in the Bulk Photovoltaic Effect

The APV effect was measured in all the crystals by acquiring the current-voltage (*I*-*V*) characteristics (Fig. 4-2) under illumination from a laser with a wavelength of 405 nm ($h\nu = 3.06eV$) and an average power intensity of 40 mW/cm^2. The time interval between two points of measurement was long enough to allow stabilization of the photocurrent. BFO single crystals exhibited substantial APV effect and other photoelectric characteristics with V_{OC} varying from 0.5V to 51V depending on the crystals. The details have been summarized in Table 4-1.

The V_{OC} is an extrinsic property of the APV effect and depends upon the photocurrent density (J_{PV}), dark conductivity (σ_d) and photoconductivity (σ_{ph}) that are related by the following equation given by Fridkin[9]:

$$V_{OC} = J_{PV}\left(\frac{1}{\sigma_d + \sigma_{ph}}\right)L \qquad (4\text{-}1)$$

where L is the device length, i.e. the gap between the electrodes.

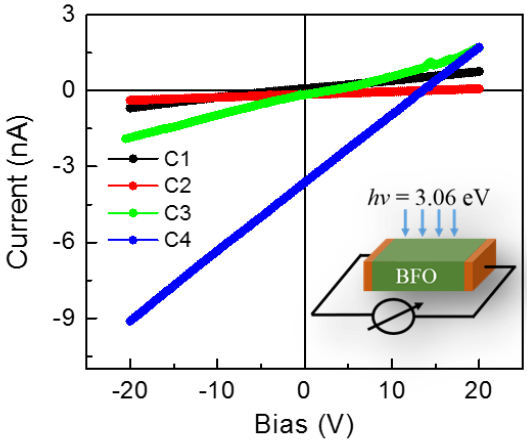

Figure 4-2. Current-voltage characteristics of $BiFeO_3$ single crystals obtained in different growth runs and from different sources. The insert shows the measurement setup schematically.

Table 4-1 The photoconductive properties and V_{OC} of the BFO single crystals

Sample	Orientation	I_{PV} (nA)	σ_{ph} (nA/V)	V_{OC} (V)	σ_d (pA/V)
C1	(100)	0.078	0.03	2.5	0.9
C2	(110)	0.155	0.012	13.75	0.16
C3	(100)	0.165	0.08	2.75	3.4
C4	(110)	3.63	0.27	13.5	0.4
C5	(110)	0.150	0.1	0.5	6.9
C6	(100)	0.147	0.0025	51	0.34

In order to gain further insights into the APV effect in BFO single crystals, we measured the spectral distribution of the photoconductive response, as shown in Fig. 4-3a. The spectral distribution of the photoconductive response shows some intriguing characteristics. Firstly, there is a significant signal at all the wavelengths, including in the region that lies within the band gap of BFO (2.7 eV/460 nm). Secondly, the maximum signal in all the samples is at (375±5) nm (~3.3 eV), which is larger than the band gap. This is most probably related to the carrier recombination at the illuminated surface rather

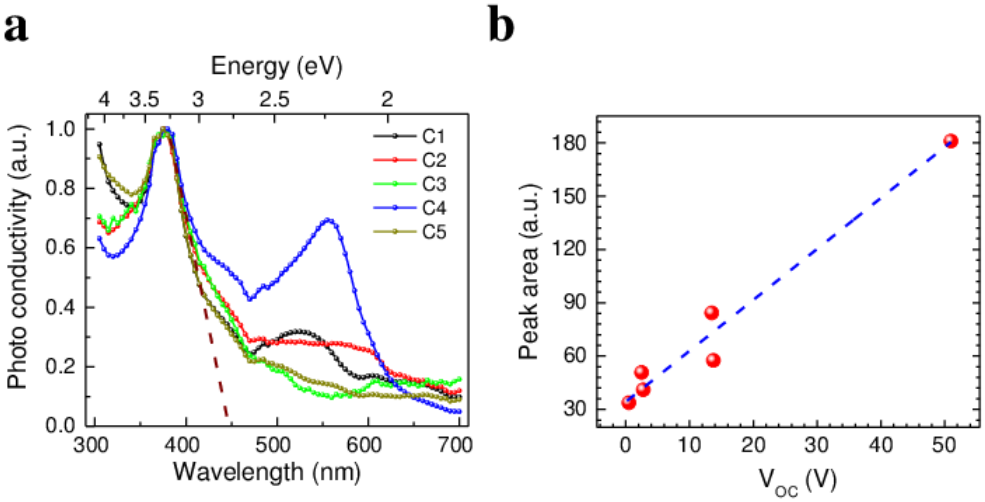

Figure 4-3. (a) Normalized spectral distribution of the photocurrent measured in photoconductive mode with a 20V bias. The dashed line represents the linear fitting of the rising part of the photoconductive response just below 375nm. (b) Open-circuit voltage V_{OC} plotted against the area under the peak which appears between 470 nm and 700 nm in the spectral distribution shown in (a).

than the direct band gap transitions[96]. Nevertheless, the linear fit of the rising part of the signal intercepts the axis of the wavelength at 450 nm (2.8 eV), which agrees quite well with the band gap of BFO. Third and most important, there is a strong sub-band gap signal in the region between 475 nm and 700 nm, which, as we will show, is directly related to the value of V_{OC}. The distribution of the signal within this range varies from sample to sample: from a very sharp peak to a broad distribution or a very low level signal. This signal is related to the presence of sub-band gap levels and is due to the transitions that occur via the levels situated between 2 eV and 2.6 eV, with peak at about 2.2 eV resulting in generation of non-equilibrium carriers and thus photoelectric signal. This rather broad distribution in energy indicates the presence of a band of levels.

The existence of sub-band gap levels in BFO has already been proven via optical investigations. A broad photo-induced absorption peak centred around 540 nm has been observed in optical absorption measurements[97]. Time resolved photoluminescence (PL) measurements on BFO crystals revealed a sharp peak at 2.65 eV which is embedded in a broadband (2.3-2.85 eV) PL signal[98]. Noticeably, the broadband PL peak resembles rather well the photo-response presented here. Moreover it suggests that these sub-band gap levels might also act as radiative recombination centres in certain conditions. Cathodoluminescence (CL) studies on BFO thin films confirmed that the electronic structure of BFO comprises of a number of sub-band levels situated at 2.0, 2.2 and 2.5 eV, among which the 2.5 eV seems to be rather insensitive to the in-plane strain induced by the substrate, the fabrication method and oxygen deficiency[88].

Our present data confirm the existence of these levels in BFO single crystals and show that these levels are not mere radiative recombination levels. A direct correlation is obtained by plotting the values of V_{OC} against the area under the sub-band gap signal (see Fig. 4-3b), which might be related to the total density of the sub-band photoelectrically active levels. The plot reveals a direct relationship between the sub-band levels and the APV effect, particularly with the actual value of V_{OC}. The BFO single crystals show an APV effect whenever these levels are photo-electrically active. This explicitly suggests that these sub-band gap levels, especially the ones around 2.2 eV, assist in fulfilling the second condition of the BPV effect and are at the electronic origin of the APV effect. We suppose that these levels, depending upon the effective position of the quasi Fermi level (E_{Fn}) are acting either as simple recombination levels (ground levels) or as trapping levels. As soon as these levels transform into trapping levels, they become photoelectrically active and induce an asymmetry in *k*-space, which is required for the BPV effect. Incident

photons ($h\nu$=3.06 eV) excite non-equilibrium carriers via band-band transitions, which in a short period of time are trapped by these sub-band gap levels. Thereafter, the photoconductive current is not simply due to the band-band transitions but proceeds via these levels. The levels contribute to the photoconduction by trapping and re-emitting the carriers in the allowed bands. We assume that these sub-band gap levels, involved in the electronic transport, are at the origin of the shift-current, and the eventual photocurrent[87].

Additional support to this mechanism is provided by the spectral distribution of the short-circuit photocurrent I_{SC} measured at zero applied bias and only due to the APV effect, as shown in Fig. 4-4. From the spectral distribution of the I_{SC}, it can be easily seen that the maximum in the response appears in the same spectral range as the photoconductive distribution. The linear extrapolation of the rising part of the main peak results in the same band gap values, but the sub-band gap signal is largely supressed. This suggests that the carriers excited with energies lower than the bandgap of BFO, i.e. excited directly to the sub-band gap levels, will not generate significant photocurrent due to the fact that the recombination process proceeds mostly in the same way as the exciting process. Hence one fundamental condition which is required for BPV effect, respectively that the carrier recombination path should be different as the excitation path, is not fulfilled.

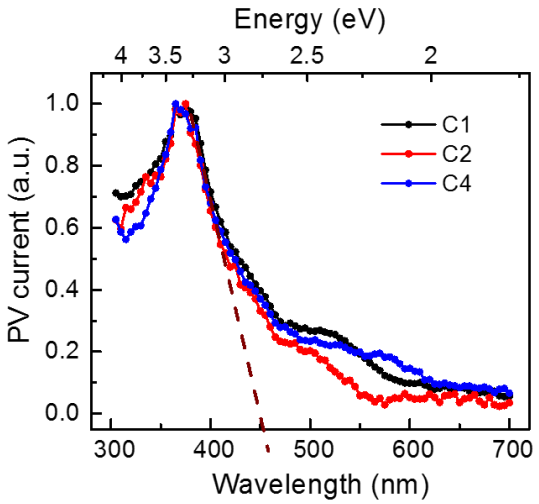

Figure 4-4. Spectral distribution of the photovoltaic current for the BFO crystals showing sizable I_{SC} and V_{OC}.

4.3.2 Temperature Dependent Activity of Sub-bandgap Levels

It is known that the occupancy of the sub-band gap levels is largely determined by the position of the E_{Fn} in the band gap. Therefore, the character of a level that lies in the vicinity of the E_{Fn} can change due to a small variation in the position of E_{Fn} [99]. In order to validate such a behaviour of the sub-band gap levels in our crystals, we measured the spectral distribution at different temperatures up to 440 K, which is shown in Fig. 4-5a. The value of the band gap, calculated by extrapolation, remains the same at all temperatures. However, the photoconductive signal measured between 470 nm and 700

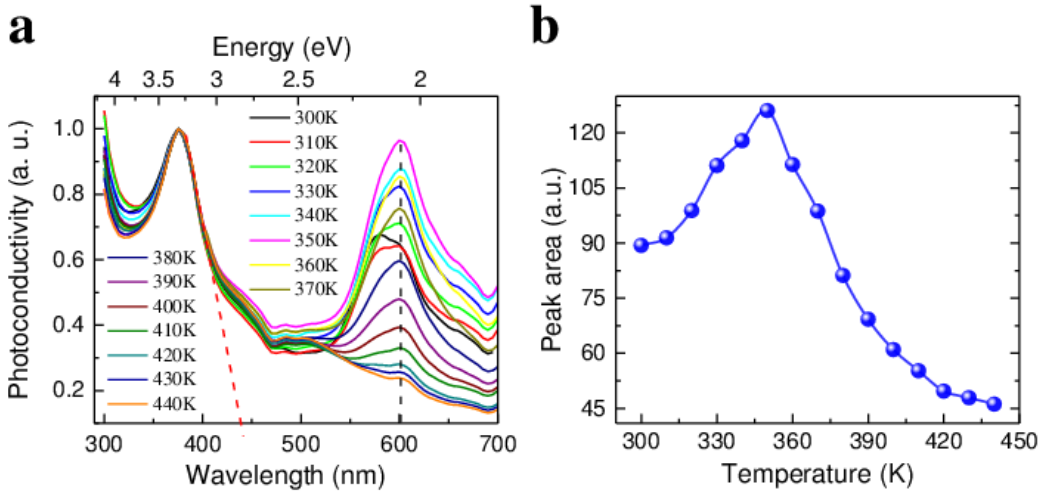

Figure 4-5. (a) Normalized spectral distribution of the photocurrent measured in the photoconductive mode (20V bias) spanning from 300K to 440K. (b) The variation of the peak area under spectral distribution in (a) calculated from 470nm to 700nm.

nm, which is due to the activity of the sub-band gap levels, varies massively with temperature. While the peak position did not change with the temperature, the area under the sub-band gap level signal increases till 350 K and then tends to decrease with further increase in temperature, as shown in Fig. 4-5b.

The increasing trend of the peak area between 300 K and 350 K evidently shows the role of the position of E_{Fn} in determining the occupancy of the levels. The E_{Fn} tends to move towards the middle of the bandgap with an increase in temperature, transforming ground levels just below the E_{Fn} into trapping levels. As a result, the carriers previously captured in the ground levels are freed and contribute to conduction, which is visible as an increase in the signal. As the E_{Fn} continues to move towards the middle of the band gap with increasing temperature, the trapping levels transport all the carriers into the allowed bands and eventually transform into shallow ionized levels. Thereafter, their role in the photoconduction is largely supressed. Additionally, the evolution of photocurrent I_{SC} with temperature

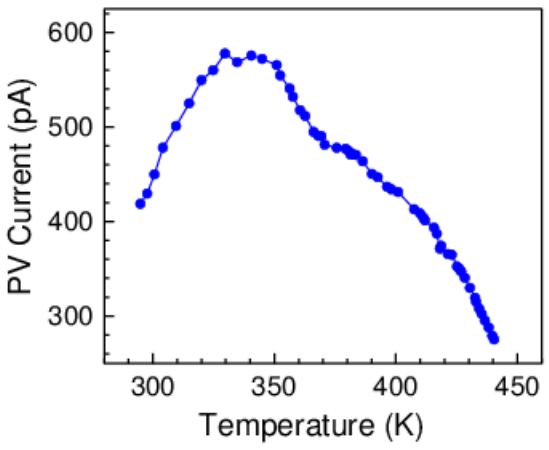

Figure 4-6. Temperature dependent photovoltaic current I_{PV} between 295K and 440K.

was measured and is shown in Fig. 4-6. The I_{SC} increases with temperature, reaching its maximum at around 350K, and then tends to decrease with further increase in temperature. Note that the evolution of I_{SC} with temperature resembles the variation of sub-band peak area shown in Fig. 4-5b, which further confirms the essential role of sub-band levels, situated at around 2.2 eV, in the appearance of BPV effect.

It must be mentioned here that the effective position of E_{Fn} can depend upon a variety of factors such as purity of raw materials, processing methods, contamination, etc. Hence, the diverse and contradicting reports about the photovoltaic properties of BFO can be largely attributed to the uncertainty in the position of E_{Fn}.

4.3.3 Tailoring the Bulk Photovoltaic Effect via Sub-bandgap Levels

Keeping in perspective this temperature dependent occupancy of the sub-band levels, one might also perceive here the possibility to modulate the APV effect, including the V_{OC}. It can be predicted that a combination of temperature and electric field treatment, that will modify the occupancy of these levels and implicitly the position of E_{Fn} at room temperature, would affect massively the activity of the levels and hence the APV effect, i.e. I_{SC} and V_{OC}.

In order to verify this hypothesis, we used a BFO single crystal that exhibited in its pristine state a V_{OC} of -28 V, which is well above the band gap. The crystal was then subjected to a controlled set of thermal and electric field treatments. The *I-V* plots

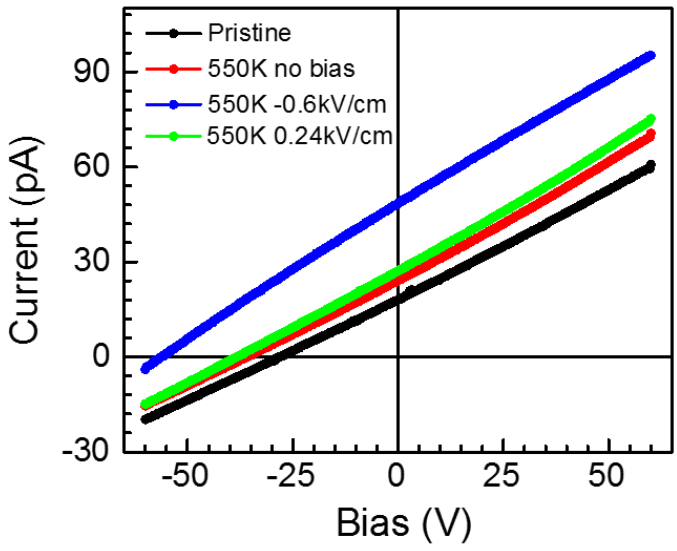

Figure 4-7. Photo *I-V* curves from $BiFeO_3$ single crystal after different thermal-electrical treatments.

acquired at room temperature under illumination after the treatments are shown in Fig. 4-7. In all the thermal treatments the sample was heated to 550 K at 5 $Kmin^{-1}$ and cooled down to room temperature at the same rate. It was mentioned before that one of the necessary conditions for the appearance of the APV effect is the availability of empty states in the levels within the band gap. By heating the sample to a high temperature, E_{Fn} moves towards the middle of the band gap and trapped carriers could be thermally excited and recombined. Hence after heating the sample the APV effect must be enhanced due to the downward shift of E_{Fn} and the availability of larger number of empty states at room temperature, as schematically shown in Fig. 4-8.

This is indeed the case, and the V_{OC} increased to -36 V (red line in Fig. 4-7). Additionally, the states in the sub-band gap levels can be further emptied or filled by the application of an electric field simultaneously with the thermal treatment, similar to the one used in trap level spectroscopy[100]. This was performed by applying a small bias field of -0.6 $kVcm^{-1}$ while cooling the sample. As a result of this treatment, the V_{OC} value increased to -56 V. A reversal of this process can also be envisaged when an electric field of opposite polarity will cause filling up of the states in the levels and therefore reduce the APV effect. We have demonstrated such a scenario by applying +0.24 $kVcm^{-1}$ while cooling the sample. This caused the V_{OC} to drop to -38 V (green curve in Fig. 4-7).

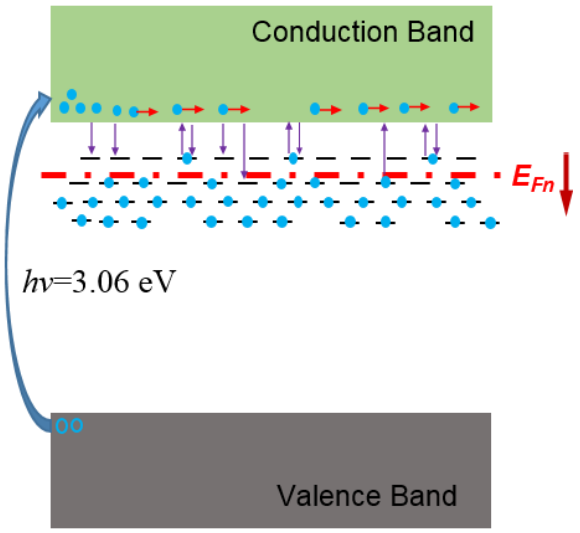

Figure 4-8. Band diagrams to depict the evolution of the quasi Fermi level (E_{Fn}) position with respect to the sub band gap levels after thermal-electrical treatments.

Additionally, the thermal-electrical treatment also modifies the sub-band signal in the photoconductive response, and is shown in Fig. 4-9. The sample was heated to 550 K and cooled, under a bias field of 0.5 kV/cm. There is an evident drop in the photoconductive response from the sub-band levels after the treatment. The drop should also result in a lower V_{OC} as confirmed in Fig. 4-7.

It must be mentioned here that the electric fields applied across the sample for these measurements are well below the reported values of coercive fields for BFO, so an influence of the ferroelectric polarisation is largely ruled out. The above experiments show the possibility to tune the photovoltaic effect, especially the value of V_{OC}, by tuning the occupancy of the sub-band levels and not by ferroelectric switching. This suggests that the electronic mechanism behind the switchable photovoltaic effect discovered in BFO and other ferroelectric materials might be the same as presented here, since the charge injection during high field ferroelectric switching might be massive and modify the occupancy of the sub-band levels.

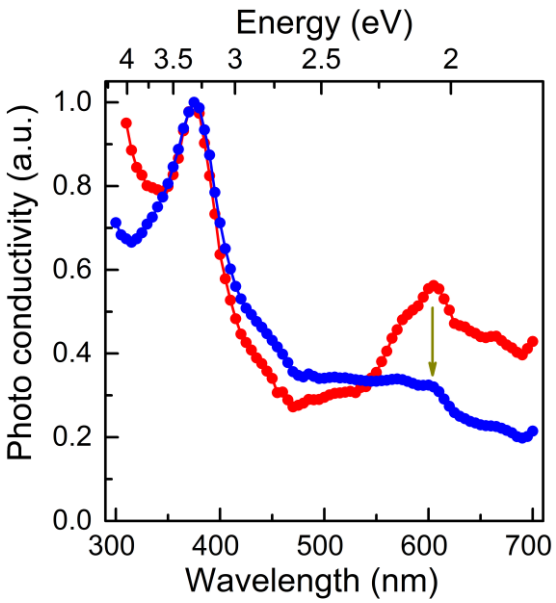

Figure 4-9 Photoconductive response of $BiFeO_3$ single crystal before (red line) and after (blue line) the thermal-electrical treatment, respectively heating up to 550K and cool down with a positive 0.5kV/cm electrical field.

4.4 Conclusion

We have shown that the spectral distribution of the photoconductive response in $BiFeO_3$ single crystals involves an important sub-band gap response in the range of 2.0-2.6 eV with a strong peak near 2.2 eV. This strong sub-band gap photoelectric response is due to the activity of sub-band gap levels. There is a direct correlation between the response in this spectral range and the existence of the anomalous photovoltaic effect, which suggests that the sub-band gap levels are at the electronic origin of APV effect in $BiFeO_3$. The occupancy of these levels plays a dominant role in the appearance and value of the photovoltaic current and above band gap V_{OC}. This allows an effective tailoring of the V_{OC} by modifying the occupancy of these sub-band levels with a controlled scheme of thermal and electric field treatments.

Chapter 5. Bulk Photovoltaic Effect in Monodomain $BiFeO_3$ Thin Films

In this Chapter, by studying monodomain $BiFeO_3$ thin films with only a single ferroelectric variant, we demonstrate that the photovoltaic current of $BiFeO_3$ ferroelectric semiconductor possesses a preferred direction depending on the light polarisation direction and working temperature, which is not along the ferroelectric polarisation direction. The results indicate that the bulk photovoltaic effect originates from non-centrosymmetry of ferroelectric semiconductors but is independent of the ferroelectric polarisation. Moreover, we showed that the bulk photovoltaic effect can be tailored by modifying the activity of sub-band gap levels via chemical doping, thus enhancing the power conversion efficiency in ferroelectric semiconductors.

5.1 Introduction

In principle, ferroelectric (FE) materials give rise to two kinds of the PV effects based on different charge separation mechanisms. On the one hand, as a wide bandgap material, a Schottky barrier always forms at its interface with most metals[38,39]. The built-in field developed within the depletion region of the barrier separates photo-excited carriers leading to a spontaneous PV current under illumination[40,41]. The direction of the PV current can be switched by applying an electrical field due to the inherent correlation between the barrier profile and the FE polarisation charges[101]. On the other hand, FE materials due to their non-centrosymmetric structures exhibit also the BPV effect, which exhibits two distinctive features [36,102,103]. It has been recently shown that the BPV effect of FE semiconductors has the potential to boost the solar energy conversion efficiency and even to overcome the Shockley–Queisser limit[104].

In contrast to the classic PV effect in a Schottky barrier, the correlation between the BPV effect and the FE polarisation remains largely unresolved and the reported results are contradictory. Seidel *et al.*[37,105] reported a large V_{OC} with a PV current of opposite direction to that of FE polarisation in BFO films whereas Akash *et al.*[12] and first principle calculations[87] showed the PV current to be parallel to the FE polarisation. Moreover, in the case of BFO films, the coexistence of different FE polarisation variants and associated FE domain walls in a single FE device precludes revealing the innate characteristics of

the BPV effect[12,37,106,107]. Therefore, for a better understanding of the BPV effect, it is crucial to study the BPV effect in a system consisting with only a single FE polarisation variant excluding the influence of domain walls. To that end, we studied the relationship between the BPV effect and the FE polarisation through the temperature-resolved BPV effect of monodomain BFO thin films. The PV properties of monodomain BFO films were characterized in a wide temperature range with electrodes running either parallel or perpendicular to the FE polarisation direction. We also studied the tunability of the PV current and V_{OC} by varying the illumination parameters and temperature, as well as chemically doping the BFO films.

5.2 Monodomian $BiFeO_3$ Thin Film Preparation

Nominally 200 nm thick (001)-oriented BFO thin films were deposited epitaxially on bare $SrTiO_3$ (001) substrates by pulsed laser depositio. In order to get monodomain BFO films with only one ferroelectric variant, we used $SrTiO_3$ substrates with a 4° miscut along the [110] direction[108]. The growth parameters of monodomain BFO films were given in Table 3-1.

To study the PV effects of the monodomain BFO films, we fabricated on the BFO films two sets of in-plane platinum electrodes with a gap of 80 μm and a length of 0.5 mm running either perpendicular or parallel to the in-plane FE polarisation direction. As shown in Fig. 5-1, the first configuration with electrodes perpendicular to the polarisation

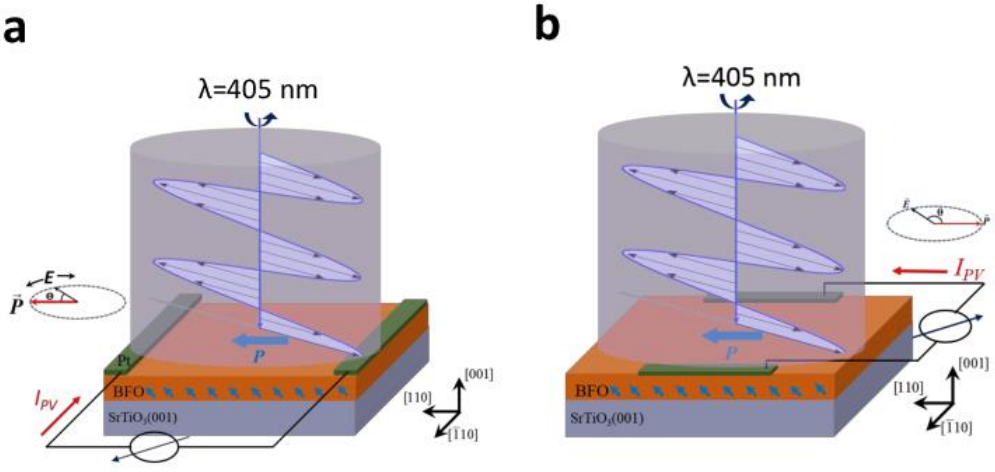

Figure 5-1. Schematics showing the measurement geometries with in-plane electrodes running (a) perpendicular and (b) parallel to the ferroelectric polarisation, respectively.

was to investigate the PV current parallel or antiparallel to the polarisation while the second configuration with electrodes parallel to the polarisation was to investigate the PV current perpendicular to the polarisation. A linearly polarized laser of a wavelength of 405 nm ($h\nu$=3.06 eV) was used to illuminate the BFO films along the direction normal to the film surface.

5.3 Results and Discussion

5.3.1 Crystallographic and Domain Structure Characterization

Fig. 5-2a shows the out-of-plane XRD 2θ-ω scan of the BFO film grown on the high miscut $SrTiO_3$ substrate. The strong (*00l*) (*l*=1, 2, 3) diffraction peaks indicate that the deposited BFO film is epitaxially crystallized. In order to check the structure variants in the BFO film, we performed the RSM near the $\{113\}_{pc}$ peak family at various phi angles[108]. Due to the large rhombohedral distortion of BFO crystallographic lattice ($\alpha=\beta=\gamma=89.4^{O}$), the peak positions of $(113)_{pc}$, $(1\text{-}13)_{pc}$ (same as the $(\text{-}113)_{pc}$) and $(\text{-}1\text{-}13)_{pc}$ should be distinguished from each other as demonstrated in Fig. 5-2b. The ferroelastic variants are intrinsically correlated with the structure distortions. A homogeneous crystallographic distortion, namely a single ferroelastic variant in the BFO film, will give rise to a single $(113)_{pc}$ peak at a certain phi angle, as demonstrated in Fig. 5-2c-f. This indicates that there is only one ferroelastic variant in the BFO/STO film.

The piezoresponse force microscopy (PFM) confirmed the single domain structure of the BFO films. The BFO films exhibit a relatively smooth surface morphology (Fig. 5-3a) and a uniform in-plane and out-of-plane PFM phase signal, indicating an outwards out-of-plane polarisation and in-plane polarisation running along the [110] direction over the whole film (Fig. 5-3b and 5-3c).

5.3.2 Temperature-resolved Bulk Photovoltaic Effect

To check the manifestation of the BPV effect in the monodomain BFO film, we first measured the light polarisation dependence of the PV current with in-plane electrodes running perpendicular to the in-plane FE polarisation (for simplicity, referred to perpendicular geometry). The PV current, namely the short-circuit photocurrent under

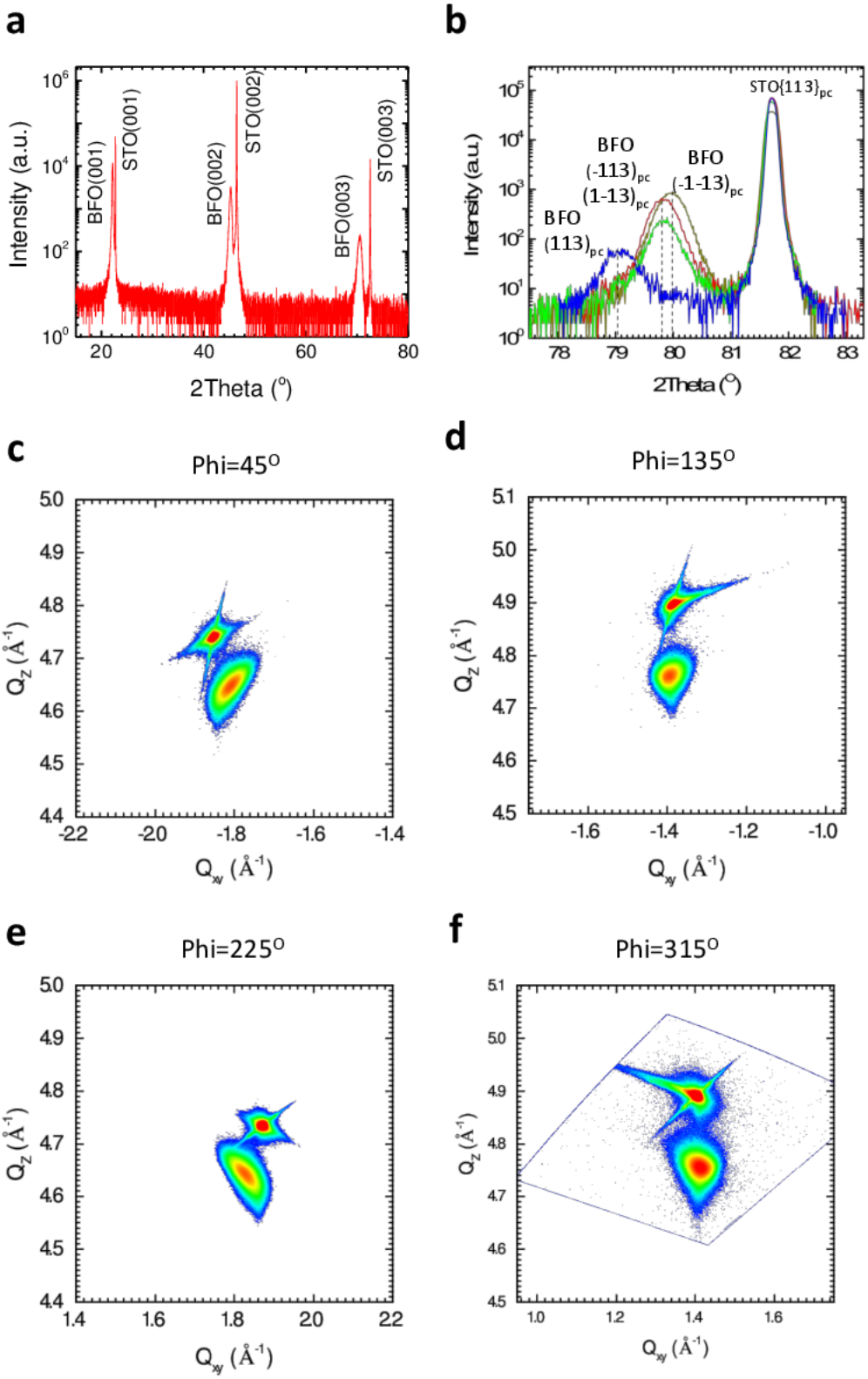

Figure 5-2. Structural characterization of the monodomain $BiFeO_3$ thin film. (a) XRD 2θ-ω scan along the out-of-plane direction. (b)XRD 2θ-ω scan of the BFO {113} peak family. (c-d) RSMs of the monodomain $BiFeO_3/SrTiO_3$ heterostructure near {113} $SrTiO_3$ peaks with different phi angles.

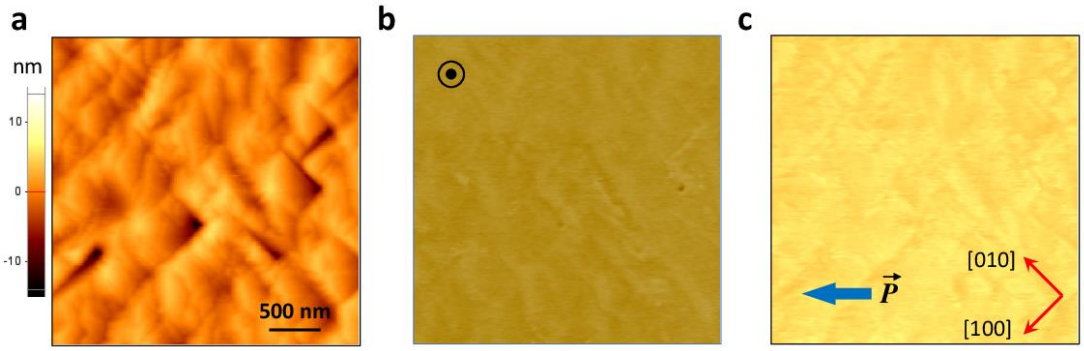

Figure 5-3. Domain structure characterization of monodomain $BiFeO_3/SrTiO_3$ film. (a) Topography, (b) the out-of-plane and (c) in-plane PFM phase signal.

illumination, is measured by an electrometer without applying external bias. The magnitude of the PV current was recorded simultaneously while rotating the angle θ between the light polarisation and the in-plane FE polarisation via a half-wave plate. The light intensity was kept constant during the measurement. Note here that the current running in the same direction as the FE polarisation is defined as positive, and negative when it is antiparallel to the FE polarisation. As clearly depicted in Fig. 5-4a, the PV current exhibits an angular dependence on the light polarisation with a period of 180° within the whole temperature range. This light polarisation dependence of the PV current is a unique feature of the BPV effect, which can be expressed as: [1]

$$I_i = I_{light} A \boldsymbol{\beta}_{ijk} \boldsymbol{e}_j \boldsymbol{e}_k \tag{5-1}$$

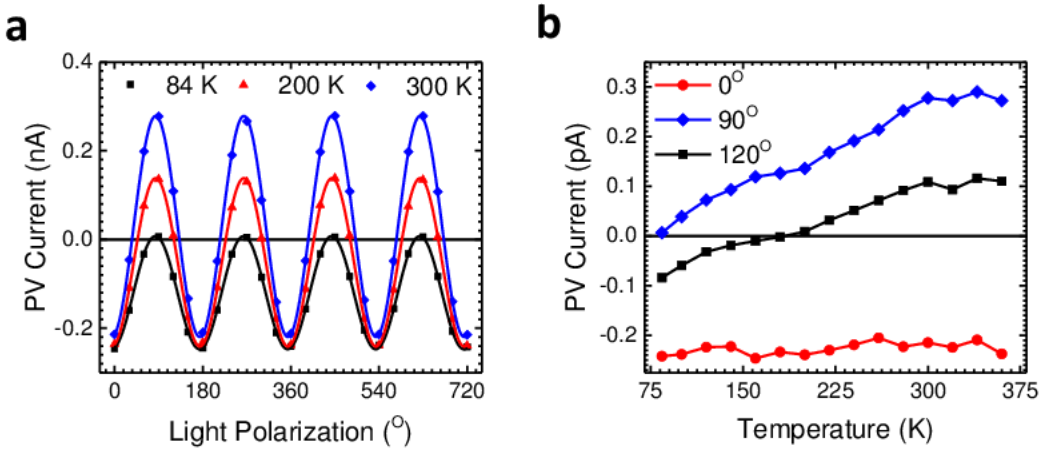

Figure 5-4. (a) The dependence of the PV current on the angle between the light polarisation and the in-plane FE polarisation with in-plane electrodes perpendicular to in-plane projection of ferroelectric polarisation. The continuous lines are the fit of experimental data with Eq. 5-2. (b) Temperature-dependent PV current under different light polarisation angles.

where I_i is the PV current along a particular crystallographic direction, I_{light} is the light intensity, A is the electrode area, $\boldsymbol{\beta}_{ijk}$ is the third rank BPV tensor in the rhombohedral coordinate system, $\boldsymbol{e}_j$ and $\boldsymbol{e}_k$ are the projection of the electrical field of the light onto the BFO surface. Regarding the particular crystallographic configuration of the monodomain BFO film, the BPV current along the direction of the in-plane FE polarisation can be predicted as:

$$I_{\perp} = \tfrac{\sqrt{2}}{2} I_{light} A\left[B_{11} + B_{12} - 2B_{16}\cos(2\theta + \varphi_{\perp})\right] \tag{5-2}$$

where $I_{\perp}$ is the PV current collected by the perpendicular electrode geometry, B_{11}, B_{12}, B_{16} are the BPV tensor elements in the lab coordinate system of which relations to $\boldsymbol{\beta}_{ijk}$ are shown in Table 5-1, $\varphi_{\perp}$ is an experimental phase shift. The experimental data measured at various temperatures all fit well with the Eq. 5-2 shown as continuous curves, demonstrating the PV current originates solely from the BPV effect.

Interestingly, the light polarisation dependence of the PV current evolves with temperature. At 84 K, $I_{\perp}$ keeps a negative sign with any light polarisation, indicating that $I_{\perp}$ always runs antiparallel to the in-plane FE polarisation, while the current curves extend to the positive quadrants at higher temperatures (see Fig. 5-4a). Thus, the direction

Table 5-1. Expressions of BPV tensor elements in lab coordinate in terms of 4 independent tensor elements in rhombohedral coordinate

B_{lq}	Expression
B_{11}	$\frac{4}{3\sqrt{3}}\beta_{15} - \frac{4}{3\sqrt{6}}\beta_{22} + \frac{2}{3\sqrt{3}}\beta_{31} + \frac{1}{3\sqrt{3}}\beta_{33}$
B_{12}	$-\frac{2}{3\sqrt{3}}\beta_{15} + \frac{2}{3\sqrt{6}}\beta_{22} + \frac{2}{3\sqrt{3}}\beta_{31} + \frac{1}{3\sqrt{3}}\beta_{33}$
B_{16}	$\frac{2}{3\sqrt{3}}\beta_{15} + \frac{4}{3\sqrt{6}}\beta_{22} - \frac{2}{3\sqrt{3}}\beta_{31} + \frac{2}{3\sqrt{3}}\beta_{33}$

where $\beta_{15} = \beta_{24} = 2\beta_{113} = 2\beta_{131} = 2\beta_{223} = 2\beta_{232}$;

$\beta_{22} = -\beta_{21} = -\beta_{16} = \beta_{222} = -\beta_{211} = -2\beta_{112} = -2\beta_{121}$;

$\beta_{31} = \beta_{32} = \beta_{322} = \beta_{311}$;

$\beta_{33} = \beta_{333}$.

of $I_{\perp}$ at some light polarisation angles, such as 120°, changes its sign from negative to positive just by increasing the temperature (see the black curve of Fig. 5-4b). This temperature-tailored direction of the PV current is unusual as the crystallographic structure and FE polarisation of the BFO films remain constant within the studied temperature range owing to its very high Curie temperature[76]. This implies that the BPV effect is not directly correlated with the FE polarisation as believed in case of the PV effect originating from the interface Schottky barrier. The BPV effect is determined by the internal non-centrosymmetry as well as some additional factors, such as sub-band gap levels induced by structural or electronic defects, the activity of which varies with temperature[103].

The relationship between the BPV effect and the FE polarisation was further investigated by setting the in-plane electrodes running parallel to the FE polarisation (referred to parallel geometry). In this particular geometry, while there is no component of FE polarisation running perpendicular to the electrodes, there is a significant PV current. This PV current (defined here as $I_{//}$) also has a dependence on the light polarisation shown in Fig. 5-5a. Specifically, the PV current is negligible when the light polarisation is parallel to the in-plane FE polarisation whereas the PV current evolves to a positive maximum value when the light polarisation angle is $45°$. Afterwards, the PV current decreases to almost zero at $90°$ and then reaches a negative maximum value at

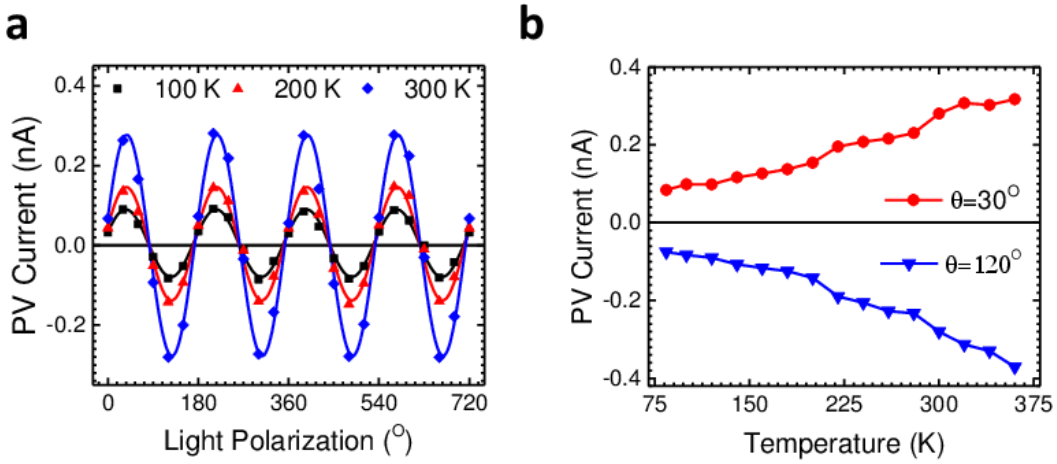

Figure 5-5. (a) The dependence of the PV current on the light polarisation angle with in-plane electrode parallel to in-plane projection of the ferroelectric polarisation. The continuous lines are the fit of experimental data with Equation 3; (b) Temperature-dependent PV current under different light polarisation angles

135° . Moreover, the magnitude of the PV current maxima increases with the temperature (see Fig. 5-5b). This light polarisation dependence can be well fitted by an equation deduced from the BPV theory, which can be expressed as:

$$I_{//} = \frac{\sqrt{2}}{2} A I_{light} (B_{12} - B_{11}) \sin(2\theta + \varphi_{//}) \tag{5-3}$$

where $\varphi_{//}$ is a constant to compensate the angle shift of the in-plane electrode with respective to the in-plane FE polarisation.

In addition, another primary characteristic feature of the BPV effect, i.e., appearance of an above bandgap V_{OC} under illumination, was also studied in both electrode geometries by acquiring current-voltage (*I*-*V*) curves as shown in Fig. 5-6a and 5-6b. The linear light polarisation was set parallel to the FE polarisation in the perpendicular geometry whereas the light polarisation was set to around 45° for parallel geometry. The PV current in the perpendicular geometry always keeps a negative sign and almost

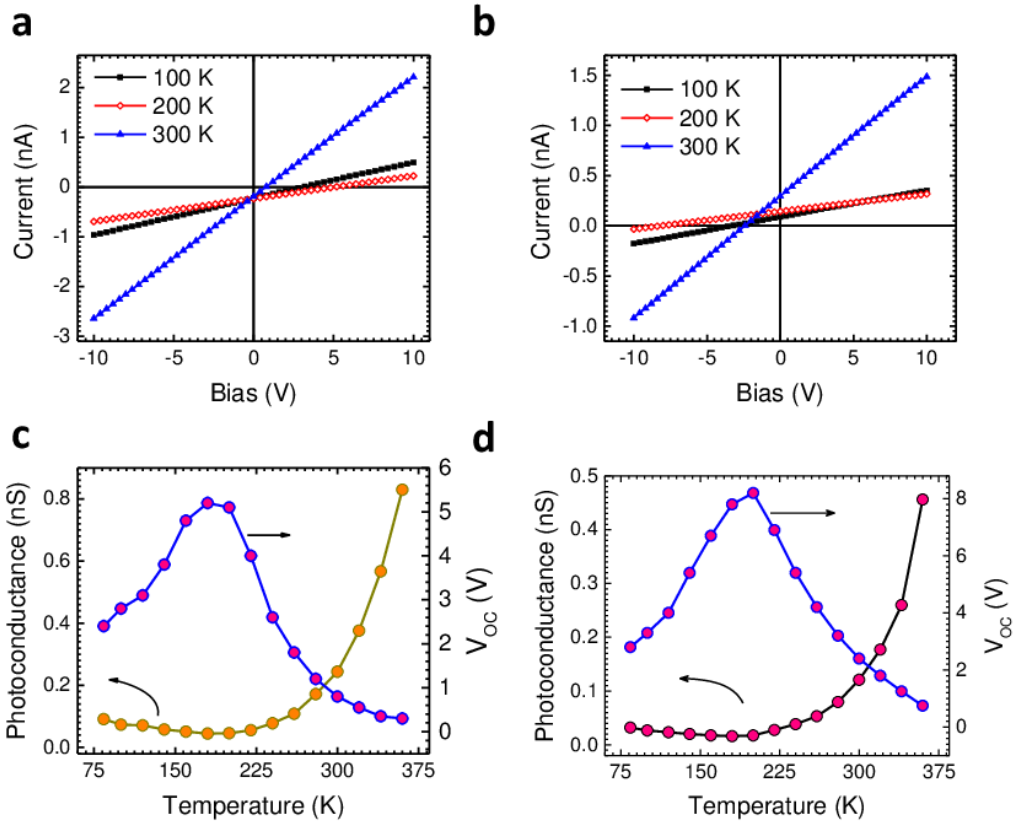

Figure 5-6. (a) Current-voltage (*I*-*V*) characteristics acquired under illumination with light polarisation parallel to the FE polarisation for perpendicular geometry. (b) I-V curves for parallel electrode geometry with light polarisation set to around 45°. Temperature dependent photoconductance and V_{OC} for (c) perpendicular and (d) parallel geometry.

constant values (see the red line of Fig. 5-4b) within the temperature range of interest under the specific light polarisation direction. Meanwhile, the conductance of the BFO film under illumination, namely the slope of the *I-V* curves, decreases with increasing temperature before reaching a minimum at about 200 K and then increases with further raising the temperature, as shown in Fig. 5-6c. Consequently, the V_{OC} of the monodomain FE devices in the perpendicular geometry shows a maximum value of 5.2 V at 180 K and then decreases almost exponentially with increasing temperature (see Fig. 5-6d). Similarly, the V_{OC} in the parallel geometry shows a maximum value of 8.2 V at about 200 K, which is more than twice the value of the forbidden bandgap ($E_g = 2.7$ eV).

The data above clearly show that the BPV effect in the monodomain BFO is characterized by bandgap V_{OC} and PV current direction and magnitude of which depend on the incident light polarisation angle and temperature, but originated from the FE polarisation. This suggests the BPV effect itself is an independent material property of FE similar to the piezoelectric effect. Studying the BPV effects, especially the BPV tensor elements, may offer an alternative insight into the intrinsic physical characteristics, such as the phase transition and the evolution of electronic structure (see Fig. 5-7).

Note that the BPV tensor elements used in this work correspond to the pseudo-cubic coordinate syetem. B_{16} and B_{12} remain negative sign in the studied temperature range and their magnitude increases slightly with temperature. In contrast, B_{11} increases significantly from a negative value at low temperature to a large positive value at room

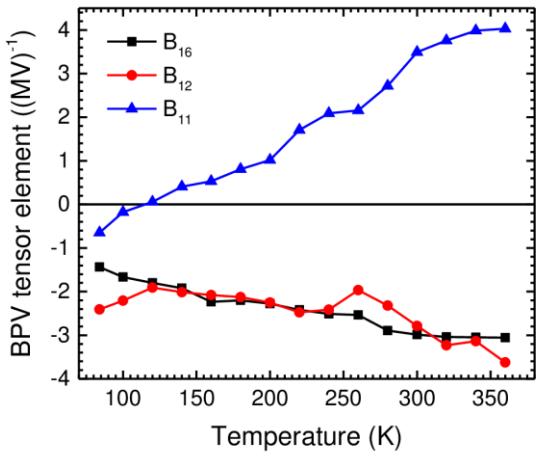

Figure 5-7. The bulk photovoltaic effect tensor elements of the monodomain $BiFeO_3$ film as a function of temperatures.

temperature. The origin of this evolution and its correlation with the electronic structure, however, remains a puzzle and deserves further investigations. Although not induced by FE polarisation, the BPV effect is still correlated with the FE polarisation via the non-centrosymmetric structure. Once the structure changes by external stimuli, such as electric field, both the BPV effect and the FE polarisation are simultaneously modified[37].

5.3.3 Tuning the Bulk Photovoltaic Effect via Chemical Doping

Apart from the crystallographic structure, the BPV effect is also sensitive to the fine electronic structure, especially the sub-bandgap levels[45,103]. The scattered behaviour of the PV current reported in the literature can be ascribed to the different fine electronic structures induced by defects, such as O and Bi vacancies, in the BFO films because of different sample preparation conditions[109]. To prove this hypothesis, a monodomain BFO film with 5% Mn dopant (BFMO) was fabricated with the same conditions as used for pure BFO films to introduce defects and to artificially modify the sub-bandgap levels. In sharp contrast to the pure BFO film, the PV current measured with the perpendicular electrode geometry remains unidirectional irrespective of the light polarisation angle at room temperature (Fig. 5-8a). Moreover, the PV response of the BFMO film is significantly enhanced (Fig. 5-8b). Both the magnitude of the PV current and V_{OC} are increased by a factor of five in comparison to that of the pure BFO film. The Mn dopant,

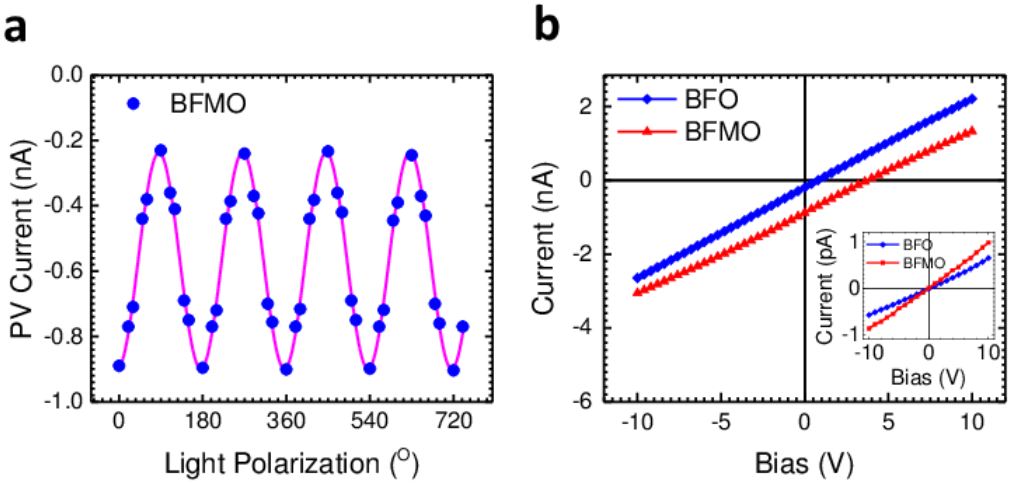

Figure 5-8. (a) The light polarisation dependence of the PV current in 5% Mn-doped $BiFeO_3$ (BFMO) monodomain film with in-plane electrodes running perpendicular to ferroelectric polarisation. Solid lines are the fit of experimental data with Eq. 5-2. (b) Current-voltage characteristics of BFO and BFMO films under illumination; The insert shows the dark *I-V* curve of BFO and BFMO films.

acting most probably as a hole acceptor, modifies substantially the fine electronic structure of BFO film, which accounts for the enhancement of the BPV effect in BFMO film[110]. This is demonstrated by the wavelength-resolved photovoltaic characterization as shown in Fig. 5-9. As compared to the pure BFO film, the BFMO film exhibits an enhanced PV response below λ=535 nm ($h\nu$=2.3 eV), confirming the activation of the sub-band levels by the Mn-doping. This massive enhancement in the visible range obtained by chemical doping is highly relevant for potential application in energy harvesting.

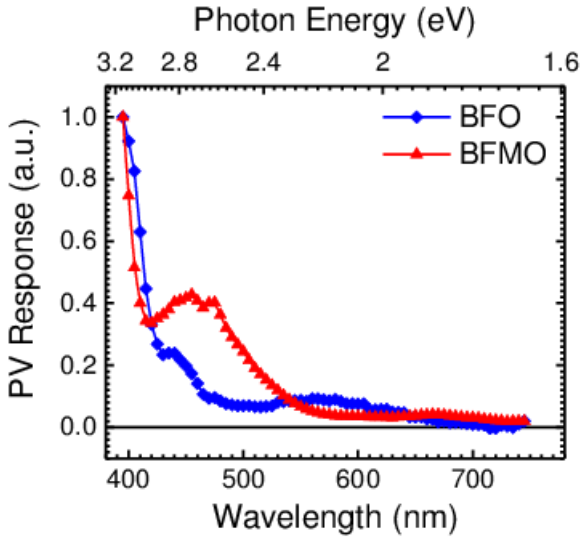

Figure 5-9. The spectral distribution of normalized photovoltaic response of the $BiFeO_3$ film (blue line) and the $BiFe_{0.95}M_{0.05}O_3$ film (red line), respectively.

5.4 Conclusion

The PV properties of monodomain BFO films have been systematically studied. The BPV effect is shown to be an independent characteristic property of non-centrosymmetric structure rather than originated from the ferroelectric polarisation. The PV current originated from the BPV effect exhibits tunable directions depending on the incident light polarisation and temperatures. Moreover, the BPV effect can be effectively tailored by tuning the activity of sub-band levels through chemical doping, hence enhancing the net PV response of BFO in the visible range of the light spectrum.

Chapter 6. Role of Domain Walls in the Bulk Photovoltaic Effect

Domain walls, which are intrinsically two dimensional nano-objects exhibiting nontrivial electronic and magnetic behaviours, have been proven to play a crucial role in photovoltaic properties of ferroelectrics. Despite this recognition, the electronic properties of domain walls under illumination until now have been accessible only through macroscopic studies and their effects on the conduction of photovoltaic current still remain elusive. The lack of understanding hinders the development of nanoscale devices based on ferroelectric domain walls. Here, we directly characterize the local photovoltaic and photoconductive properties of 71° domain walls in $BiFeO_3$ thin films with nanoscale resolution. The local photovoltaic current, proven to be driven by the bulk photovoltaic effect, has been probed over the whole illuminated surface by using a specially designed photoelectric atomic force microscope and found to be significantly enhanced at domain walls. Additionally, spatially resolved photoconductive current distribution reveals a higher density of excited carriers at domain walls in comparison with domains. Our measurements demonstrate that domain wall enhanced photovoltaic current originates from its high conduction rather than the internal electric field. This photoconduction-facilitated local photovoltaic current is likely to be a universal property of topological defects in ferroelectric semiconductors.

6.1 Introduction

Domain walls (DWs) in ferroelectrics have attracted increased attention in recent years owing to their unique physical properties, such as enhanced electronic conduction[111-114], magnetoelectric coupling[29,115], and the capability of the manipulation by external electrical, magnetic or strain field[107]. Additionally, DWs play a crucial role in the macroscopic properties of their host materials, such as polarisation switching[116], permittivity[117] and pyroelectric properties[118]. In particular, they have emerged as key focal interests in the field of photo-ferroelectrics since the discovery of the anomalous photovoltaic effect (APV) in bismuth ferrite thin film[37,105]. It was first proposed that domain walls were the origin of above band gap open-circuit voltage (V_{OC}) owing to the efficient separation of electrons and holes by the internal electric field within domain

walls[37,105]. However, a subsequent experiment revealed that the actual mechanism behind APV effect is the bulk photovoltaic effect (BPV) resulting from its non-centrosymmetric lattice structure[119]. In contrast to the known photovoltaic effect in semiconductors with *p-n* junctions, the photovoltaic (PV) current in the BPV effect arises from the asymmetric momentum distribution of the non-equilibrium carriers in the bulk and the V_{OC} is inversely proportional to the conductivity under illumination[120]. BPV effect in ferroelectric materials leads to an anomalously large V_{OC}, i.e. well beyond the value of the forbidden bandgap, which itself can affect the indices of the refraction (photorefractive effect)[121] and other physical properties[122]. However, domain walls would instead supress the value of V_{OC} owing to the enhanced conductivity[119]. Nevertheless, the performance of a ferroelectric solar cell is not only determined by the value of V_{OC} but also the magnitude of the PV current. The question whether domain walls would facilitate or hinder the conduction of the BPV current, however, still remains unresolved, despite its importance for the photovoltaic performance based on ferroelectric materials.

In fact, it is still a challenge to distinguish the photo-response of domain walls in a ferroelectric device by the macroscopic studies due to their coexistence with the domain matrix. In order to address this problem, it is crucial to characterize the local photo-response of ferroelectric materials with nanoscale resolution, providing thus insight into electronic properties of each entity, i.e., domain and domain wall, in a ferroelectric PV device.

Here, we present a systematical study of the local photovoltaic properties of BFO thin films with nanoscale resolution, which reveals an enhancement of the PV current at domain walls. The studied BFO films consist of pure 71° domain walls and exhibit a substantial BPV effect, i.e., above bandgap V_{OC} and light-polarisation dependent PV current, at both macroscopic and nanoscale levels. Domain wall-enhanced local PV current is observed in two different sample geometries, i.e., DWs parallel and perpendicular to the grounded electrodes. Furthermore, using the ability to tune the BPV effect by varying the light polarisation angle, the spatially resolved photoconductive current is mapped, revealing a higher density of photo-excited carriers at domain walls compared to that of the domains. The resultant enhancement of the conduction at domain walls effectively facilitates the transport and collection of PV current originated from the BPV effect.

6.2 Experimental Details

Epitaxial BFO films were fabricated by pulsed laser deposition (PLD) on $(110)_o$–oriented $TbScO_3$ (TSO) substrates with growth parameters shown in Table 3-1. In order to get pure 71° domain walls, $TbScO_3$ substrates were annealed at 1000 ℃ with O_2 flow of ~200 sccm for 2 hours before film deposition[37]. The anomalous photovoltaic effect was first characterized by in-plane platinum electrodes with a defined gap of about 80 μm and a length of about 300 μm. The BFO surface was illuminated by a 405 nm laser (Newport LQA405-85E) with an intensity of 55 W/cm^2. The incident laser polarisation was tuned by rotating a half wavelength plate (Thorlabs). Local electronic properties were characterized and mapped using a home-made PhAFM system as depicted in Fig. 3-7. Here, the distance between the tip contact and grounded Pt electrode is about 40 μm. PFM was performed with ac voltage of 2.5 V amplitude and 19.27 kHz frequency applied to the AFM tip (HQ: NSC14/Pt, MikroMasch).

6.3 Results and Discussion

6.3.1 Structure Characterization

The crystallographic structure of the BFO/TSO film was first systematically characterized by the XRD method and reciprocal space mapping. As shown in Fig. 6-1, the XRD 2θ-ω scan of the BFO film grown on $TbScO_3$ (110) substrate (TSO) only shows

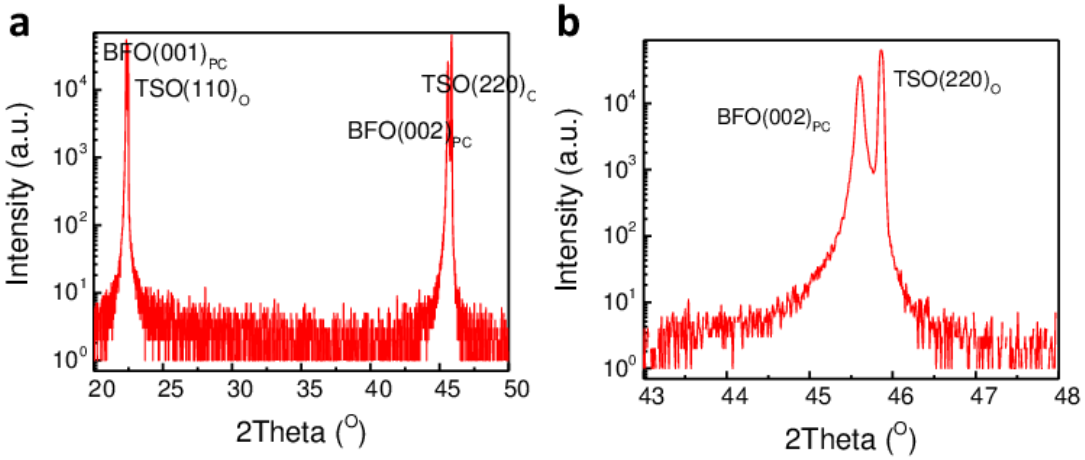

Figure 6-1. XRD data. (a) X-ray 2θ-ω scan of pseudocubic (002) face of $BiFeO_3/TbScO_3$ film. (b) Zoom in image around BFO $(002)_{pc}$ peak.

strong (*00l*) (*l*=1,2) peaks, demonstrating the phase purity of the BFO film. Due to the small lattice mismatch between BFO and TSO, the diffraction peaks of BFO and TSO almost coincide with each other. The reciprocal space maps (RSM) near $(002)_{pc}$ plane at both orthogonal in-plane sample orientation, i.e., $\varphi=0^{O}$ and $\varphi=90^{O}$, show one peak of BFO film without peak splitting, confirming the non-tilted nature of the lattice arrangement of BFO film on TSO substrate (see Fig. 6-2a, b). Splitting of the BFO $\{113\}_{pc}$ peaks shown in Fig. 6-2c and 6-2d indicates that only two ferroelastic variants, namely r_1 and r_4, exist

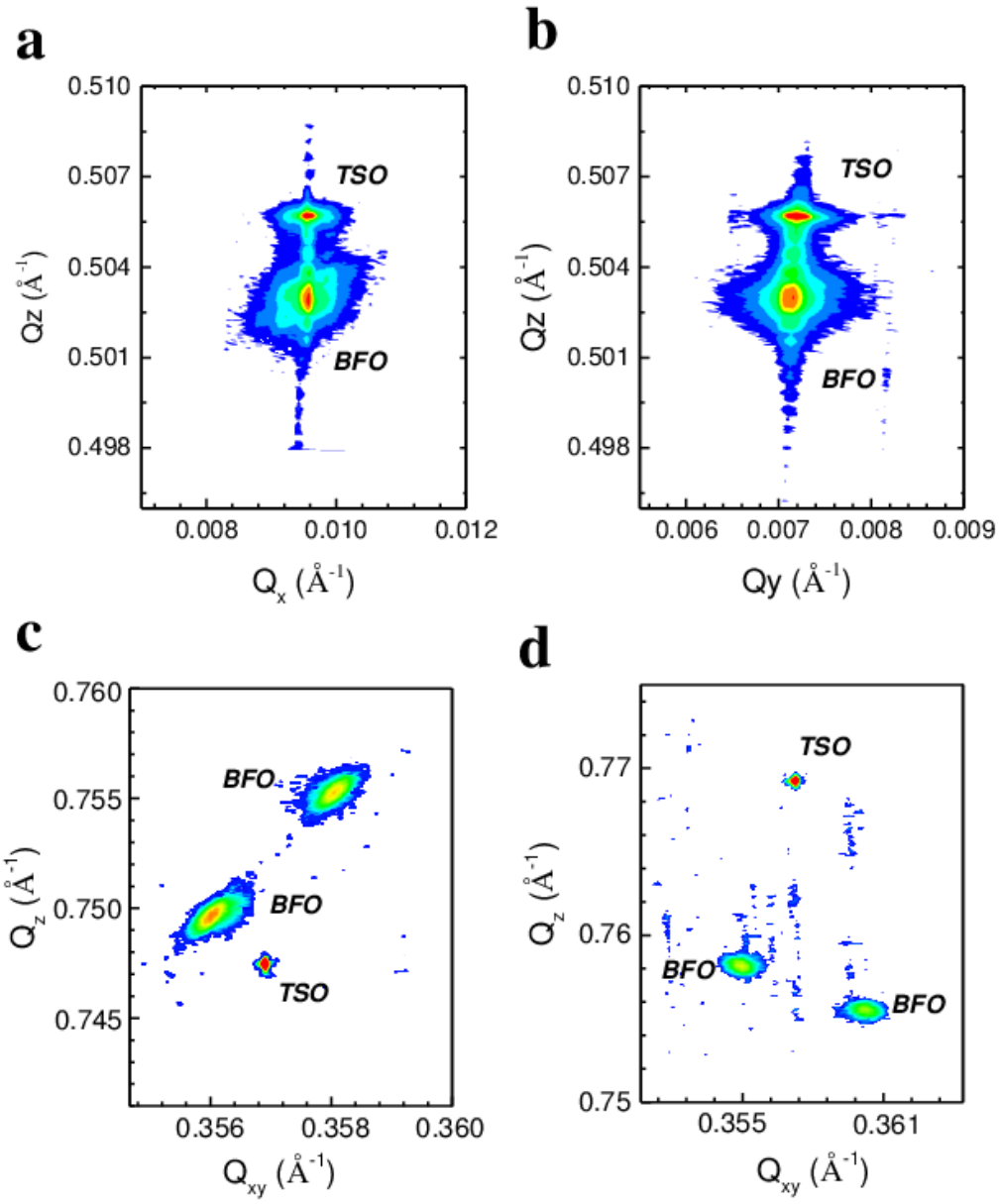

Figure 6-2. Reciprocal space maps (a) and (b) are the pseudocubic {002} face at φ of 0° and 90°, respectively. (c) and (d) are the reciprocal space maps of pseudocubic {113} measured at φ of 45° and 135°, respectively.

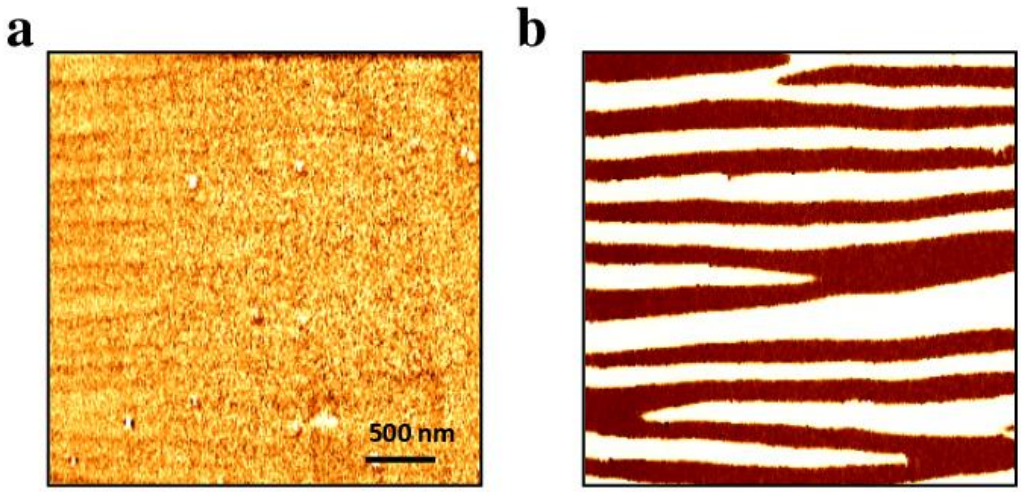

Figure 6-3. Domain structure characterization. (a) Out-of-plane PFM phase signal indicating a uniform out-of-plane polarisation direction and (b) in-plane PFM phase signal showing ±90° phase change for alternative polarisation directions in each domain.

in BFO film (refer to Fig. 2-7). The domain structure of the Fig. 6-3a and 3b represent the out-of-plane and in-plane PFM phase images, respectively, indicating the well-defined 71° stripe domains with an averaged width of about 160 nm.

6.3.2 Macroscopic Characterization of Photovoltaic Effect.

In order to confirm that the films under investigation show a typical behaviour, we first characterized the macroscopic photovoltaic properties of the BFO film by employing in-plane electrodes in two different geometries: electrodes parallel and perpendicular to the DWs, respectively (Fig. 6-4a, b). As illustrated in Fig. 6-4c, the BFO film exhibits a substantial APV effect in both geometries with above bandgap (E_g ~2.7 eV) open circuit voltage (V_{OC}) and large short-circuit current (I_{SC}). Specifically, V_{OC} and I_{SC} reach −33 V and 330 pA in the parallel geometry, and -7 V and 100 pA in the perpendicular geometry, respectively. To get further insight into the APV effect of the BFO film, the PV current was measured by varying the laser polarisation angle with respect to the crystallographic structure of the BFO film while keeping the illumination intensity constant. The variation of I_{SC} along as a function of laser polarisation azimuth in the two different electrode geometries is shown in Fig. 6-4d. In the parallel geometry, the I_{SC} reaches a maximum when the laser polarisation is perpendicular to the DWs while it decreases to almost zero when the light polarisation is parallel to the DWs. Additionally, the sign of the I_{SC}, viz. the current direction, can be tailored along with its magnitude by the incident light

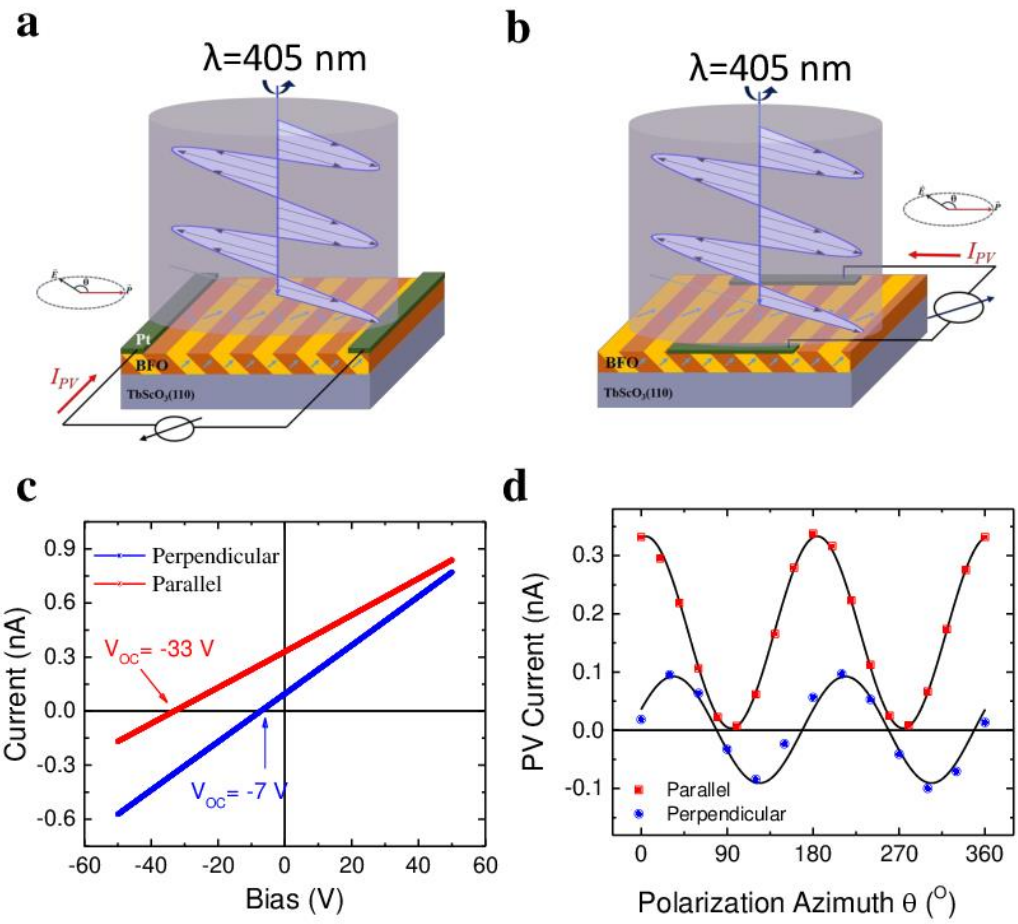

Figure 6-4. Macroscopic photovoltaic characterization of the $BiFeO_3$ thin film. (a-b) In-plane electrode geometry and illumination geometry for macroscopic measurements. Electrodes aligned (a) parallel to and (b) perpendicular to 71° domain walls. (c) Macroscopic *I-V* characteristics under illumination from a 405 nm laser with in-plane electrodes aligned parallel to (red line) and perpendicular to (blue line) the 71° domain walls. (d) Variation of photovoltaic current as function of the angle between light polarisation and the in-plane net ferroelectric polarisation with in-plane electrodes running parallel (red square dots) and perpendicular (blue circle dots) to domain walls. The continuous black lines are the fitting with Eq. 6-2 and 6-3 for parallel and perpendicular geometry, respectively.

polarisation in the perpendicular geometry. This peculiar light polarisation dependent PV current clearly differentiates the APV effect of BFO film from the conventional photovoltaic effect as in the classic p-n junction. In a conventional PV effect in which separation of the non-equilibrium photo-generated carriers is based on a gradient of the chemical potential, the PV current does not depend on light polarisation. This dependence is a strong indication that the mechanism of the APV effect is the BPV effect. The PV current density J_i in this case can be expressed in the form given by[120]

$$J_i = I_{light}\boldsymbol{\beta}_{ijk}\boldsymbol{e}_j\boldsymbol{e}_k \quad (6\text{-}1)$$

Concerning the 71° domain configuration of the studied BFO film, the response of the BPV effect in parallel and perpendicular geometries can be expressed by the following equations respectively[119]:

$$J_{parallel} = \frac{1}{3\sqrt{3}} I_{light}\left(\beta_{33} + 2\beta_{31} - \frac{\sqrt{2}}{2}\beta_{22} + \beta_{15}\right) + \frac{1}{\sqrt{6}} I_{light}\left(\beta_{22} - \sqrt{2}\beta_{15}\right)\cos\left(2\theta + \phi_x\right) \quad (6\text{-}2)$$

$$J_{perpendicular} = \frac{2}{3\sqrt{3}} I_{light}\left(\beta_{15} + \sqrt{2}\beta_{22} - \beta_{31} + \beta_{33}\right)\sin\left(2\theta + \phi_y\right) \quad (6\text{-}3)$$

where $J_{parallel}$ and $J_{perpendicular}$ are the current density in parallel and perpendicular geometry, respectively; β_{ij} the BPV tensor elements expressed in the matrix notation (see Table 6-1); ϕ_x and ϕ_y the phase shift to compensate experimental errors, for instance, misalignment between the in-plane net ferroelectric polarisation and light polarisation when θ=0°. The above equations fit very well the experimental data (see Fig. 6-4d), confirming that the mechanism of APV effect in BFO film is the BPV effect. Using the reported value of β_{22} [123], the values of rest three independent BPV tensor elements can be calculated as shown in Table 6-2.

Table 6-1. Conversion law between tensor notation and matrix notation [1]

Tensor notation	11	22	33	23, 32	31, 13	12, 21
Matrix notation	1	2	3	4	5	6

Table 6-2. Values of the BPV tensor elements of BFO film

BPV tensor elements	Value (V^{-1})
β_{15}	-6.5×10^{-5}
β_{31}	1.81×10^{-4}
β_{33}	2.11×10^{-4}
β_{22} [106]	1.10×10^{-4}

6.3.3 Nanoscale Characterization of Local Photovoltaic Effect

Our main goal is to explore the local photoelectric properties with nanoscale resolution in order to understand the role of the domain walls in the BPV effect, especially the transport of BPV current. For this purpose, we have used a home-built photoelectric atomic force microscopy (PhAFM).

As schematically shown in Fig. 6-5a, a platinum stripe electrode was deposited on the BFO surface to close the current circuit with the AFM tip. Note here that the Pt electrode is set parallel to the 71° domain walls and grounded. A linearly polarized blue laser with a wavelength of 405 nm (hv=3.06 eV) was used to illuminate the area between the Pt electrode and the tip-surface contact. Given the nanoscale tip-sample contact diameter

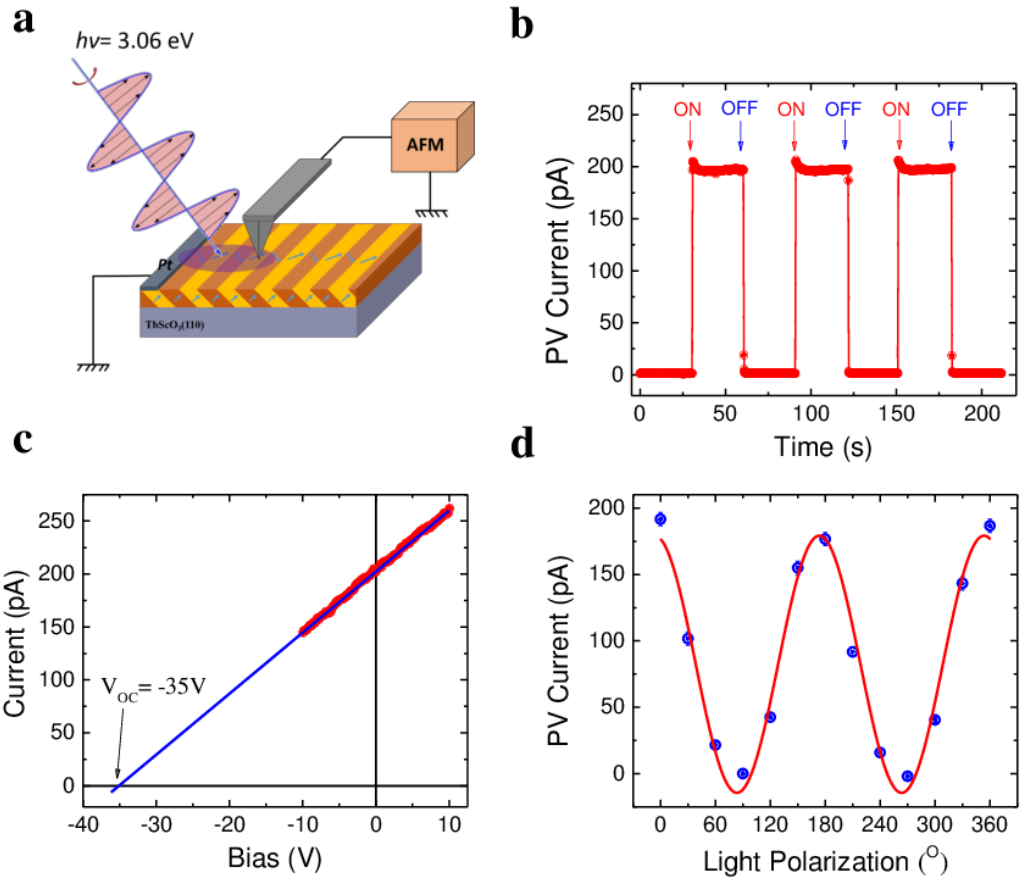

Figure 6-5. Local photovoltaic characterization. (a) Schematic showing the local measurement conducted by the PhAFM system under illumination. (b) Photovoltaic current probed by PhAFM tip. (c) Local *I-V* characteristics measured through the PhAFM tip. The linear exploration gives -35V as the open circuit voltage. (d) Photovoltaic current collected by PhAFM tip as a function of light polarisation. The continuous red line is the fit with Eq. 6-2.

(r_{tip}~30 nm), measurement of the current by PhAFM tip could provide an insight into local photoelectric properties with the same resolution as the contact diameter. Fig. 6-5b shows the time evolution of the local PV current (I_{PV}) when switching on/off the laser. A sizable current is recorded by the conductive AFM tip without applying external voltage. The magnitude of I_{PV} could be easily tailored by tuning illumination intensity, as shown in Fig. 6-6. Although the tip-surface contact area is about five orders of magnitude smaller than that of the in-plane electrodes, the local I_{PV} can reach the same order of magnitude as compared to the I_{SC} (330 pA) measured with in-plane electrodes (Fig. 6-4c) under the same illumination conditions. Meanwhile, the local V_{OC} can reach as large as -35 V determined by the extrapolation of the *I-V* characteristic in Fig 6-5c (blue curve), which is one order of magnitude higher than the bandgap of BFO. Alike that in BFO single crystals, the tip-enhanced photovoltaic effect has also been demonstrated in the BFO thin films[46].

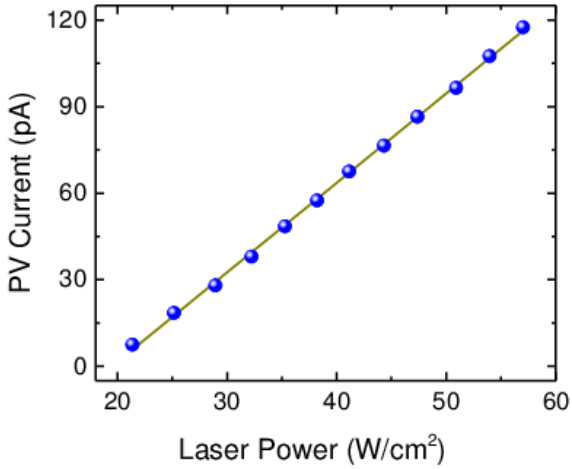

Figure 6-6. Photovoltaic current collected by a Pt-coated AFM tip in contact with BFO film as a function of illumination intensity. The yellow line is a linear fit of the experimental data shown as blue dots.

The first issue to resolve is the origin of the PV current collected by the tip, i.e. whether it is generated by a potential Schottky contact existing at the tip-BFO interface or by the BPV effect, as in the bulk case. For this we measured the PV current collected by the tip as function of the incident light polarisation. A two-fold azimuthal dependence of I_{PV} as a function of the light polarisation (Fig. 6-5d) reveals a similar behaviour as in the case of the macroscopic PV current (Fig. 6-4d), confirming that the driving force behind the tip-enhanced photovoltaic effect is also the BPV effect.

6.3.4 Spatially-resolved Photovoltaic Current Mapping

Further on we proceed in acquiring the spatially resolved PV current distribution by scanning the conductive tip on the illuminated BFO surface and simultaneously recording the I_{PV}. With the help of a switching system, the AFM can be operated sequentially in

PhAFM mode and PFM mode, enabling precise correlation between the domain and PV current patterns in the same area. Fig. 6-7a shows such correlation between I_{PV} and ferroelectric domains in a 3×3 μm^2 area. We specifically used a low laser intensity to set the average I_{PV} to a relatively low value, leading to a high resolution of spatial current distribution. The PV current map shows some intriguing features. Firstly, the PV current is detected over the whole scanned surface containing both domains and DWs, with an averaged value of 25 pA under this specific mapping condition. Secondly, and more importantly, the PV current was significantly enhanced at particular positions as highlighted by the bright lines in Fig. 6-7a. By comparing to the domain patterns revealed by both PFM in-plane phase signal (Fig. 6-7b) and in-plane amplitude signal (Fig. 6-7c),

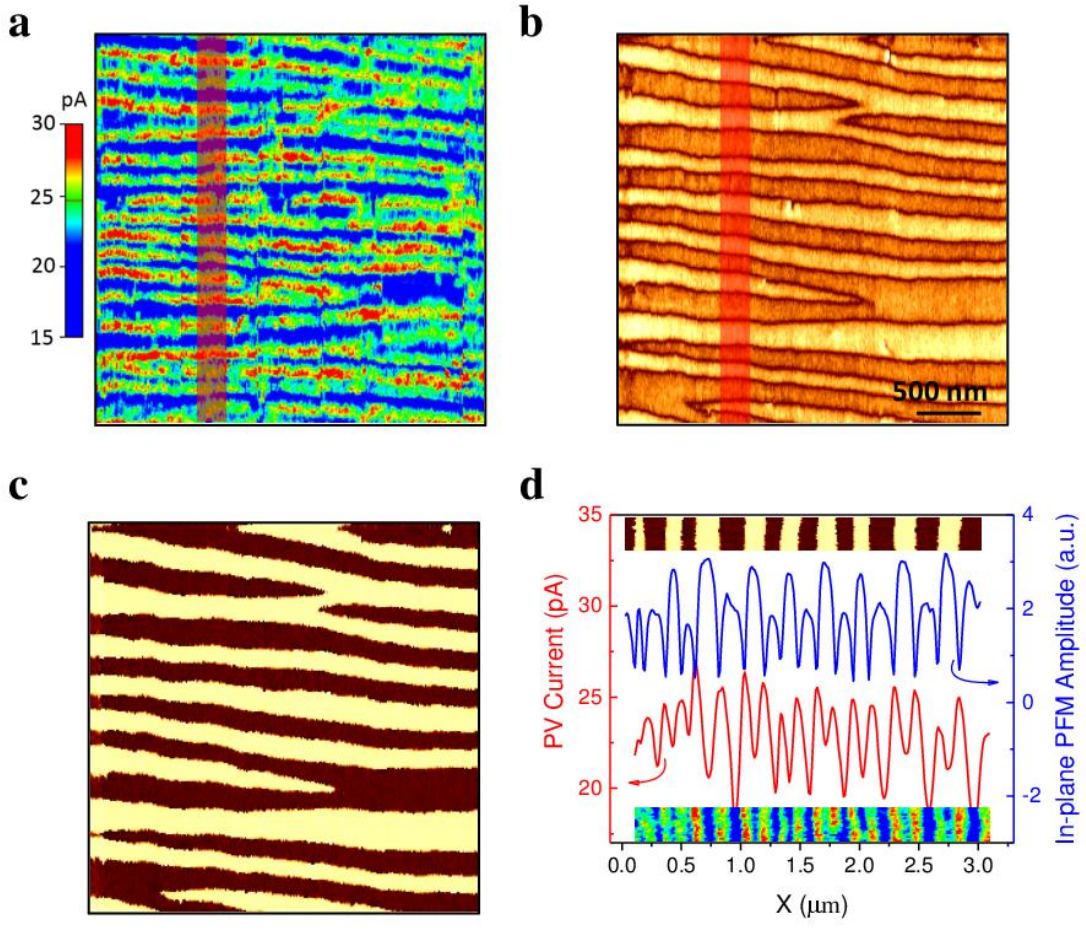

Figure 6-7. Spatially resolved photovoltaic current mapping with domain walls parallel to grounded electrode. (a) Spatial distribution of the photovoltaic current detected by PhAFM. (b) and (c) are the in-plane PFM amplitude and phase signal, respectively. (d) Profile analysis of photovoltaic current distribution and in-plane PFM amplitude signal averaged over the area marked by red in (a) and (b), upper insert and lower insert show the corresponding PFM phase images and the current distribution of

the lines exhibiting a higher PV current in Fig. 6-6a correspond to the locations where PFM amplitude signal is almost zero, respectively at the DWs. This correlation could be further validated by analysing the profiles of spatially distributed PV current and the in-plane PFM amplitude of the same region marked by red in Fig. 6-7a and 7b. As illustrated in Fig. 6-7d, each peak in the PFM in-plane amplitude corresponds to a minimum of the PV current while every minimum of the PFM in-plane amplitude, which is associated with the domain walls, points to a maximum of the PV current. This clearly shows a significant enhancement of the local PV current at DWs compared to the bulk of the domain.

The same analysis can be performed wih the grounded Pt counter electrode running perpendicular to the domain walls as illustrated in the insert of Fig. 6-8a. Fig. 6-8a shows typical *I-V* characteristics measured in this perpendicular geometry, indicating a sizable PV current (46 pA) and above bandgap V_{OC} (~10 V), similar to the macroscopic case with in-plane perpendicular geometry (Fig. 6-4c). Following the same procedure, we map the I_{PV} distribution in this second case when the domain walls are running perpendicular to the Pt electrode. Likewise, the PV current is probed all over the scanned area with a significant enhancement at the DWs (see Fig. 6-8b, c).

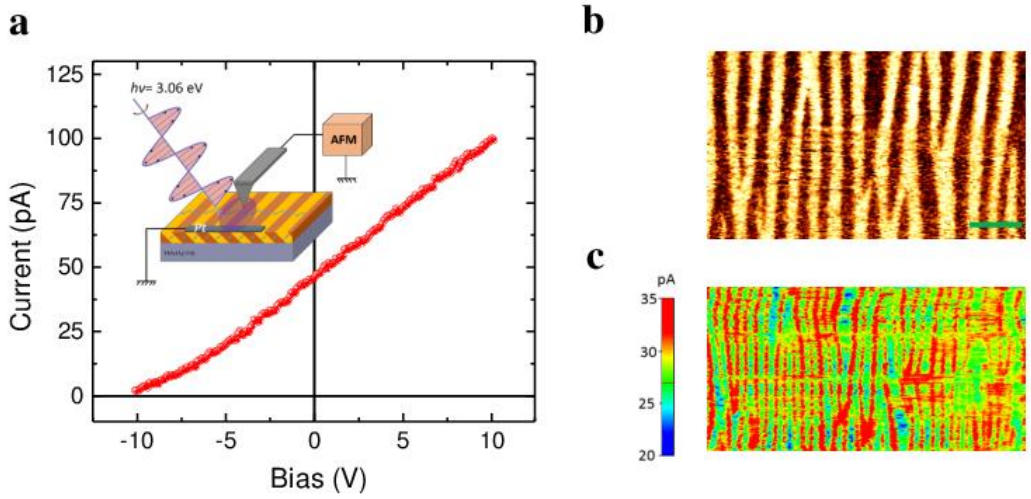

Figure 6-8. Spatially resolved photovoltaic current mapping with domain walls perpendicular to grounded electrode. (a) Local *I-V* curve acquired by PhAFM The insert shows the measurement geometry schematically. (b) and (c) In-plane PFM phase signal and spatially-resolved photovoltaic current distribution of the same area, respectively. The length of the scale bar is 500 nm.

6.3.5 Nanoscale Characterization of Photoconductive Current

To understand our experimental results, we analyse the origins of the current measured through the tip. As it has been shown above that the main origin is the BPV effect, we may now consider the most general case of a uniformly illuminated ferroelectric film under an electric field. The current in a certain crystallographic direction J_i consists of three contributions, namely bulk photovoltaic effect, drift and diffusion as expressed below:[124]

$$J_i = J_{BPV} + J_{drift} + J_{diff} = I_{light}\boldsymbol{\beta}_{ijk}\boldsymbol{e}_j\boldsymbol{e}_k + en\bar{\mu}E_i - eD\nabla n \qquad (6\text{-}4)$$

where e is the electron charge, n the carrier density, $\bar{\mu}$ the effective mobility, E_i the electric field component along the specified direction and D the diffusion coefficient. The simple diffusion currents as well as the Dember effect resulting from non-uniform illumination are neglected here due to uniform illumination in the area of interest.

Keeping in perspective the light polarisation dependence of the BPV effect (see Fig. 6-5d), one can recognize the possibility to decrease the bulk photovoltaic current J_{BPV} by tuning the light polarisation and map in such way only the distribution of the drift current, i.e. photoconductive current. The latter according to Eq. (6-4) depends solely on local carrier density n and effective mobility $\bar{\mu}$. To verify this hypothesis, the *I-V* characteristics at different light polarisations are measured and shown in Fig. 6-9. It is clear that *I-V* curves shift downwards along the ordinate with increasing laser polarisation angle from 0° to 90° and the PV current is largely suppressed when the laser polarisation is parallel to the stripe domain walls ($\theta = 90°$), which is consistent with the light polarisation dependence of PV current (see Fig. 6-4d).

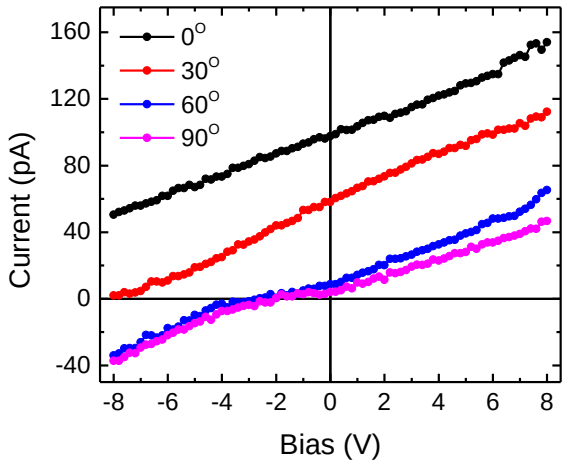

Figure 6-9. *I-V* characteristics under different incident light polarization angles

By applying 5 V to the conductive tip and setting the incident laser polarisation azimuth as 90°, only the photoconductive current is acquired through the AFM tip (see

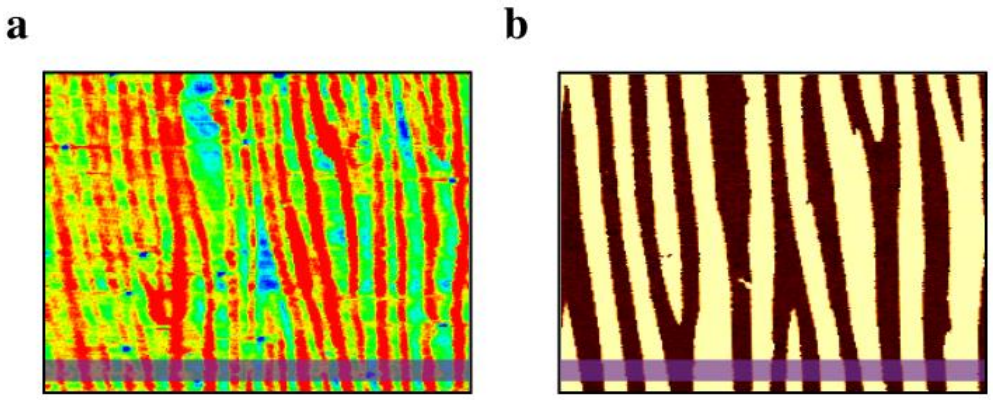

Figure 6-10. (a) Spatially resolved distribution of photoconductive current under an external bias of 5V and (b) the PFM in-plane phase signal of the same area. Here the grounded Pt electrode is parallel to the domain walls.

Fig. 6-10a). The domain configuration of the same area is characterized by the in-plane PFM phase signal as shown in Fig. 6-10b. While certain photoconductive current is detected over the whole scanned area, a significant enhancement is observed at the DWs, as demonstrated by the profile analysis in Fig. 6-11. This enhancement of the photoconductive current collected by the moving tip exactly at the domain walls is a consequence of a higher photoconductivity within the domain wall, which is consistent with in-plane macroscopic measurements showing enhanced photoconductivity when domain walls are aligned perpendicular to electrodes[119]. Although being a local property, this abnormal photovoltaic effect and enhanced photoconductivity of the domain walls is detectable only if the illumination is global. As shown in the Fig. 6-12, illuminating only the area under the AFM tip fails to generate significant photovoltaic current. The whole area between the grounded electrode and the AFM tip needs to be illuminated in order to observe the effects.

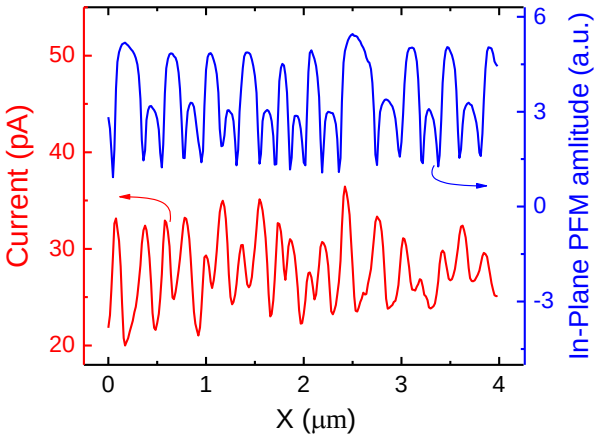

Figure 6-11. Profile analysis of in-plane PFM amplitude and the current distribution of the same region marked by red in Fig. 6-10.

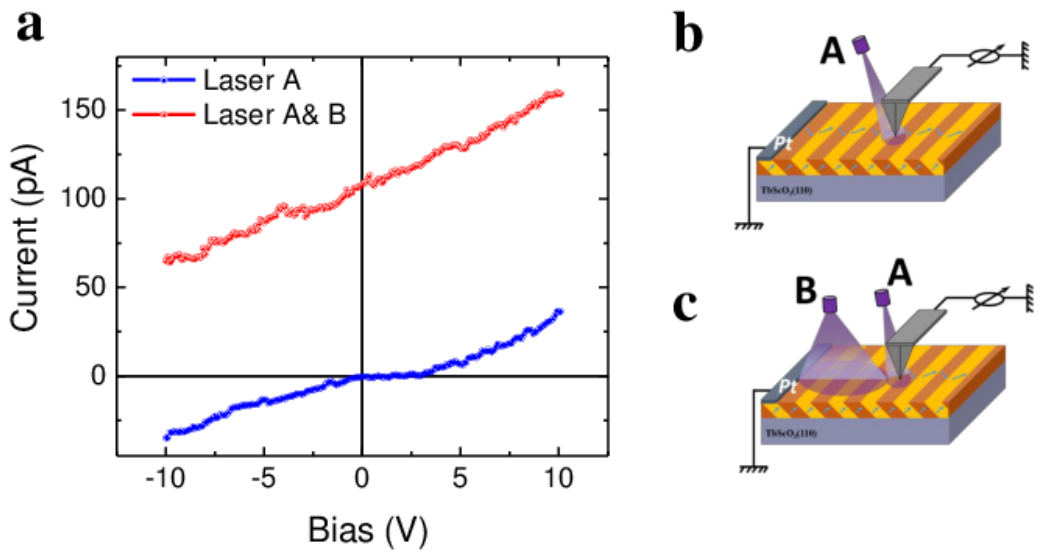

Figure 6-12. Two laser experiment. (a) *I-V* curves obtained in two laser experiment. Blue *I-V* curve is obtained with only Laser A illuminating the tip-contact region as schematically shown in (b) while red *I-V* curve is the one measured with illimination from both A and B as depicted in (c).

6.3.6 Discussion

In a simple scenario the domain walls showing a higher photoconductivity will play the role of a high conducting path for the photo-generated non-equilibrium carriers. If the illumination is local, only the local photoconductive properties are measured with external applied bias whereas illumination of the whole area between the collecting tip and counter electrode will add the photovoltaic current, which is a bulk property. We conclude from here that the local photovoltaic effect at the DWs is missing or negligible compared to the bulk PV effect. A higher photoconductivity is generally due to a higher carrier density n and/or effective mobility $\overline{\mu}$. An enhanced carrier density of DWs is related to a different electronic structure within DWs, i.e. either higher defect density or Fermi level position or a combination which would result in a different transport process at DWs compared to the bulk[111,112,125-127].

A higher carrier density at the domain walls would actually have a twofold effect on the local photocurrent enhancement. The first one is very obvious as explained above by enhancing the internal conductivity, and a second is to lower the effective tip-surface contact resistance. Apart from the contact region, the bulk of BFO film underneath the contact also plays an important role in the transport process, especially considering the extremely high current density (~10 A/cm^2) flowing through the tip-surface contact. *I-V*

characteristics acquired under illumination indicate an Ohmic-type behaviour in the low voltage range (either external applied voltage or photo-emf arising from the BPV effect). Considering this nanoscale contact (r_C ~30 nm) as an ideal point contact geometry, the dependence of current on voltage can be expressed as[128]:

$$I = 2\pi e\mu n r_C V \tag{6-5}$$

Accordingly, the transport resistance in the BFO film decrease as carrier density and/or mobility increases. Hence, domain walls, which possess higher carrier density and/or mobility, would possess higher conduction as compared to that of the domains. Consequently, in sharp contrast to the adverse effect upon V_{OC} , domain walls could effectively facilitate the transport and collection of photovoltaic current generated in the bulk of ferroelectrics.

6.4 Conclusion

The local photovoltaic effect of BFO film consisting of pure 71° domain has been explored using the PhAFM with a nanoscale resolution. PV current, shown to originate from the bulk photovoltaic effect, is detected over the entire surface and significant enhancement occurs at the domain walls. Moreover, by using the ability to tune the BPV effect by light polarisation, it is established that the enhancement of PV current at the domain walls is due to their higher photoconductivity and not a photovoltaic effect within domain walls.

Chapter 7. Light-induced Reversible Control of Ferroelectric Polarisation

Finding a unique parameter that would allow manipulation of all ferroic order parameters, i.e., (anti-)ferromagnetic, ferroelectric and ferroelastic, at room temperature is an important goal in nowadays solid state physics. Here we demonstrate full optical control, i.e. reversible switching, of the ferroelectric/ferroelastic domains in $BiFeO_3$ thin films at room temperature by the mediation of the tip-enhanced photovoltaic effect. The enhanced short-circuit photocurrent density at the tip contact area generates a local electric field well exceeding the coercive field, enabling ferroelectric polarisation switching. Interestingly, tailoring the photocurrent direction, via either tuning the illumination geometry or simply rotating the light polarisation, full control of the ferroelectric polarisation is achieved. Our finding offers a new insight into the interactions between light and ferroic orders, enabling fully optical control of all the ferroic orders at room temperature and providing guidance to the design of novel opto-ferroic devices for data storage and sensing.

7.1 Introduction

Manipulation of ferroic order parameters, i.e., (anti) ferromagnetic, ferroelectric and ferroelastic domains, by light at room temperature is a fascinating issue in modern solid state field due to cross-fertilisation of research fields, such as optics, magnetism and ferroelectricity that are largely decoupled, as well as due to its potential applications in information storage and sensors. It has been already proven that the interaction between light and magnetism allows all optical control of the magnetic domains in ferromagnetic[129], ferrimagnetic[130] and antiferromagnetic materials[131,132] via thermal and inverse Faraday effects[133]. By contrast, the optical control of the ferroelectric and/or ferroelastic orders remains in their infancy.

Light interacts with ferroelectrics in primarily two ways, i.e. thermally or electronically. Absorption of high intensity laser in ferroelectric materials, such as $LiNbO_3$ single crystals, raises the local temperature close to the Curie temperature and induces a giant local temperature gradient, giving rise to the thermal effect and resulting in local ferroelectric polarisation switching due to the thermoelectric effect and

pyroelectric effect[134,135,136]. However, this heat originated polarisation switching is irreversible and usually destructive[137].

Light can also generate non-equilibrium carriers by the usual band-band transition, leading to the electronic effect in ferroelectrics. One of the intriguing electronic effect in ferroelectric materials under illumination is the BPV effect originating from their non-centrosymmetric structures[10]. The BPV effect generates a light polarisation dependent switchable short-circuit current (I_{SC}) and an anomalously large V_{OC} well exceeding the limitation of the bandgap[10,12,36,40,46,87,103,106,138]. The theoretically unlimited V_{OC}, which is able to modify the refractive index[36], is likely to be able to trigger domain switching in ferroelectrics under illumination. However, the electric field induced by the V_{OC} is either parallel to the ferroelectric polarisation or smaller than the coercive field[44]. For instance, the largest reported value of the electric field generated by the V_{OC} in $BiFeO_3$ films, is about 5.5 kV/cm that is about two orders of magnitude smaller than its coercive field[12,139]. Overall, neither the thermal nor electronic effects reported so far induced by light interaction with ferroelectrics are able to reversibly manipulate the ferroelectric domains in a deterministic way.

Here, we exploit a largely overlooked characteristic parameter of the BPV effect, i.e., the photocurrent I_{SC}, as a tool to achieve optical control of ferroelectric domains. In the semiconductor realm, the current density is proportional to the gradient of electric potential, i.e., electric field[140]. Equally, in devices powered in constant current mode, respectively by a current source rather than a certain constant field, the local electric field is proportional to the local current density. In the case of the BPV effect, the light excitation generates non-equilibrium carriers that spontaneously move towards a preferred crystallographic direction in the absence of any applied external electric field. This makes the BPV effect behave like a current source[10]. It can be speculated that in a certain architecture wherein the photocurrent density is significantly enhanced, for example, by reducing the area of current flow, a local electric field that could be higher than the coercive field will be generated, enabling thus the polarisation switching.

Based on this hypothesis, we utilized a conductive atomic force microscopy (AFM) tip as a movable electrode to probe the light-generated photocurrent in a specially designed device based on epitaxial BFO thin films. Despites its nanoscale dimension, the conductive AFM tip can collect a similar amount of I_{SC} as the macroscopic electrodes[46,104,106]. This intriguing phenomenon, which is termed tip-enhanced

photovoltaic (PV) effect, would automatically enhance by several orders of magnitude at the nanoscale contact the photocurrent density as well as the local electric field, inducing ferroelectric polarisation switching underneath the tip.

7.2 $BiFeO_3$ Thin Film Preparation

To achieve the optical control of ferroelectric polarisation we used tip-enhanced PV effect in a specially designed thin film device configuration schematically shown in Fig. 7-1. Nominally 150 nm thick $(001)_{pc}$-oriented BFO films are deposited on (110)-oriented $TbScO_3$ (TSO) substrate buffered with patterned 10 nm SRO film where the subscript "pc" denotes pseudocubic perovskite indices. The epitaxial SRO layer is previously patterned in a square shape located in the centre of the sample, which acts as a bottom electrode offering screening charges for polarisation switching. The BFO film is deposited over the whole substrate building two main regions: with and without SRO bottom electrode.

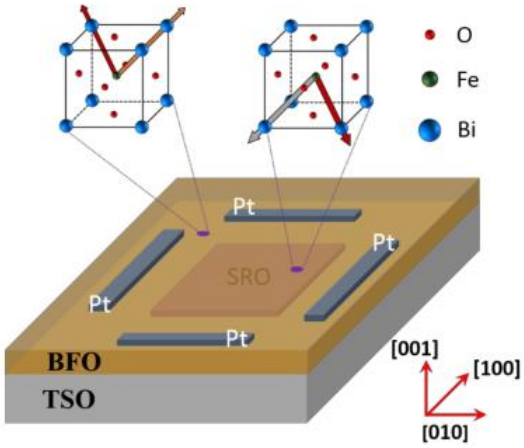

Figure 7-1. Schematic of the $BiFeO_3$ thin film explored in this chapter.

The BFO film used in this work was prepared by two-step pulsed laser deposition method, as schematically shown in Fig. 7-2a. A 100 nm thick amorphous $La_{0.7}Sr_{0.3}MnO_3$ (LSMO) film was firstly deposited on the O_2-anneal $TbScO_3$ substrate at room temperature by PLD as hard mask to grow patterned SRO thin film. The LSMO film was then patterned by the photolithography method and etched by acid consisting of 0.1 M/L H_2O_2 and 3.3 mM/L H_2SO_4 to remove the center part. Then, a 10 nm thick $SrRuO_3$ was deposited on the TSO substrate patterned by LSMO film. The growth conditions are listed in Table 3-1. The hard mask LSMO layer was then etched away by acid, leaving a square shaped SRO film in the center of the TSO substrates. Afterwards, the BFO film with a thickness of about 150 nm was grown by PLD technique on the SRO buffered TSO substrate.

Fig. 7-2b shows the surface morphology of the treated TSO substrate with clear step terraces. The height difference between adjacent steps is consistent with the lattice constant. As clearly depicted in the Fig. 7-2c, the SRO film still exhibits a step terraced surface like the TSO substrate, indicating its high quality. Both the BFO/TSO film and the BFO/SRO/TSO films possess smooth surface with sub-nanometre roughness (see Fig. 7-2d and 2e). Stripe platinum electrodes with a length of about 200 μm were evaporated on the top of the BFO/TSO surface running parallel to the respective edges of the SRO

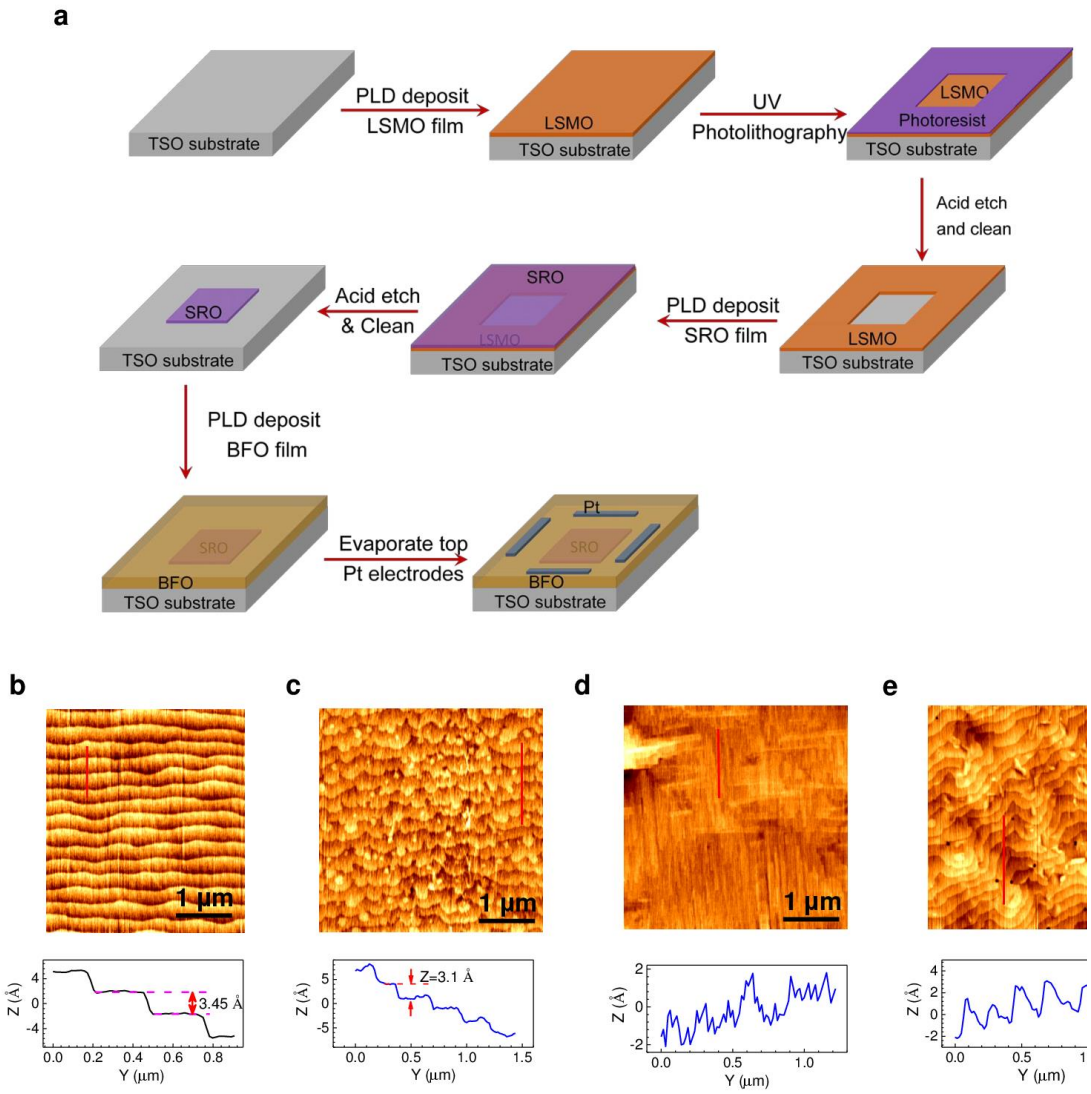

Figure 7-2. Sample preparation processes and surface morphology characterization.(a) The preparation processes of $BiFeO_3$ thin films on $SrRuO_3$ buffered $TbScO_3$ substrate. The surface topography of (b) the O_2 annealed $TbScO_3$ substrate, (c) as grown $SrRuO_3$ layer, (d) $BiFeO_3$ film grown in bare $TbScO_3$ substrate and (e) $BiFeO_3$ film on $SrRuO_3$ buffered $TbScO_3$ substrate. The figures under (b-e) are the respective line profiles of the area marked by black lines.

layer. These stripe electrodes are to complete the current circuit with the PhAFM system. The gap between the platinum electrode and the edge of the SRO layer is about 200 μm.

7.3 Results and Discussion

7.3.1 Crystallographic and Domain Structure Characterization

The BFO sample was first characterized by the XRD and RSM method to study its crystallographic structure. As shown in Fig. 7-3, the XRD 2θ-ω scan of BFO film only shows strong (*00l*) (*l*=1,2) peaks, indicating pure phase of BFO film. The reciprocal space mapping (RSM) near $\{002\}_{pc}$ faces at φ=0° shows only one peak of BFO film without peak splitting whereas that measured at φ=90° shows one main peak with two weak peaks, indicating that the arrangement of the BFO lattice on the TSO substrate is partially tilted (Fig. 7-4a and 4b). To further characterize the structural variant of the BFO film, we performed the RSM around the BFO $\{113\}_{pc}$ faces at φ=45° and φ=135°, respectively. Clearly illustrated in Fig. 7-4c and 4d, the RSM signal of BFO $\{113\}_{pc}$ faces splits into two main peaks and two weak peaks. This indicates that there exist two dominant ferroelastic variants and another two variants with minor volume in the BFO film. Combined with the PFM characterization (see below), the major variants corresponds to the $\vec{P}_1^+ / \vec{P}_1^-$ and $\vec{P}_2^+ / \vec{P}_2^-$ while the minor variants are $\vec{P}_3^-$ and $\vec{P}_4^-$ (see Fig. 2-12).

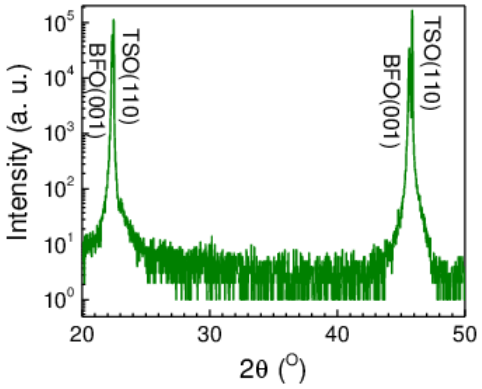

Figure 7-3. XRD 2θ-ω scan of pseudocubic (002) face of $BiFeO_3$ thin films

The domain structures of the The BFO film grown directly on TSO substrate, termed here BFO/TSO, consists of stripe domains separated by 71° domain walls with uniform positive out-of-plane polarisation, i.e., pointing from BFO/TSO interface to BFO surface (see Fig. 7-5a and 5b). The BFO film deposited on SRO bottom electrode (termed BFO/SRO) comprises also of mostly 71° stripe domains but with negative out-of-plane polarisation, i.e., pointing from the BFO surface to the BFO/SRO interface (Fig. 7-5c and 5d). The polarisation of the BFO/SRO heterostructures can be easily switched in a

conventionally way, i.e., with electrically biased AFM tip, as shown in Fig. 7-6a. Local spectroscopic PFM measurement revealed a rectangular-like piezoelectric hysteresis loop with local coercive voltage of about 5 V and marginal imprint (see Fig. 7-6b).

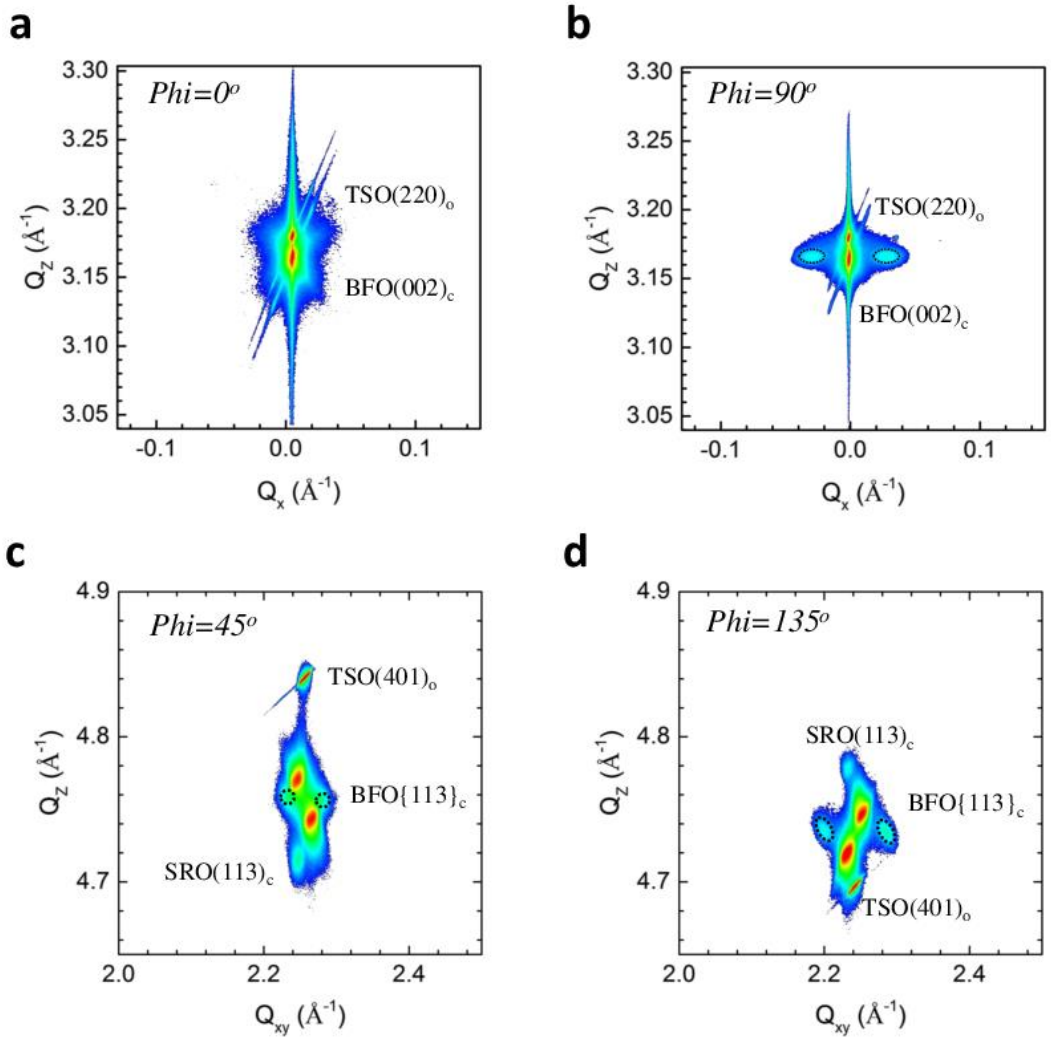

Figure 7-4. Reciprocal space maps (a) and (b) are the $BiFeO_3$ $\{002\}_{pc}$ face at φ of 0^O and 90^O, respectively. (c) and (d) are the reciprocal space maps of $BiFeO_3$ $\{113\}_{pc}$ measured at φ of 45° and 135°, respectively.

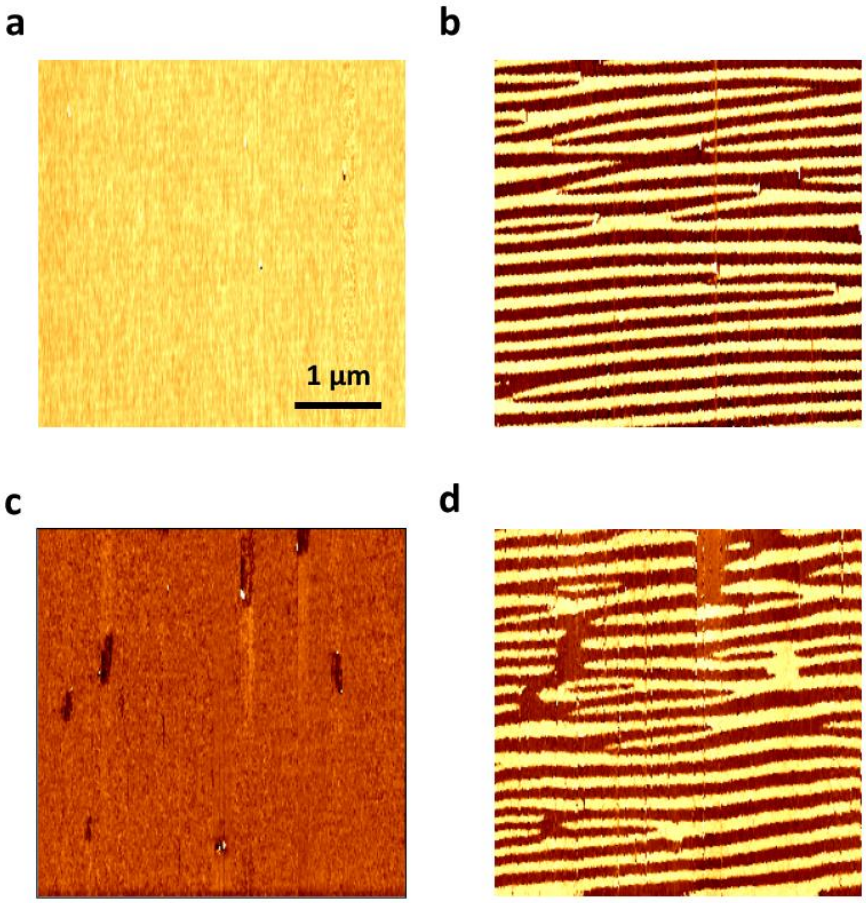

Figure 7-5. (a) The out-of-plane PFM phase signal and (b) the in-plane PFM phase signal of $BiFeO_3/TbScO_3$ film. (c) The out-of-plane and (d) in-plane PFM phase signal of the $BiFeO_3/SrRuO_3/TbScO_3$ film.

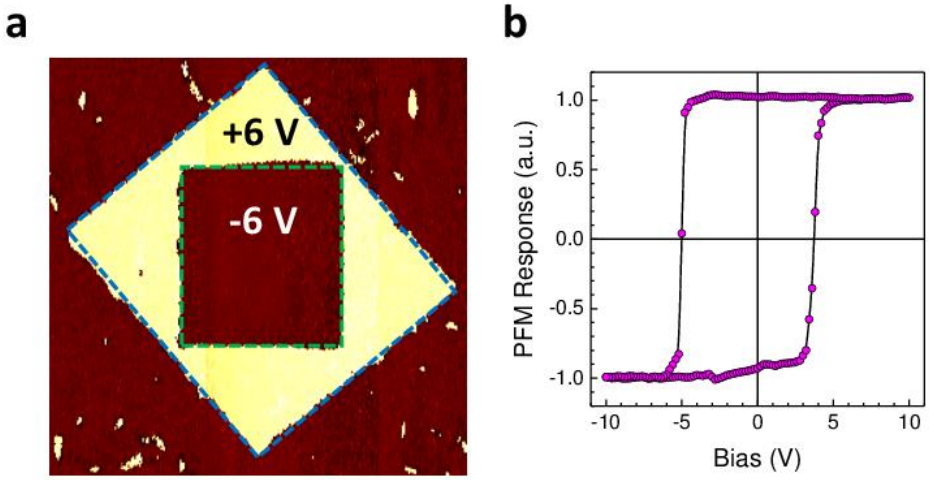

Figure 7-6. (a) Out-of-plane PFM phase signal illustrating an electrically written domain structure. (b) Local PFM spectroscopic P-V loop.

7.3.2 Tip-enhanced Photovoltaic Effect-Induced Ferroelectric Switching

Optically induced ferroelectric polarisation switching experiments are based on the principle that a high current flowing through a finite size electrode must be associated with a very high electric field localized under this electrode (tip enhancement). We have here decoupled photovoltaic generation and current collection with the above device in which the light-induced I_{SC} are generated in BFO/TSO area and further collected by the tip in the BFO/SRO area. The experiments were performed using the PhAFM system along with the stripe platinum electrodes (see Fig. 7-7).

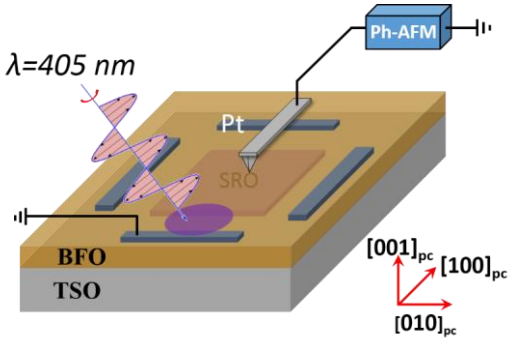

Figure 7-7. Schematic showing the device configuration and illumination area wherein the grounded platinum electrode runs along the $BiFeO_3$ $[010]_{pc}$ direction.

The current-voltage characteristic acquired by the tip contacting BFO film above the SRO layer, but illuminating the BFO/TSO space with an illumination intensity of 40 W/cm^2 reveals a positive I_{SC} with a magnitude of about 0.3 nA and an above bandgap V_{OC} of -26 V (see Fig. 7-8a). Note that the positive sign of the I_{SC} denotes the current flows from the BFO film to the tip. Due to the nanoscale size of tip radius, the short-circuit current density at the tip/surface contact area reaches about 10 A/cm^2, that is about

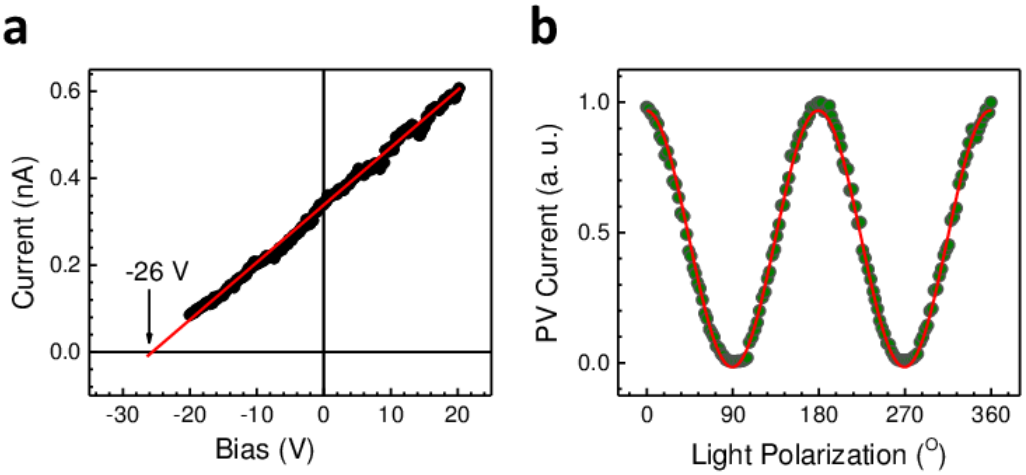

Figure 7-8. (a) The local current-voltage characteristics. (b) The light polarisation dependence of local photocurrent.

five orders of magnitude higher than that of the coplanar PV device[106]. The periodic dependence of the I_{SC} on the light polarisation, as shown in Fig. 7-8b, confirms that the tip-probed current originates from the BPV effect of the BFO/TSO film[10].

This giant short-circuit current density along with the anomalous V_{OC} obtained in the above geometry, as hypothesised, can induce local switching of the ferroelectric domains. To verify this, we use the tip as a mobile electrode to scan a 3×3 μm^2 area on the BFO/SRO surface while illuminating the BFO/TSO surface and recording the value of the I_{SC}, termed here PhAFM scan (Fig. 7-9). Note that, neither AC nor DC external voltage was applied to the system during this scanning process. The pristine domain structure around this area was first characterized by the PFM in dark (Fig. 7-10a and 10b). We subsequently investigated the resultant ferroelectric domain pattern as shown in Fig. 7-10c and 10d. The area marked by the squares corresponds to the photocurrent mapping area shown in Fig. 7-9. Strikingly, the out-of-plane polarisation of the scanned area has been switched from negative to positive and the in-plane domains have also been significantly modified.

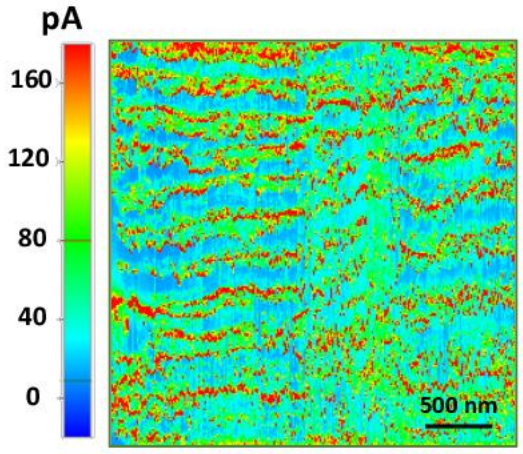

Figure 7-9. Spatially resolved photocurrent distribution acquired by PhAFM with illumination geometry shown in Fig. 7-7.

To comprehensively characterize the ferroelectric domain structures written by light, angle-resolved PFM measurements were performed after the optical writing process, as shown in Fig. 7-11. The pristine domain structures of a 20×20 μm^2 area were first characterized before the optical writing (Fig. 7-11a, b). The illumination condition and the scanning method used here for optical writing are the same as that used in Fig. 7-10. To fully characterise the resultant domain structures after optical writing, the area was measured by PFM using different tip directions with respect to the BFO crystallographic structure. First, the cantilever was placed along the BFO $[100]_{pc}$ direction while doing the PFM scanning (Fig. 7-11c, d). Then, this area was characterized again by placing the cantilever in perpendicular direction, i.e., along the $[010]_{pc}$ direction, by rotating the

sample by 90° (Fig. 7-11e, f). According to these PFM phase images, we found that the ferroelectric variants were switched by light from the pristine $\vec{P}_1^-/\vec{P}_2^-$ to the $\vec{P}_1^+/\vec{P}_2^+$, as schematically shown in the insert of Fig. 7-11c, e and Fig. 7-12 . Therefore, the ferroelectric polarisation is switched solely by light via the tip-enhanced PV effect.

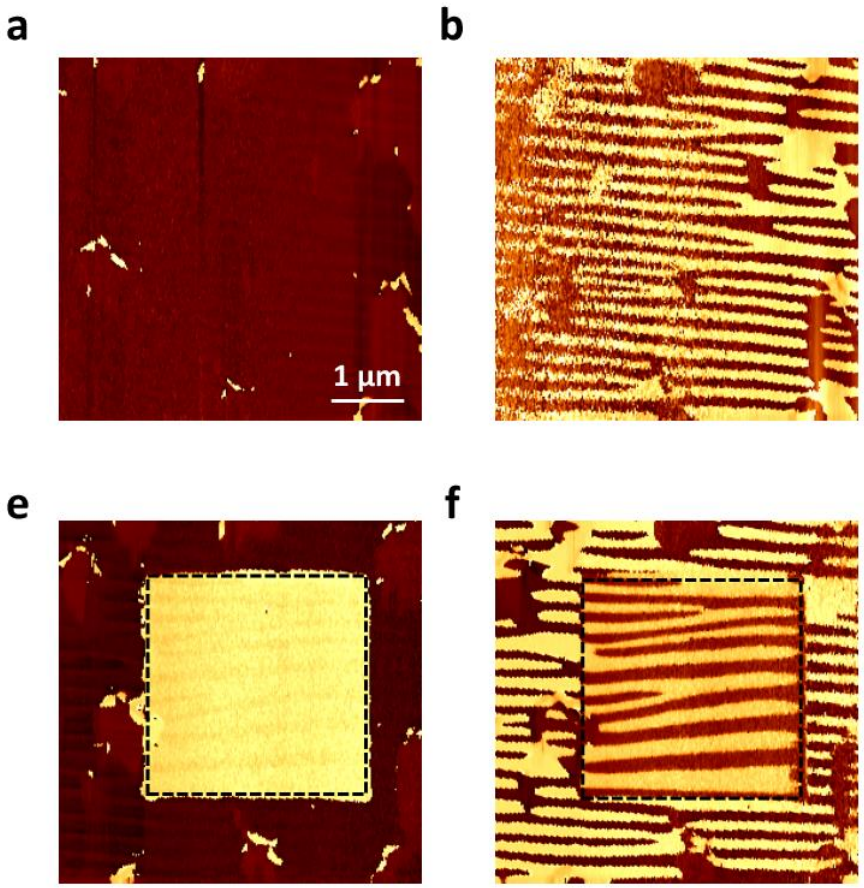

Figure 7-10. (a) Out-of-plane and (b) in-plane PFM phase signal of a pristine domain structures before PhAFM scans. (c) Optically written out-of-plane and (d) in-plane domain structures.

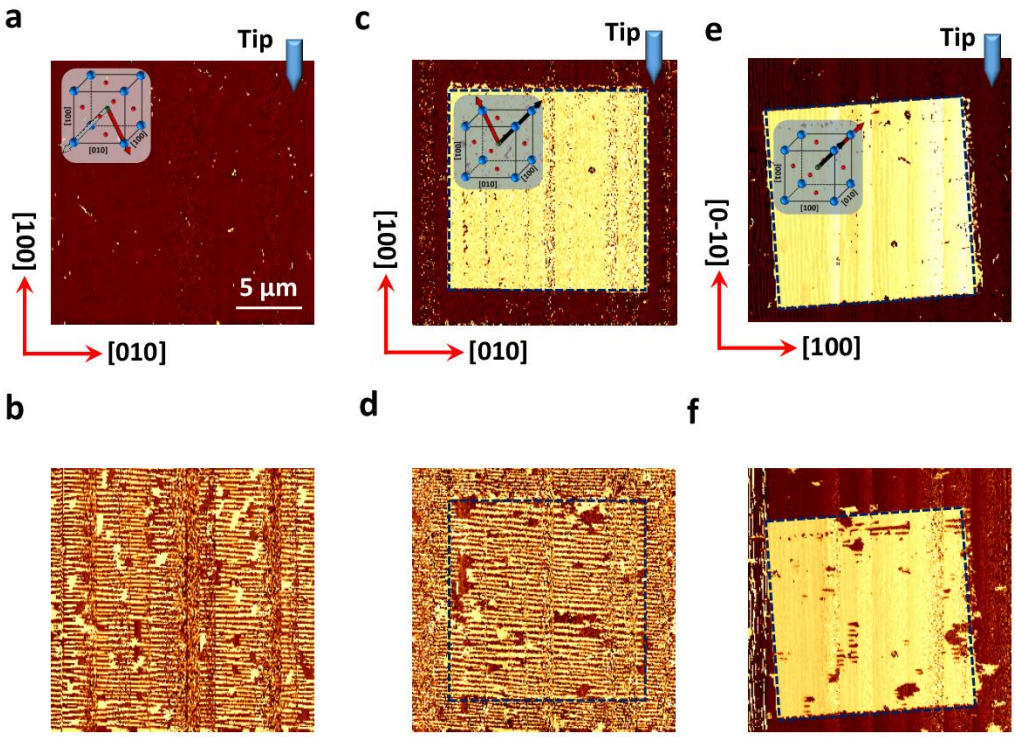

Figure 7-11. Angle-resolved PFM characterization of the optically written domains. (a) Out-of-plane and (b) in-plane PFM phase signal showing the pristine domain structures of a 20×20 μm^2 area before optical writing. The insert shows the corresponding ferroelectric variants of the $BiFeO_3$/$SrRuO_3$ film. (c-f), Angle-resolved PFM characterization of the optically written domain structures. Domain structures shown (c-d) were characterized by placing AFM cantilever along $BiFeO_3$ [100]pc direction while that shown in (e-f) was characterized with AFM cantilever pointing to $BiFeO_3$ [010]pc direction. (c) and (e) show the out-of-plane domain structures while d and f correspond to the in-plane domain structure. The insert shown in (c) and (e) shows the optically switched ferroelectric variants.

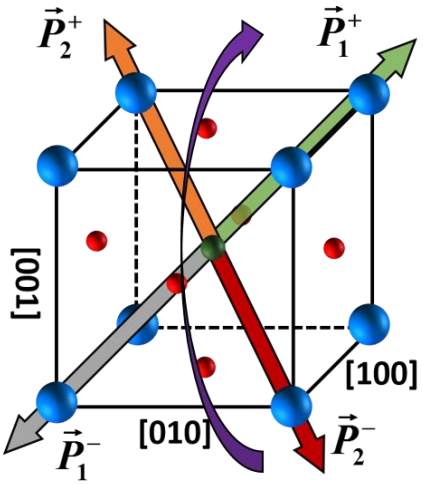

Figure 7-12. Schematic illustrates the optically induced polarisation switching between pristine ferroelectric variants $\vec{P}_1^- / \vec{P}_2^-$ to the resultant $\vec{P}_1^+ / \vec{P}_2^+$.

The critical light intensity that induces the ferroelectric switching has also been studied. The pristine domain structures of an area was first characterized by PFM in dark before the optical writing, as shown in Fig. 7-13a. Then, the optical writing process was conducted by scanning the tip on this area while illuminating the BFO/TSO surface with increased light intensities. Fig. 7-13b shows the spatially resolved I_{SC} distribution acquired under various light intensity. At low light intensity of 0.2 W/cm^2, the I_{SC} is probed only at locations where domain wall exists whereas that at the domain bulk is very small. More importantly, the intact lines in the I_{SC} distribution mapped under 0.2 W/cm^2 light intensity indicate that the domains structures probably remain unchanged during the

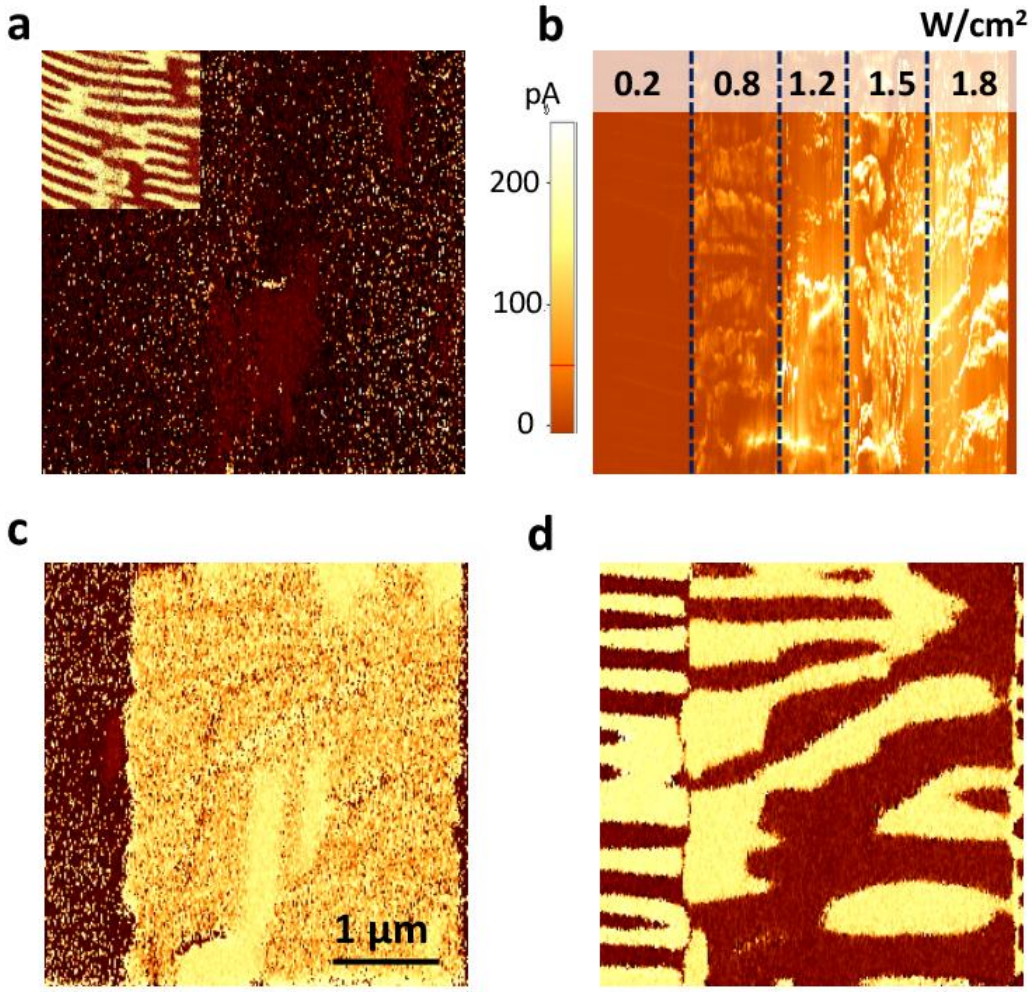

Figure 7-13. Light intensity resolved optical control of ferroelectric domains. (a) Out-of-plane PFM phase signal showing the pristine domain structures. The insert shows the corresponding in-plane domain structures. (b) Short-circuit current mapping with increased light intensity illuminating on the $BiFeO_3/TbScO_3$ surface. The number at the top of (b) indicates the light intensity used during the PhAFM scana of that area. (c) The resultant out-of-plane and (d) in-plane PFM phase signal after the PhAFM scans.

PhAFM scans. However, after increasing the light intensity over 0.8 W/cm^2, the I_{SC} mapping image becomes disordered, indicating the domain structure being largely distorted. To verify this, the domain structure of this area was characterized again by PFM in the dark after the PhAFM scans. As clearly illustrated in Fig. 7-13c, d, the domain structure remains the same as the pristine one after the PhAFM scan with the light intensity of 0.2 W/cm^2. With increased light intensity ($\geq$ 0.8 W/cm^2), the out-of-plane polarisation has been switched from negative to positive. The in-plane domain structure has also been largely modified, which is consistent with the I_{SC} mapping. The above experiment primarily indicates that low light intensity ($\geq$ 0.8 W/cm^2) is able to achieve the optical control of ferroelectric orders, which is over five order of magnitude smaller than the light intensity required for the thermally induced ferroelectric switching[135,136].

In addition to the optical control of the ferroelectric polarisations in the BFO/SRO/TSO film discussed above, light can also manipulate the in-plane ferroelectric domains in the BFO/TSO film in the absence of a conductive bottom electrode, which is similar to that achieved by coplanar electrodes[141]. Fig. 7-14a shows the local current-voltage characteristics acquired by the AFM tip on the illuminated BFO/TSO surface with light polarisation running parallel to the BFO $[100]_{pc}$ crystallographic structure. The AFM tip collects a large I_{SC} directly from the BFO/TSO surface (~170 pA) and the local V_{OC} reaches as large as -31 V. The local PV current also exhibits light polarisation dependence, confirming its origin as the BPV effect (Fig. 7-14b). As the tip collects a positive I_{SC} here, i.e., the I_{SC} flows from the BFO film into the tip, the induced local electrical field underneath the tip is parallel to the out-of-plane ferroelectric polarisation. Thus, the out-of-plane component of the ferroelectric polarisation remains intact under the PhAFM scans. Nevertheless, the movement of the conductive tip will induce a tailing electrical field pointing to the tip movement direction, which would modify the in-plane ferroelectric polarisations[29].As demonstrated in Fig. 7-14c and 14d, the in-plane domain structures have been largely modified after the PhAFM scans with an I_{SC} of about 150 pA. For instance, a wide stripe domain appears at the position indicated by the black dot where three pristine stripe domains existed before the PhAFM scans.

7.3.3 The Role of Tip Enhancement

To prove that the tip-enhancement is the key ingredient in this optical control of the ferroelectric polarisation, we preformed similar experiments in which 5nm thick Pt electrodes with a lateral size of 10×10 μm^2 were evaporate on top of the BFO/SRO area

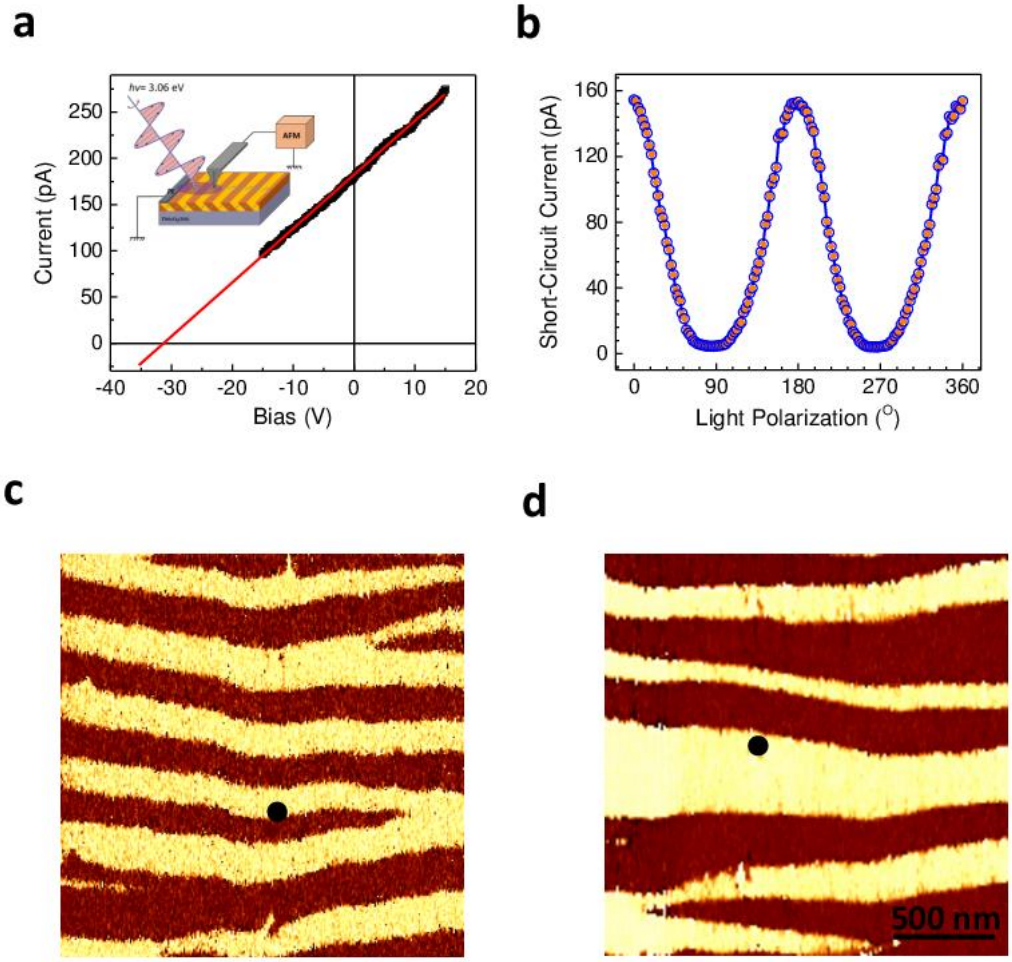

Figure 7-14. Light-induced in-plane ferroelectric polarisation switching in $BiFeO_3/TbScO_3$ films. (a) The local current-voltage curve acquired the AFM tip on illuminated $BiFeO_3/TbScO_3$ films with an light intensity of 40 W/cm^2 and light polarisation parallel to the $BiFeO_3$ [100]pc direction. The insert shows the measurement setup schematic. (b) The light polarisation dependence of the local short-circuit current. (c) Pristine in-plane domain structure of a 2×2 area before the optical writing. (d) Optically written domain structure by scanning the AFM tip on the illuminated $BiFeO_3/TbScO_3$ surface. The scanned area shown in (c) and (d) drift slightly as indicated by the black dot.

(Fig. 7-15a). Current-voltage characteristics of Pt/BFO/SRO capacitors reveals, as expected, a two orders of magnitude lower current density compared to that acquired by the tip on the bare BFO/SRO surface, despite its larger absolute value of the I_{SC} (Fig. 7-15b). On the other hand, the Pt/BFO/SRO structure exhibits a larger V_{OC} (44 V) compared to the tip/BFO/SRO structure (26 V). If V_{OC} would solely be the driving force to induce the polarisation switching, the ferroelectric polarisation of the Pt/BFO/SRO capacitors would have been more easily switched compared to the tip/BFO/SRO structure under the same illumination condition. To verify this, we performed the PhAFM scan on a 20×20

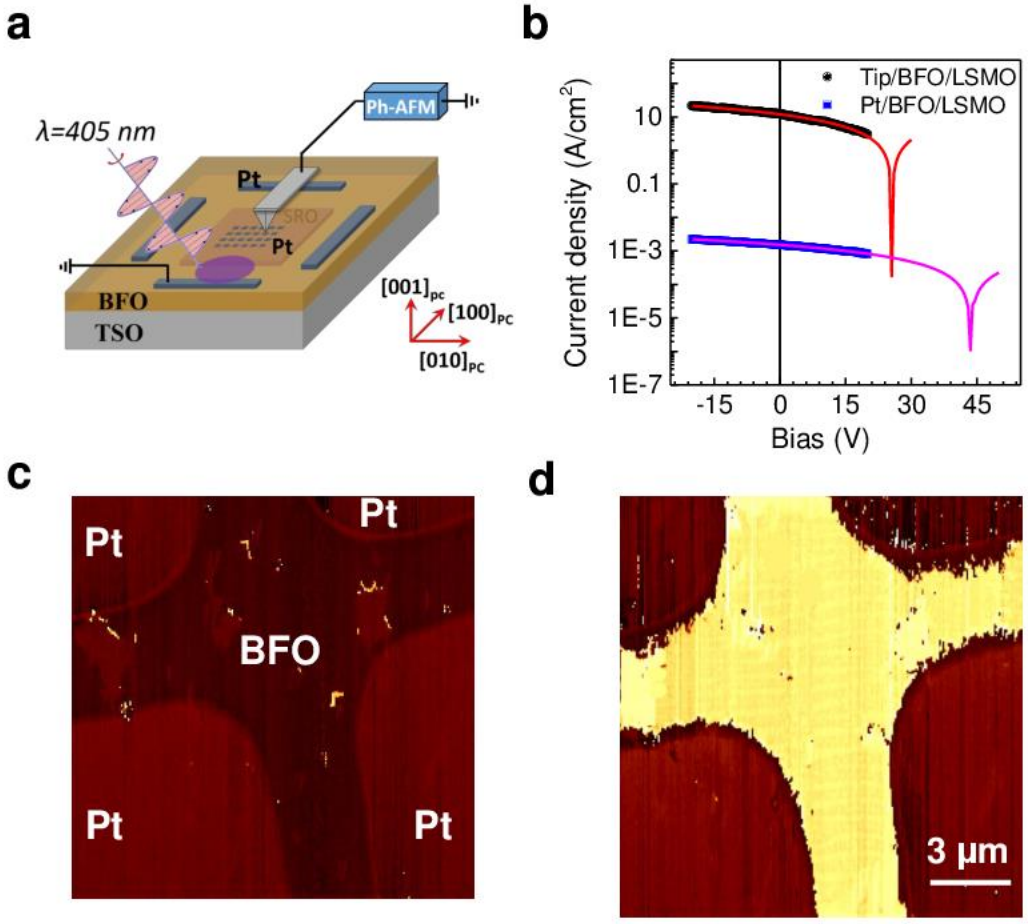

Figure 7-15. Role of short-circuit current density in the light-induced ferroelectric polarisation switching. (a) Schematic shows the PhAFM scans on the $BiFeO_3/SrRuO_3$ film covered by patterned Pt top electrodes. (b) The current density-voltage characteristics of tip/$BiFeO_3/SrRuO_3$ structure and Pt/$BiFeO_3/SrRuO_3$ capacitors. (c) Out-of-plane domain structure of a 20×20 μm^2 area covering both bare $BiFeO_3/SrRuO_3$ surface and Pt/$BiFeO_3/SrRuO_3$ structure was characterized before, and (d) after the PhAFM scans.

μm^2 area covering both bare BFO/SRO surface and Pt/BFO/SRO capacitors while illuminating the neighbouring BFO/TSO surface. Fig. 7-15c and 15d show respectively the out-of-plane domain structure of the scanned area before and after the PhAFM scan with an average I_{SC} of about 100 pA. As expected, only the polarisation of the bare BFO/SRO area is switched to positive direction, that of the Pt/BFO/SRO capacitors remaining unperturbed. Therefore we conclude that the enhanced current density is the switching driving force.

To understand the associated mechanism, we analyse the electronic transport process of I_{SC}. The I_{SC} conduction path consists of two parts: the in-plane part represented by the illuminated BFO/TSO film (from platinum stripe to SRO layer) and the out-of-plane part

from SRO bottom electrode to the AFM tip. The illuminated BFO/TSO area generates the I_{SC} originated from the BPV effect, acting as a current source. This current flows into the SRO electrode and then is injected into the conductive tip passing the BFO film. Due to the massively reduced size of the tip contact area on the BFO surface, the current density J is very high in the region near the tip/BFO interface. As elucidated by Lampert et al., the maximum electrical field associated with a current injection from a point contact, i.e., the AFM tip in this work, can be predicted as[128,142]:

$$E_{\max} = 0.4\left(\frac{I}{\pi\mu\theta\varepsilon_0\varepsilon}\right)^{1/2}\left(\frac{1}{r_{tip}}\right)^{1/2} \tag{7-1}$$

where θ is a parameter describing the trapping effect of the shallow levels in the bandgap, ε_0 is the vacuum permittivity, ε is the relative permittivity of the BFO film, and r_{tip} is the radius of the contact area. Clearly, the electrical field underneath the tip is proportional to the I_{SC} whereas inversely proportional to the contact dimension. Given a set of trapping levels lying 0.5 eV below the bottom of the conduction band, the evolution of the E_{max} generated in the BFO film as a function of photocurrent and contact radius is shown in Fig.7-16. For instance, a 300 pA current injected from the tip with a radius of 30 nm generates an E_{max} as large as 1800 kV/cm, which is one order of magnitude larger than the coercive field ($E_c \sim 200\ kV/cm$), thus enabling local ferroelectric polarisation switching. In contrast, if the contact radius r_{tip} is large, the E_{max} decreases correspondingly even at the same I_{SC}. This is happening underneath the large Pt top electrodes where the

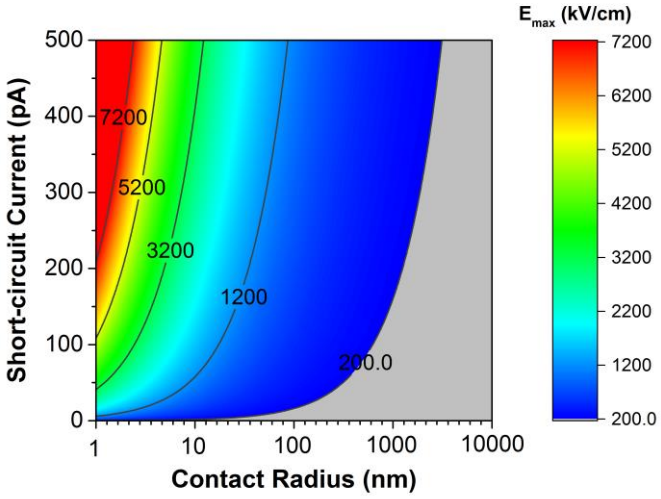

Figure 7-16. The maximum electrical field generated by the tip-enhanced photovoltaic effect in the $BiFeO_3$ film as a function of the contact radius and short-circuit current magnitude. Mobility μ is assumed to be 1 cm^2/Vs.

field distribution is now different (uniform, parallel) and effective field decreases dramatically to a value smaller than the E_c.

Keeping in perspective the giant electrical field generated by the tip-enhanced PV effect, one may perceive the possibility to induce ionic migration underneath the tip. To verify this possibility, we studied the effect of tip-enhanced PV effect on the surface morphology. Specifically, the I_{SC} was probed by the conductive AFM tip at some predetermined positions on the BFO/SRO surface for about 5 seconds and then the modified surface morphology was characterize. We found that the large negative I_{SC}, i.e., current flowing from the tip into the BFO film, exhibits pronounced effect on the surface morphology (see Fig. 7-17) whereas positive I_{SC} shows negligible effect on the morphology. The positions where negative I_{SC} (~ -200 pA) was probed turn to high bumps, pointing to a potential ionic migration or local breakdown. This light-induced ionic migration, in turn, demonstrates the manifestation of the giant electrical field underneath the tip contact area resulted from the tip-enhanced PV effect.

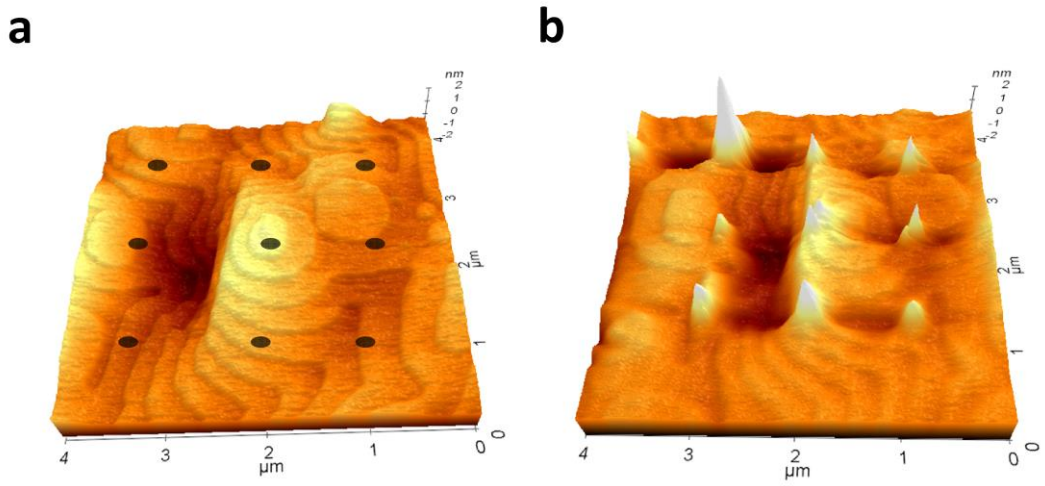

Figure 7-17. Photo-induced ionic migration in $BiFeO_3$ thin film. (a) The pristine surface morphology of a 4×4 μm^2 area on the $BiFeO_3/SrRuO_3$ film. The black dots indicate the positions where the light-induced negative short-circuit current will be probed by the AFM tip. (b) The resultant surface morphology after probing the negative current at the predetermined positions.

7.3.4 Reversible Switching of Ferroelectric Polarisation by Light

To achieve full optical control of ferroelectric variants, one needs to reversibly switch the ferroelectric polarisation. Keeping in perspective the essential role of the I_{SC}, one can perceive that this can be achieved by tuning the I_{SC} directions at the tip contact region.

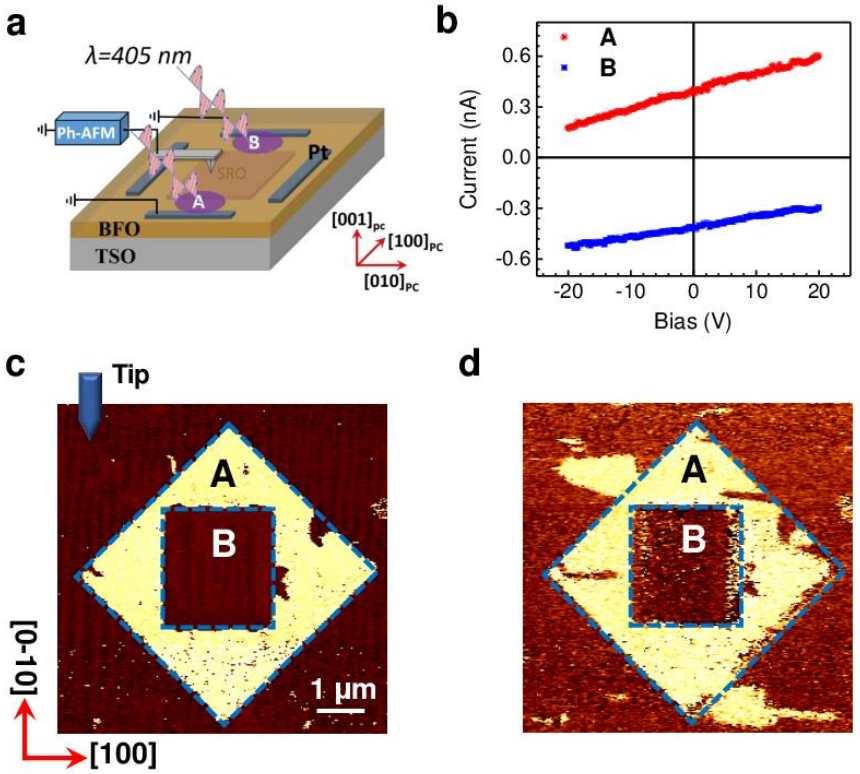

Figure 7-18. Light-induced reversible switching of ferroelectric polarisation via tuning illumination area. (a) Illumination configuration schematically showing two areas on the $BiFeO_3/TbScO_3$ surface giving rise to opposite current directions at the tip contact area. (b) Current-voltage characteristics acquired by illuminating area A and B, respectively. (c) Out-of-plane and (d) in-plane PFM phase signals of an optically written box-in-box domain structures in a 6×6 μm^2 area by illuminating area A and B subsequently during the PhAFM scanning processes. While doing the PhAFM scans, the fast scan direction of the tip is along the $[100]_{pc}$ direction and the slow direction is towards the $[010]_{pc}$ direction.

This can be realized in two ways. First possibility is to tune the illumination geometry. Fig. 7-18a shows schematically the illumination strategy where illumination upon area A gives rise to a I_{SC} flowing from the BFO/SRO film into the tip whereas illuminating light on area B generates a I_{SC} running in the opposite direction, as demonstrated in Fig. 7-18b. This is due to the fact that the I_{SC} originated from the BPV effect is solely related to the crystallographic structure. In this particular geometry and the BFO/TSO film, the I_{SC} always flows along the $[100]_{pc}$ direction when the grounded stripe electrodes run along $[010]_{pc}$ direction. As a result, illuminating area A would generate a large positive electric field underneath the tip while illuminating area B would give rise to a negative field. So, by alternatively illuminating area A and B, one can reversibly switch the ferroelectric polarisation by light. The PhAFM tip firstly scans a 4×4 μm^2 area on the BFO/SRO

surface while illuminating area A. Afterwards, the tip scans an inner 2×2 μm^2 area by illuminating area B. As clearly shown in Fig. 7-18c and 18d, both the out-of-plane and in-plane ferroelectric polarisation of the scanned area was switched from negative to positive and then back to negative, demonstrating the full control of the ferroelectric polarisation by light.

Finding a certain illumination parameter that would allow reversible ferroelectric switching without modifying the light beam position would be a real advantage, enabling developing future applications and devices. To achieve this, we exploit another feature that is uniquely related to the BPV effect, respectively dependence of I_{SC} on the light polarisation. We thus explore reversible control of ferroelectric polarisation by using the light polarisation as the tuning parameter. The illumination geometry for this purpose is shown in Fig. 19 where the grounded stripe electrode runs along BFO $[100]_{pc}$ direction instead. Both magnitude and direction of the I_{SC} in this geometry depends on the incident light polarisation angle, as demonstrated in Fig. 7-20. Note that the light polarisation angle mentioned here refers to the angle between the light polarisation and the BFO $[100]_{pc}$ crystallographic direction. The I_{SC} probed by the tip reaches a positive maximum at the light polarisation angle of $45° + 180°n$, whereas it turns to a negative maximum at the angle of $135° + 180°n$ $(n = 1,2,3 \ldots)$. This is consistent with previous reports which utilized coplanar electrodes running parallel to the in-plane polarisation of the BFO film (see Fig. 6-4d)[12,106,138].

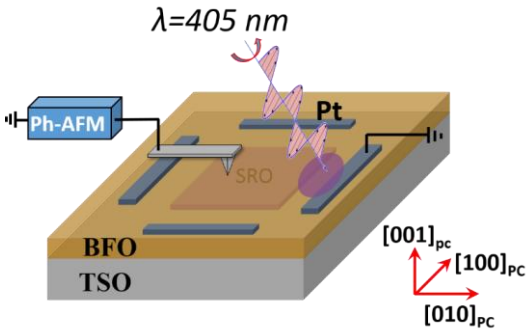

Figure 7-19. Schematic showing the device configuration and illumination area for the light polarisation controlled optically switching ferroelectric polarisation.

The possibility of light polarisation induced reversible ferroelectric switching was first studied by local PFM spectroscopic measurements. The local PFM response, i.e., both phase and amplitude of the out-of-plane PFM signal of a fixed position on the BFO/SRO surface, was monitored while illuminating the BFO/TSO surface and continuously rotating the light polarisation. As clearly illustrated in Fig. 7-20b, the PFM phase signal switches between - 90° and 90° reversibly while rotating the light polarisation. Meanwhile, the PFM amplitude signal decreases to about zero when the phase signal switching processes happen (Fig. 7-20c). This simple experiment confirms that the local ferroelectric polarisation can be fully and reversibly switched between negative and positive directions by solely rotating the light polarisation. The light polarisation controlled ferroelectric switching was further explored

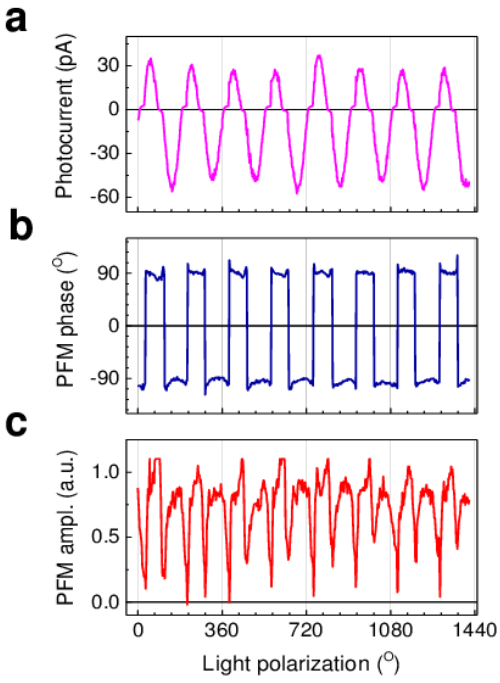

Figure 7-20. The light polarisation dependence of (a) short-circuit photocurrent (I_{SC}), (b) out-of-plane PFM phase signal and (c) amplitude signal.

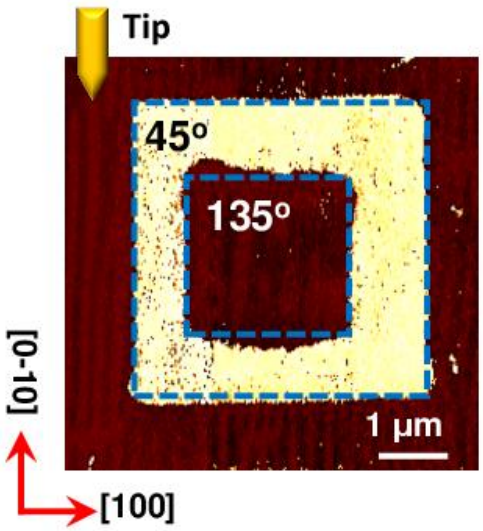

Figure 7-21. Light polarisation dependent optically-written out-of-plane domain structures. The AFM cantilever is along $BiFeO_3$ $[010]_{pc}$ crystallographic direction.

by the scanning method. The AFM tip firstly scans a 4×4 μm^2 area on the BFO/SRO surface while illuminating the BFO/TSO surface with a light polarisation angle of $45°$ and then scans an inner 2×2 μm^2 area with $135°$ light polarisation illumination. The resultant domain structure is subsequently characterized by PFM performed in the dark. As clearly demonstrated in Fig. 7-21, the domain structures have been reversibly switched from the pristine negative direction to positive and then back to the negative direction.

7.4 Conclusion

We have demonstrated fully optical control of ferroelectric domains in BFO thin films at room temperature. This is mediated by the tip-enhanced photovoltaic effect which gives rise to a dramatic enhancement of the current density at the tip contact area as well as a local electric field, which exceeds the coercive field and leads to the local ferroelectric switching. Reversible ferroelectric polarisation switching can be achieved using two particularities of the BPV effect, namely the dependence on the crystallographic direction and light polarisation. Effectively, all-optical light polarisation dependent switching (AO-LPDS) in the multiferroic/ferroelectric system can be achieved by simply rotating the light polarisation or tuning the illumination configuration. Owing to the innate multiferroic nature and strong magnetoelectric coupling between the antiferromagnetic and ferroelectric/ferroelastic orders in the BFO film[143,144], this AO-LPDS will, in principle, also simultaneously manipulate the antiferromagnetic and ferroelastic orders in this multiferroic material. Hence, light is able to fully control all the ferroic orders at room temperature, paving the way for developing novel opto-ferroic and opto-magnetoelectric devices for data storage and sensing.

Chapter 8. Flexo-Photovoltaic Effect

The Shockley-Queisser detailed-balance limit constrains the ultimate power conversion efficiency of solar cells based on charge separation by the built-in electric field at a *p*-*n* junction. It is therefore highly desirable to find novel photovoltaic mechanisms that can enable higher efficiency solar cells. Here, we report that the bulk photovoltaic effect, which exceeds the Shockley-Queisser limit but is manifested only in noncentrosymmetric (piezoelectric or ferroelectric) materials, can be realized in any semiconductor, including silicon, by mediation of the flexoelectric effect. Strain gradients are introduced using either an atomic force microscope on the nano-scale, or a micron-scale indentation system, reminiscent of the early transistor era, creating giant photovoltaic currents from centrosymmetric single crystals of $SrTiO_3$, TiO_2, and Si. This strain-gradient-induced bulk photovoltaic effect is designated here the flexo-photovoltaic effect, and functions in the absence of a *p*-*n* junction. This finding will extend significantly present solar cell technologies by boosting the solar energy conversion efficiency from a wide pool of established semiconductors.

8.1 Introduction

Although bulk photovoltaic effects in ferroelectrics have been known for 50 years, they have remained largely an academic curiosity, mainly because of their reported low power-conversion efficiency. Despite that it shows an anomalous photovoltage and potential to overcome the Shockley-Queisser (S-Q) limit[104], a substantial BPV effect is usually found in wide-bandgap *noncentrosymmetric* materials, such as ferroelectric $BaTiO_3$[145] and $BiFeO_3$[12], leading to an overall extremely low quantum efficiency under solar illumination. On the other hand, conventional solar cells consisting of *p*-*n* junctions have now become the mainstay of the modern solar industry, contributing more than 1% of the global electricity supply owing to the appropriate bandgap energies of the component semiconductors that can absorb most of the sunlight. Nevertheless, these PV cells have a photovoltage limited by the bandgap energy of the constituent semiconductors, and an ultimate efficiency constrained by the S-Q limit[146]. Concerning the respective features of two PV mechanisms mentioned above, an intuitive way to enhance the PV effect is to realize the BPV effect in semiconductors with appropriate bandgaps, regardless of their crystalline symmetry.

Inspired by this idea, we turn our focus to the flexoelectric effect. Flexoelectricity is an electromechanical property defining a coupling between an electric polarisation and a strain gradient[147,148]. In centrosymmetric materials, a strain gradient breaks the structural centrosymmetry, resulting in a strain-induced polarisation with a preferred direction. In other words, by symmetry breaking, flexoelectricity enables a piezoelectric composite containing no piezoelectric elements[52,148]. Keeping this in mind, one can hypothesize that a strain gradient, by breaking centrosymmetry, allows the manifestation of the BPV effect in materials even originally possessing a centrosymmetric structure. Thus, we propose and demonstrate here a new photovoltaic effect which turns the BPV effect into a universal effect allowed in all semiconductors by mediation of the flexoelectric effect. Given that flexoelectricity is a universal property of all materials, ranging from bio-materials[149] to semiconductors and dielectrics[150] to 2D materials such as graphene[151], this strain-gradient-induced BPV effect, termed here the flexo-photovoltaic (FPV) effect, is allowed for all symmetry classes. Thus the devices based on the FPV effect can be fabricated with silicon or any other semiconductor.

8.2 Experimental Setup and Sample Preparation

To prove our idea, we explored the PV effect induced by a point force exerted locally onto the surface of centrosymmetric materials including a $SrTiO_3$ single crystal and a rutile TiO_2 single crystal. The point force was exerted by the tip of an atomic force microscope (AFM), inducing local inhomogeneous strain at the tip/surface contact area and, therefore, a local breaking of centrosymmetry[152,153]. For our experiments, we used the PhAFM system as discussed in previous chapters. The optical system allows us to illuminate a sample surface with a 405 nm laser properly polarized by a half-wavelength plate. A conductive AFM tip applies a local force on a sample surface and simultaneously collects the resulting PV current, as schematically shown in Fig. 8-1a and 1b. The tip loading force is controlled by the AFM feedback loop.

Additionally, we also use a home-built micro-indenter system to induce local inhomogeneous deformation by pressing sample surface with a tungsten needle. As shown in Fig. 8-1c, the micro-indenter system consists of a vertically moving stage, a spring with a spring constant of 2 N/mm and a tungsten probe needle with an apex diameter of about 10 μm. The moving stage lifts up and down the sample mounted on top

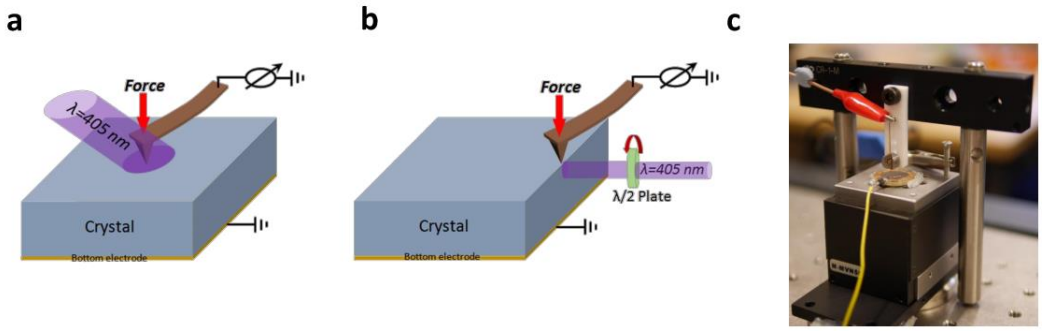

Figure 8-1. Brief schematics of the experimental setup for flexo-photovoltaic effect. (a) Setup for illumination around the contact area. (b) Setup for illumination on the side surface. (c) Photography of the home-built micro-indenter

of the spring by rotating the micrometre. The force is controlled by the compressed length of the spring after the sample is contact with the probe. A linearly polarized light illuminates the sample surface.

Regarding the samples of interests, we use both $SrTiO_3$ and TiO_2 single crystals of different orientation which are commercially available from Crystec GmbH. We cleaned them with acetone, isopropanol and deionized water before the measurements

8.3 Results and Discussion

8.3.1 Force-induced Photovoltaic Effect

$SrTiO_3$ single crystal is one of the ideal systems to study the flexoelectric effect thanks to its simple cubic centrosymmetric lattice and large dielectric permittivity[150,154]. Unlike its sister material $BaTiO_3$, ordinary $SrTiO_3$ crystals do not exhibit the BPV effect because of their inversion symmetry. But, with illumination around the contact area on a (001)-face of $SrTiO_3$ crystal, we observed a clear contrast in I_{SC} which is –0.1 pA at most under the 1 μN loading force but rises to more than –25 pA through a transient peak on increasing the loading force (Fig. 8-2). This force-

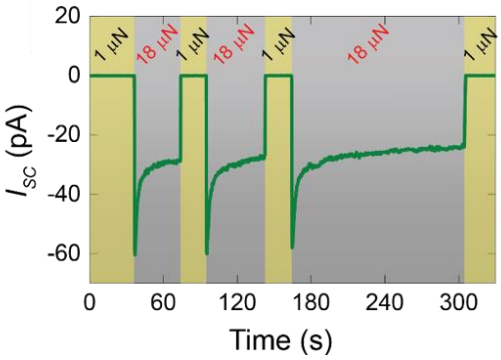

Figure 8-2. Evolution of the photocurrent induced and collected by a conductive AFM tip with a high loading force on $SrTiO_3$ (001) face.

induced I_{SC} is reproducible, as proven by repeated exertion/withdrawal of the loading force.

To show that the giant enhancement of I_{SC} by the loading force is not confined to a $SrTiO_3$ crystal or a cubic structure, we further investigated the FPV behaviours in a single crystal of rutile TiO_2, which is famous for its photoelectric applications such as dye-sensitized photovoltaic cells and photo-catalysis. Rutile TiO_2 single crystal possesses a centrosymmetric tetragonal structure with a bandgap of 3.05 eV. As in the previous case of $SrTiO_3$, large negative I_{SC} appears once a large force is exerted on a TiO_2 (100) face. Fig. 8-3 shows the stable current under the 15 μN force, confirming that the force-induced PV effect is not a transient effect. Although it depends on contact conditions and locations, the point force exerted by the AFM tip gives rise to a substantial current density up to 5 A/cm^2 at the nanoscale contact, which is over three order of magnitude higher than I_{SC} (0.3 mA/cm^2) from the Schottky junction between TiO_2 and Pt under the same illumination condition. The current density increases more than 100 times by simply increasing the loading from 1 to 15 μN (Fig. 8-4a).

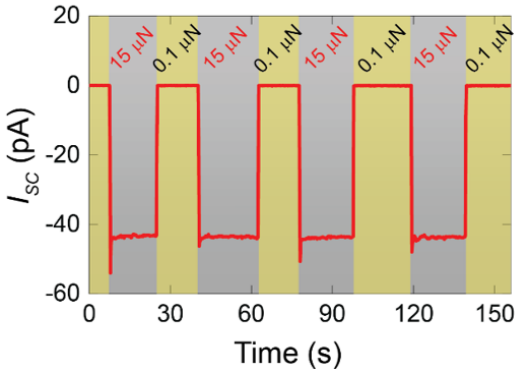

Figure 8-3. Evolution of the photocurrent induced and collected by a conductive AFM tip with a high loading force on TiO_2 (100) face.

This cannot be explained with an increase of the contact area with the loading force because a contact area increases at most ~6 times with a 15 times larger contact force in a simple elastic sphere contact model. Moreover, a 100-time increase of the contact area with an AFM tip is unphysical. Furthermore, we found that I_{SC} turns to a positive value when loading the conductive AFM tip on a (001)-face of the TiO_2 crystal in contrast to the negative value of I_{SC} on its (100)-face (Fig. 8-4b). The fact that the direction of the PV current depends on the crystallographic orientation of the TiO_2 crystal indicates that the observed PV effect cannot be merely attributed to a probable Schottky contact formed between the TiO_2 surface and the Pt-coating of the AFM tip.

A potential origin of this PV current enhancement is the BPV effect. As hypothesized, it is likely that a point force exerted on a crystal surface generates a local strain gradient, resulting in local centrosymmetry breaking and, thus, a local BPV current under

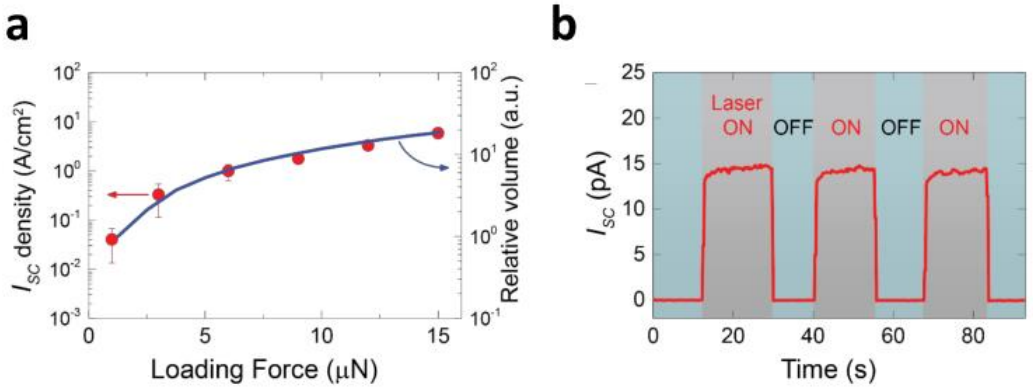

Figure 8-4. (a) The dependence of the induced photocurrent density and the relative volume subject to the strain gradient higher than 1×10^6 m^{-1} on the loading force. (b) Positive photocurrent measured on TiO_2 (001) face with a 15 μN force applied by the AFM tip.

illumination, i.e., the FPV effect, in the absence of a *p-n* junction and an appropriate band alignment. Given that both the flexoelectric response and the BPV effect depend on the crystallographic orientation[120,154,155], it strongly suggests a predominant role of the asymmetric strain gradient and the resultant FPV effect in the enhanced local PV current.

8.3.2 Strain and Strain Gradient Distribution under Point Force

The strain induced by a sphere contact has a complex spatial distribution with giant strain gradient values in an elastic material. An AFM tip apex can be assumed as a hemisphere and the distribution of strain gradient induced by the AFM tip can be calculated analytically with the Hertzian model and Boussinesq's calculation[156]. The principle of superposition with the Boussinesq solution for a point contact gives the stress distribution for any distribution of pressure within a contact area. In a cylindrical coordinate system with the origin at the centre of the contact area, the normal pressure distribution directly beneath a spherical indenter is

$$\frac{\sigma_Z(r)}{p_m} = -\frac{3}{2}\sqrt{1-\frac{r^2}{a^2}} \qquad (r \le a) \tag{8-1}$$

where σ_z is a *z*-component of stress, p_m is a mean pressure applied to the whole contact area beneath the indenter, and a is the contact radius.

By the superposition principle, the stress distribution will be

$$\frac{\sigma_r(r,z)}{p_m}=\frac{3}{2}\left\{\begin{aligned}&\frac{1-2\nu}{3}\frac{a^2}{r^2}\left[1-\left(\frac{z}{\sqrt{u}}\right)^3\right]+\left(\frac{z}{\sqrt{u}}\right)^3\frac{a^2u}{u^2+(az)^2}\\&+\frac{z}{\sqrt{u}}\left[\frac{u(1-\nu)}{a^2+u}+\frac{(1+\nu)\sqrt{u}}{a}arctan\left(\frac{a}{\sqrt{u}}\right)-2\right]\end{aligned}\right\} \quad (8\text{-}2)$$

$$\frac{\sigma_\theta(r,z)}{p_m}=-\frac{3}{2}\left\{\begin{aligned}&\frac{1-2\nu}{3}\frac{a^2}{r^2}\left[1-\left(\frac{z}{\sqrt{u}}\right)^3\right]\\&+\frac{z}{\sqrt{u}}\left[2\nu+\frac{u(1-\nu)}{a^2+u}-\frac{(1+\nu)\sqrt{u}}{a}arctan\left(\frac{a}{\sqrt{u}}\right)\right]\end{aligned}\right\} \quad (8\text{-}3)$$

$$\frac{\sigma_z(r,z)}{p_m}=-\frac{3}{2}\left(\frac{z}{\sqrt{u}}\right)^3\left(\frac{a^2u}{u^2+(az)^2}\right) \quad (8\text{-}4)$$

where ν is a Poisson's ratio and $u=\frac{1}{2}\{(r^2+z^2-a^2)+\sqrt{(r^2+z^2-a^2)^2+(2az)^2}\}$. From Hooke's law, the strain will be

$$\varepsilon_r(r,z)=\frac{1}{Y}\left[\sigma_r-\nu(\sigma_\theta+\sigma_z)\right] \quad (8\text{-}5)$$

$$\varepsilon_\theta(r,z)=\frac{1}{Y}\left[\sigma_\theta-\nu(\sigma_z+\sigma_r)\right] \quad (8\text{-}6)$$

$$\varepsilon_z(r,z)=\frac{1}{Y}\left[\sigma_z-\nu(\sigma_r+\sigma_\theta)\right] \quad (8\text{-}7)$$

Here, *Y* is the Young's modulus. A positive (negative) value corresponds to the tensile (compressive) strain along the respective axis. Shown in Fig. 8-5 is the strain distribution as functions of *r*, θ, and *z*, respectively. Each strain gradient can be obtained by a partial derivative with respect to *r*, θ, or *z*, as shown in Fig.8-6. In our calculation, we set ν =

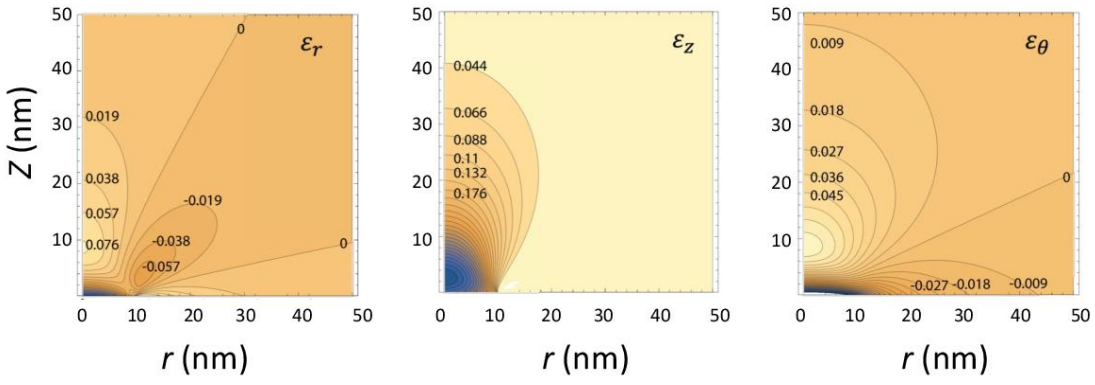

Figure 8-5. Contour maps of the r, θ, and z components of the strain induced by a spherical indenter with a contact radius of 10 nm.

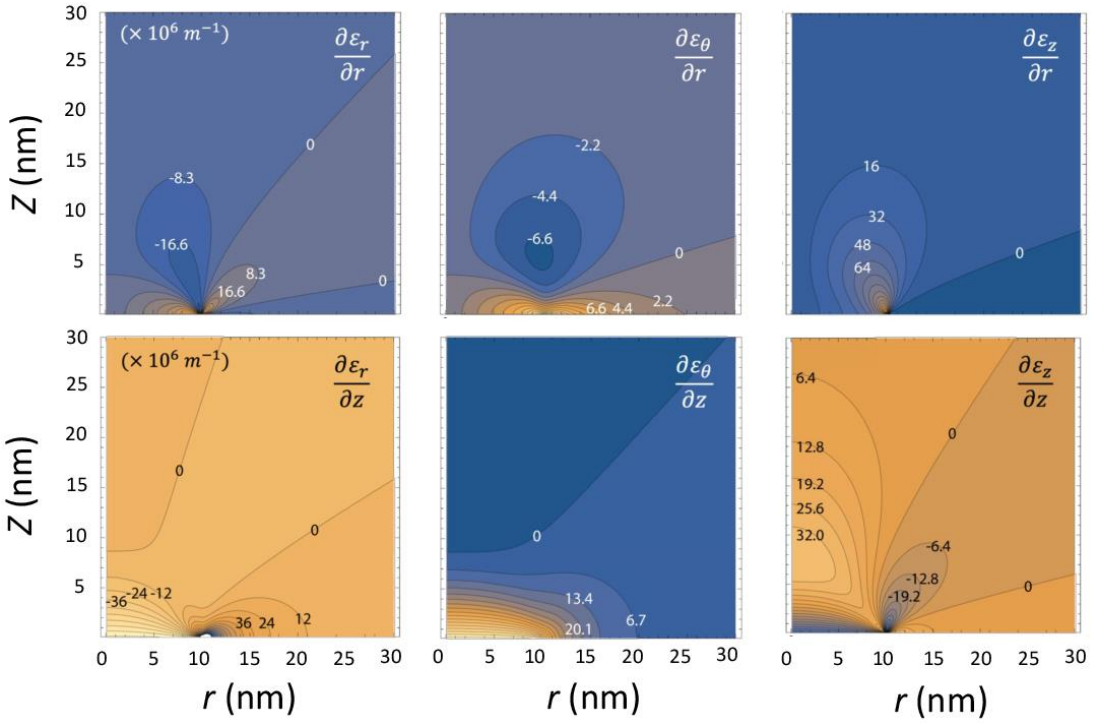

Figure 8-6. Contour maps of the partial derivatives of the *r*, *θ*, and *z* components of the strain induced by a spherical indenter with a contact radius of 10 nm. The contact area with a radius of 10 nm is centred at the origin, and the force is pointing upward. The positive (negative) value of the strain means a tensile (compressive) strain.

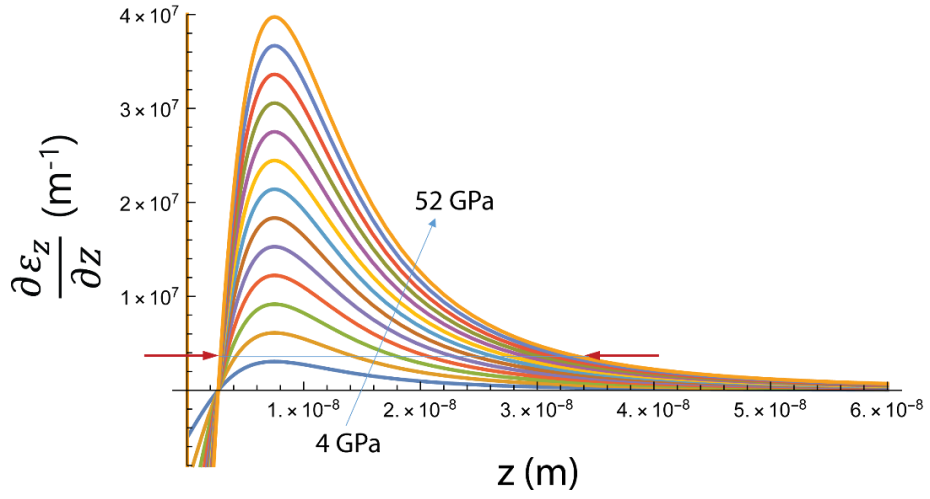

Figure 8-7. The z-derivative of the z-component of the strain gradient at r ≈ 0 as a function of z with different loading stress from 4 GPa to 52 GPa (The point r = 0 is a singularity point).

0.22, Y = 100 GPa, a = 10 nm, and p_m = 50 GPa (equivalently, ca. 15.7 μN of the tip loading force). The force is exerted toward the positive direction (upward) in z axis. The strain gradient is as large as 10^7 m^{-1}. Interestingly, we found that the I_{SC} density and the volume beneath the AFM tip being subject to a strain gradient larger than 1×10^6 m^{-1} show similar dependence on the exerted force (see Fig. 8-4a). Details on the strained volume is shown in Fig. 8-7. It is expected that the giant strain gradients induced by the AFM tip break local symmetry, leading to the manifestation of the BPV effect locally under illumination. However, a relationship between the complex distribution of the strain gradient and the BPV properties should be quite intricate and deep theoretical considerations are required.

Note that in Fig. 8-4, we determined the volume subject to a strain gradient larger than 1×10^6 m^{-1} as following. The depth subject to the strain gradient was determined by the distance between two red arrows in the figure, which increases with the loading stress as the curve is higher and wider with the higher loading stress. Then, the volume was approximately estimated by cube of the determined depth. The relative volume in Fig. 8-4 was obtained by normalizing with the volume obtained in the curve of 4 GPa stress.

8.3.3 Origin of the Force-induced Photovoltaic Effect

The main characteristic of the BPV effect, stemming from its tensorial nature, is a periodic dependence on the angle between the PV current and the light polarisation[102]. For the present case, the FPV effect proposed by us is the collective effect of local BPV effect manifested in the strain-gradient-induced non-centrosymmetric structures. Here, we demonstrate that the PV current resulting from the FPV effect also possesses the light polarisation dependence, which distinguishes the FPV effect from other PV effect such as those of p-n junctions and Schottky barriers. For the model, a force $\boldsymbol{F}$ applied at point $\boldsymbol{O}$ along Z direction by a conductive AFM tip generates a complex strain gradient and induces non-centrosymmetric structures in the volume beneath the contact area, as shown in Fig. 8-8. By assuming the apex of the AFM tip is of hemispherical shape, the structure of deformed volume possesses an infinite rotational symmetry with respect to Z axis. Per Neumann's Principle, "*The symmetry elements of any physical property of a crystal must include the symmetry elements of the point group of the crystal*", the distribution of the BPV tensor of local non-centrosymmetric structures also has the infinite rotational symmetry with respect to Z axis which means the BPV tensor is independent of the parameter θ.

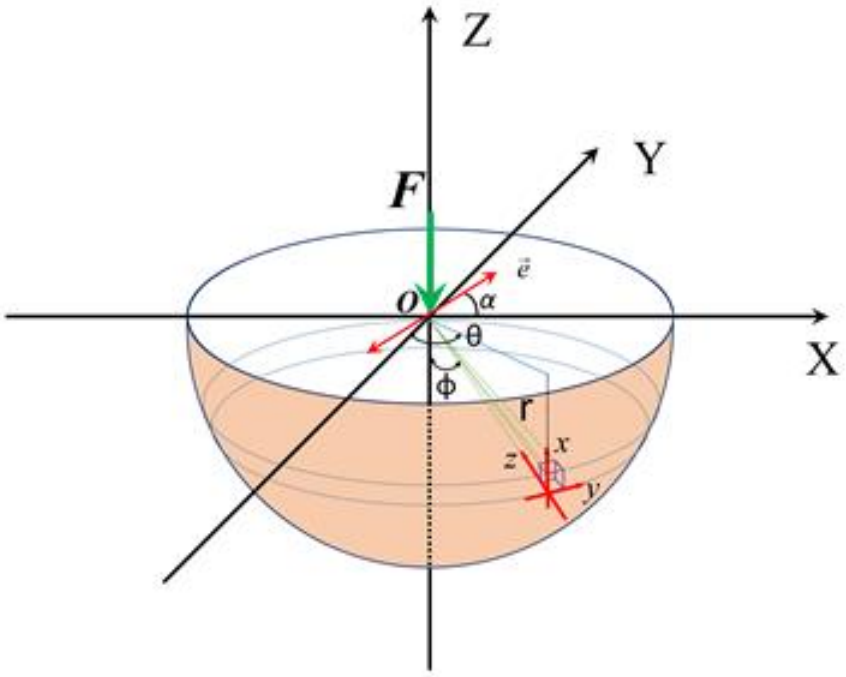

Figure 8-8. A schematic shows the spherical coordinate and related parameters to calculate the light polarisation ($\vec{e}$) dependence of the flexo-photovoltaic current induced by a point force. The linearly polarized light illuminates the strained area along Y axis and the light polarisation is rotated within the ZX plane.

Given that the expression of a tensor depends on the chosen reference system, the local coordinate in each local non-centrosymmetric structure shall also possess the infinite rotational symmetry with respect to Z axis in order to retain the rotational symmetry for the expressions of local BPV tensor elements. For this purpose, as the red coordination indicated in Fig. 8-8, the *z* axis of the local coordinate always points to the origin O where the force is exerted and the *y* axis is always parallel to the XY plane and perpendicular to the *z* axis. The *x* axis is set orthogonal to both *y* and *z* axes to form a right hand Cartesian coordinate system. Accordingly, a general BPV tensor of a local non-centrosymmetric structure can be expressed as[83,102]

$$\boldsymbol{\beta}_{ijk}(r,\phi)=\boldsymbol{\beta}_{ij}(r,\phi)=\begin{pmatrix}\beta_{11} & \beta_{12} & \beta_{13} & \beta_{14} & \beta_{15} & \beta_{16}\\ \beta_{21} & \beta_{22} & \beta_{23} & \beta_{24} & \beta_{25} & \beta_{26}\\ \beta_{31} & \beta_{32} & \beta_{33} & \beta_{34} & \beta_{35} & \beta_{36}\end{pmatrix} \tag{8-8}$$

The resultant local BPV current is also dictated by the light polarisation with respect to the structure which can be expressed as[102]:

$$J_i = I_o \boldsymbol{\beta}_{ijk} \boldsymbol{e}_j \boldsymbol{e}_k \tag{8-9}$$

where J_i is the current density along i direction ($i = x, y, z$), I_o is the light intensity, $\boldsymbol{e}_j$ and $\boldsymbol{e}_k$ are the electrical field vectors of the incident light. Thus, it is crucial to calculate the expression for the light polarisation vector in the local coordinate. Given a particular geometry wherein the linear polarized light illuminates along the Y direction, the light polarisation can be expressed in the global coordinate (XYZ) as:

$$e = (\cos\alpha, 0, \sin\alpha) \tag{8-10}$$

where α is the angle between the light polarisation and the X-axis. The transformation of a vector expression from the (XYZ) coordinate into the local (*xyz*) coordinate located at (r,θ,ϕ) can be given as:

$$\begin{pmatrix} x \\ y \\ z \end{pmatrix} = \begin{pmatrix} \cos\theta\cos\phi & \sin\theta\cos\phi & \sin\phi \\ -\sin\theta & \cos\theta & 0 \\ -\cos\theta\sin\phi & -\sin\theta\sin\phi & \cos\phi \end{pmatrix} \begin{pmatrix} X \\ Y \\ Z \end{pmatrix} \tag{8-11}$$

Accordingly, the light polarisation can be expressed in the local coordinate as:

$$\begin{pmatrix} e_x \\ e_y \\ e_z \end{pmatrix} = \begin{pmatrix} \cos\theta\cos\phi\cos\alpha + \sin\phi\sin\alpha \\ -\sin\theta\cos\alpha \\ -\sin\phi\cos\theta\cos\alpha + \cos\phi\sin\alpha \end{pmatrix} \tag{8-12}$$

Then, the product $\boldsymbol{e}_j\boldsymbol{e}_k$ can be calculated as

$$\boldsymbol{e}_j\boldsymbol{e}_k = \begin{bmatrix} e_x^2 & e_y^2 & e_z^2 & 2e_ye_z & 2e_xe_z & 2e_xe_y \end{bmatrix}^T \tag{8-13}$$

Based on the above equations, the product $\boldsymbol{e}_j\boldsymbol{e}_k$ is a function of θ, ϕ and α. According to the configuration of the local coordination, only the BPV current density along *z* axis, i.e., J_z contributes to the current collected by the conductive AFM tip pressing at point ***O***, which can be expressed as:

$$J_z(r,\theta,\phi) = I_o\boldsymbol{\beta}_{3j}(r,\phi)\boldsymbol{e}_j\boldsymbol{e}_k(\theta,\phi,\alpha) \tag{8-14}$$

Given that the current is defined as the amount of charge flowing through a unit area within a unit time, we shall calculate the number of carriers moving to (or away from) the point ***O*** along the *z* axis within a unit time. The carrier number generated by the non-centrosymmetric infinitesimal element situated at (r,θ,ϕ) can be expressed as:

$$dn_z(r,\theta,\phi) = \frac{1}{e} j_z(r,\theta,\phi)\, dA_z(r,\theta,\phi) \tag{8-15}$$

$$dA_z(r,\theta,\phi) = r^2 \sin\phi d\theta d\phi \tag{8-16}$$

As seen in Eq. (8-8), the BPV tensor elements vary as a function of the parameter *r* in the radial direction with angle of (θ,ϕ). Therefore, the number of carriers $dn_z(r,\theta,\phi)$ generated by the non-centrosymmetric structures in the (θ,ϕ) radial direction changes with *r*. However, the number of carriers $d\bar{n}_z(\theta,\phi)$ in the (θ,ϕ) radial direction is *r*-independent under the steady-state condition due to the particle conservation principle. Providing that the conductivity σ retains a constant value in the deformed area, the steady-state number of carriers $d\bar{n}_z(\theta,\phi)$ moving in the (θ,ϕ) radial direction can be estimated as a volume average:

$$d\bar{n}_z(\theta,\phi) = \frac{\int_0^L dn_z(r,\theta,\phi)\, dV(r,\theta,\phi)}{\int_0^L dV(r,\theta,\phi)} \tag{8-17}$$

where $dV(r,\theta,\phi) = r^2 \sin\phi dr d\theta d\phi$ is the volume of the non-centrosymmetric structure located at the point (r,θ,ϕ) and L is the distance within which the strain gradient exists. As shown in previous section, the value of L depends on the magnitude of the force for a specific material.

By substituting Eq. (8-14)-(8-16) into Eq. (8-17), we can get:

$$d\bar{n}_z(\theta,\phi) = \frac{1}{e} I_o \boldsymbol{\beta}_{3j}(\phi) \boldsymbol{e}_j \boldsymbol{e}_k(\theta,\phi,\alpha) \sin\phi d\theta d\phi \tag{8-18}$$

$$\boldsymbol{\beta}_{3j}(\phi) = \frac{3\int_0^L \boldsymbol{\beta}_{3j}(r,\phi) r^4 dr}{L^3} \tag{8-19}$$

Then the number of carriers $d\bar{n}_z(\phi)$ located at the radial layer between ϕ and $\phi + d\phi$ is calculated by integration of $d\bar{n}_z(\theta,\phi)$ over θ in the range between 0 and 2π, which gives:

$$d\bar{n}_z(\phi) = \frac{1}{e} I_o \boldsymbol{\beta}_{3j}(\phi) \boldsymbol{e}_j \boldsymbol{e}_k(\phi,\alpha) \sin\phi d\phi \tag{8-20}$$

$$\boldsymbol{e}_j \boldsymbol{e}_k(\phi,\alpha) = \int_0^{2\pi} \boldsymbol{e}_j \boldsymbol{e}_k(\theta,\phi,\alpha) d\theta \tag{8-21}$$

Substituting Eq.(8-12) and (8-13) into Eq. (8-21), we can get:

$$\boldsymbol{e}_j\boldsymbol{e}_k\left(\phi,\alpha\right)=\begin{pmatrix} e_x^2 \\ e_y^2 \\ e_z^2 \\ 2e_ye_z \\ 2e_xe_z \\ 2e_xe_y \end{pmatrix}=\begin{pmatrix} \pi cos^2\phi cos^2\alpha+2\pi sin^2\phi sin^2\alpha \\ \pi cos^2\alpha \\ 2\pi cos^2\phi sin^2\alpha+\pi sin^2\phi cos^2\alpha \\ 0 \\ \pi sin2\phi\left(3sin^2\alpha-1\right) \\ 0 \end{pmatrix} \tag{8-22}$$

Thus, the total number of carriers $\bar{n}_z$ moving towards the point ***O*** in a unit time can be calculated integrating $d\bar{n}_z\left(\phi\right)$ over ϕ in the range from 0 to π/2:

$$\bar{n}_z=\frac{1}{e}I_o\int_0^{\pi/2}\boldsymbol{\beta}_{3j}\left(\phi\right)\boldsymbol{e}_j\boldsymbol{e}_k\left(\phi,\alpha\right)sin\phi d\phi \tag{8-23}$$

The magnitude of the current probed at the point ***O*** can be readily given as:

$$I_{sc}=e\bar{n}_z \tag{8-24}$$

By substituting Eq. (8-20)-(8-22) into Eq. (8-24), we can get

$$\begin{aligned} I_{SC}=&\frac{\pi}{2}I_o\begin{bmatrix}\int_0^{\pi/2}\beta_{31}\left(\phi\right)\left(1+sin^2\phi\right)sin\phi d\phi+\int_0^{\pi/2}\beta_{32}\left(\phi\right)sin\phi d\phi \\ +\int_0^{\pi/2}\beta_{33}\left(\phi\right)\left(1+cos^2\phi\right)sin\phi d\phi+\int_0^{\pi/2}\beta_{35}\left(\phi\right)sin2\phi sin\phi d\phi\end{bmatrix} \\ &+\frac{\pi}{2}I_o cos2\alpha\begin{bmatrix}\int_0^{\pi/2}\beta_{31}\left(\phi\right)\left(3cos^2\phi-2\right)sin\phi d\phi+\int_0^{\pi/2}\beta_{32}\left(\phi\right)sin\phi d\phi \\ +\int_0^{\pi/2}\beta_{33}\left(\phi\right)\left(1-3cos^2\phi\right)sin\phi d\phi-3\int_0^{\pi/2}\beta_{35}\left(\phi\right)sin2\phi sin\phi d\phi\end{bmatrix}\end{aligned} \tag{8-25}$$

The sum in the brackets of the above equation becomes two constants which can be denoted as A_z and B_z, respectively.

$$\begin{aligned} A_z=&\int_0^{\pi/2}\beta_{31}\left(\phi\right)\left(1+sin^2\phi\right)sin\phi d\phi+\int_0^{\pi/2}\beta_{32}\left(\phi\right)sin\phi d\phi \\ &+\int_0^{\pi/2}\beta_{33}\left(\phi\right)\left(1+cos^2\phi\right)sin\phi d\phi+\int_0^{\pi/2}\beta_{35}\left(\phi\right)sin2\phi sin\phi d\phi\end{aligned} \tag{8-26}$$

and

$$\begin{aligned} B_z=&\int_0^{\pi/2}\beta_{31}\left(\phi\right)\left(3cos^2\phi-2\right)sin\phi d\phi+\int_0^{\pi/2}\beta_{32}\left(\phi\right)sin\phi d\phi \\ &+\int_0^{\pi/2}\beta_{33}\left(\phi\right)\left(1-3cos^2\phi\right)sin\phi d\phi-3\int_0^{\pi/2}\beta_{35}\left(\phi\right)sin2\phi sin\phi d\phi\end{aligned} \tag{8-27}$$

Thus, the PV current collected at point ***O*** can be simply expressed as:

$$I_{SC} = \frac{\pi}{2} I_o \left(A_z + B_z cos2\alpha \right) \tag{8-28}$$

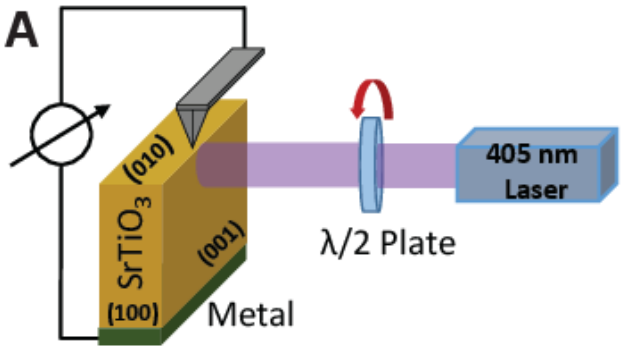

Figure 8-9. Sketch of the setup used to measure the light polarisation dependence of the PV current.

Clearly, the FPV effect inherits the distinctive feature of the BPV effect that the PV current exhibits a cosine dependence on the incident light polarisation angle with a period of 180°. Indeed, I_{SC} measured by a conductive AFM tip in the configuration illustrated in Fig. 8-9 on the $SrTiO_3$ (010) and TiO_2 (001) surfaces exhibits a light polarisation dependence in accord with Eq. (8-28), as seen in Fig. 8-10a and 10b. The sinusoidal behaviour upon rotating the polarisation proves that the underlying mechanism of the force-induced PV effect is the BPV effect mediated by the flexoelectricity, namely the flexo-photovoltaic effect.

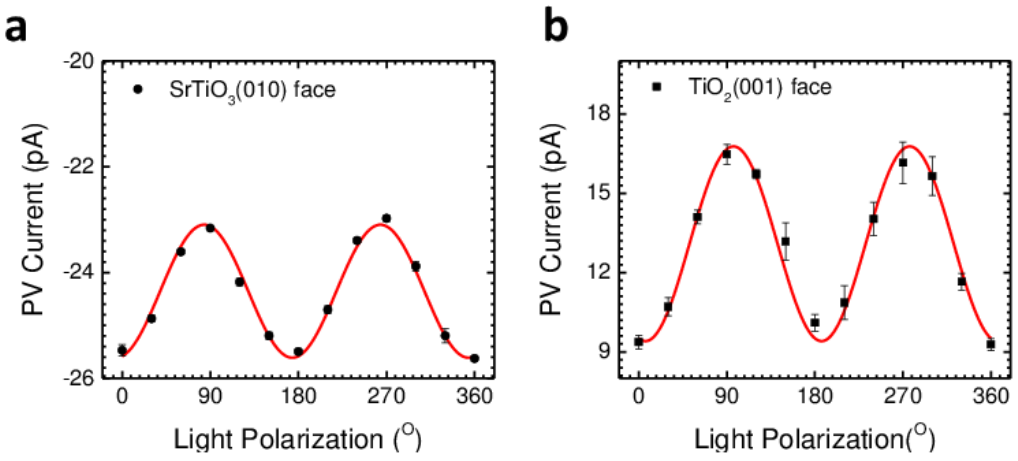

Figure 8-10. The sinusoidal dependence of the photocurrent measured on: (a) $SrTiO_3$ (010) face and (b) TiO_2 (001) face under 405 nm laser illumination. The red lines are the fitting with Eq. (8-28).

8.3.4 Flexo-photovoltaic Effect Induced by Micro-indenter

The FPV effect is neither confined to ionic crystals nor restricted to nanoscale geometries. Firstly, we performed the same experiment (as in Fig. 8-2) on an HF-passivated surface of a commercial *p*-type Si (001) crystal. Similarly, I_{SC} increases two

orders of magnitude, i.e. from a value as small as 5 pA with the 1 μN loading force to about 0.5 nA with the 15 μN loading force (Fig. 8-11). Secondly, the FPV effect could also be demonstrated using a home-built indentation system that deforms a semiconductor using a conductive tungsten probe needle with a radius of about 10 μm (Fig. 8-1c). Fig. 8-12a shows crystallographic orientation dependent photocurrent-voltage (*I-V*) characteristics of the $SrTiO_3$ crystal acquired under 4 N mechanical force exerted by the probe needle and 405 nm illumination directly to the probe contact area from the top side. These linear *I-V* characteristics are similar to those of ferroelectrics under illumination[9]. The oscillating PV current with the rotating incident light polarisation, which is well fitted with Eq. (8-28) in Fig. 8-12b**,** demonstrates again the FPV effect under the indentation force. The persistence of the FPV effect from the nanoscale (AFM) to the micrometer level provides promising feasibility for future device design and potential applications.

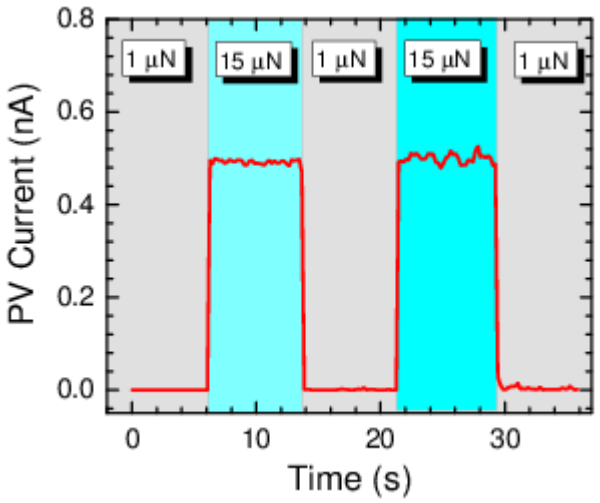

Figure 8-11. Force-induced photocurrent on (100) Si crystal measured by PhAFM under illumination of the top intended surface.

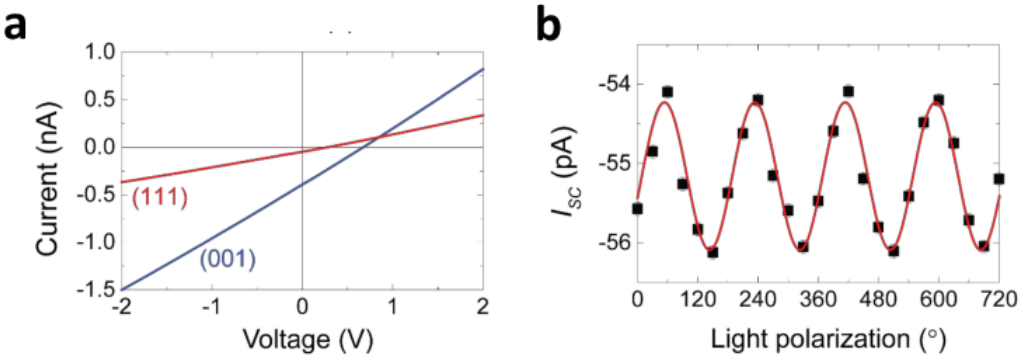

Figure 8-12. (a) Current-voltage characteristics measured on (001) and (111) faces of a $SrTiO_3$ crystal by the micro-indenter applying a 4 N force and illumination of the top intented surface. (b) The light polarisation dependence of the photocurrent on a $SrTiO_3$ (010) face measured by the micro-indenter under illumination on the side surface. The red line is the fitting of experimental data with Eq. (8-28). Because the polarisation angle origin of the micro-indenter is not coincident with the PhAFM setup, the oscillating I_{SC} has a phase shift compared with Fig. 8-10.

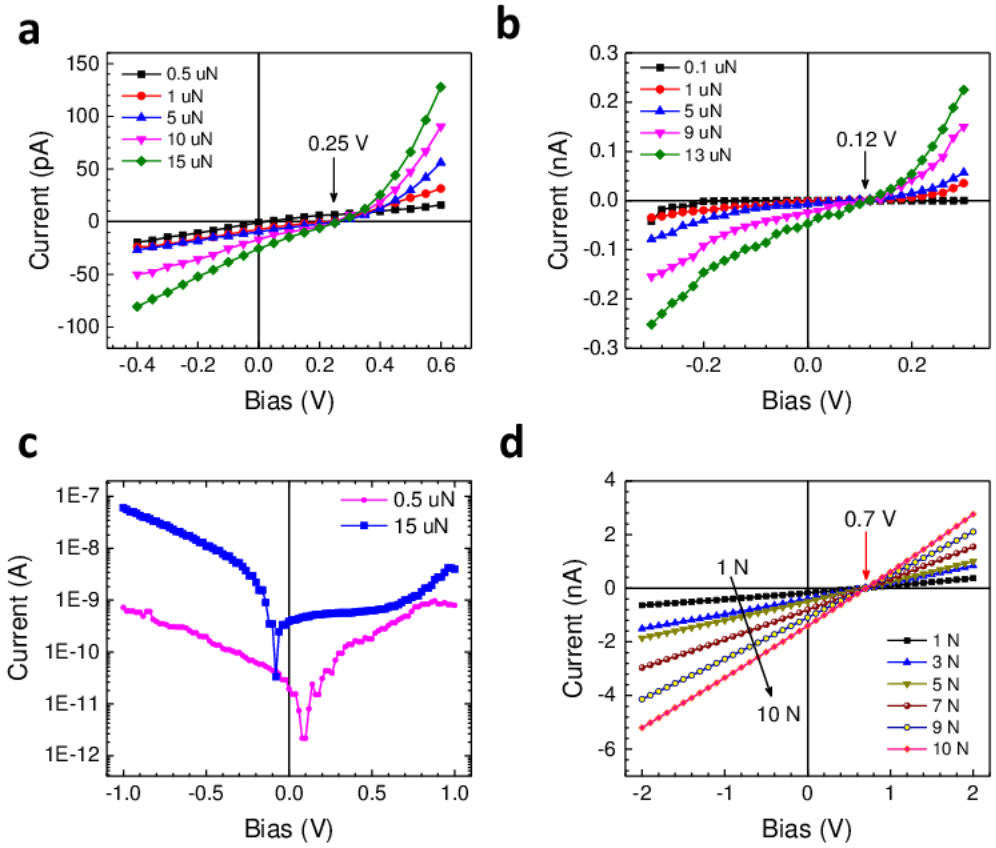

Figure 8-13. Current-voltage characteristics acquired by the conductive AFM tips under illumination with different load forces on (a) $SrTiO_3$ (001), (b) TiO_2 (100) and (c) Si (001) crystal surface. (d) Current-voltage curves acquired by a micro-probe indentation under different pressing forces on $SrTiO_3$ (001) crystal surface.

Being one of the crucial parameters in potential applications, it is important to study the open-circuit voltage (V_{OC}) of the FPV effect. The values of V_{OC} along with the photocurrent-voltage (*I-V*) characteristics acquired by the conductive AFM tip under various loading forces on both $SrTiO_3$ (001) and TiO_2 (100) crystals are shown in Fig. 8-13. When increasing the loading force exerted by the AFM tip, I_{SC} acquired on both $SrTiO_3$ (001) and TiO_2 (100) crystals is gradually enhanced whereas their V_{OC} remains almost constant with values of 0.25 V and 0.12 V, respectively. Similarly, the *I-V* curves acquired by the micro-probe indentation system on $SrTiO_3$ (001) crystal under increased pressing forces show a constant V_{OC} with increased I_{SC} (Fig. 8-13d). Additionally, the *I-V* curves of the Si (001) wafer is also given in Fig. 8-13c, which shows a small I_{SC} under the small loading force probably owing to the Schottky junction at the tip contact interface. When increasing the loading force up to 15 μN, I_{SC} turns to a large positive value. The small values of V_{OC}, which is inversely proportional to the conductivity, is probably due to the high photoconductivity of the studied crystals.

It should be also noted that the FPV effect is not related to a plasmonic effect found in the tip-enhanced Raman scattering because only an atomically sharp tip coated with Ag or Au shows the plasmonic enhancement in the visible range[157], whereas we used platinum and tungsten probes in the wide range of the nanoscale to the micrometer scale. Likewise, a potential cubic-to-tetragonal phase transition induced in $SrTiO_3$ under a large hydrostatic pressure (>6 GPa) should not play a large role here due to the centrosymmetric nature of the induced tetragonal phase[158].

8.3.5 Discussion

We emphasize here four main features of the FPV effect. First, the separation of the photoexcited carriers in the FPV effect is controlled by the local symmetry and thus the local BPV effect. As a consequence, the power conversion efficiency can in principle exceed the S-Q limit. Second, to obtain a high photocurrent from any semiconductor, only a strain gradient generator, such as a sharp probe with a sufficient loading force is necessary. This should be distinguished from the previous reports that a strain gradient modifies a bandgap, but the charge separation in the photoelectric process still requires a proper band alignment[159] or a nanostructure[159,160]. Third, whereas the BPV effect is allowed only in non-centrosymmetric materials, the FPV effect is universal. It is allowed by symmetry in all materials thanks to the universal nature of the strain-gradient-induced centrosymmetry breaking. FPV effect can be realized not only in ionic crystals ($SrTiO_3$ and TiO_2) and covalent crystals (Si), but is also relevant to any semiconductors ranging from organic-inorganic hybrid perovskites to semiconducting polymers and even topological insulators. For instance, Liu *et al*. reported for the first time that the topological insulator Bi_2Te_3 with a centrosymmetric structure exhibits the BPV effect by means of the flexoelectric effect[161]. Finally, given that the BPV effect consists of asymmetric quantum mechanical processes such as photoexcitation, relaxation, recombination, and scattering, we demonstrate that one can readily control the quantum mechanical processes by macroscopic tool such as an AFM tip and a probe needle.

The configuration of our photovoltaic indentation system is very simple and the FPV effect can be increasingly significant with decreasing material dimensions into the nanoscale, where flexoelectricity is more important[48]. Thus, an important strain engineering playground for improving the final performance of solar cells and optoelectronic devices is now open. For example, a new type of tandem solar cell can be easily fabricated by combining an array of indenters and a conventional *p*-*n* junction,

enabling a higher efficiency since the FPV effect can be designed to add to the existing PV current generated by the buried *p-n* junction. Given that the lattice mismatch at the interfaces and crystallographic disorders in epitaxial and polycrystalline thin film solar cells give rise to substantial strain gradients[162-164], the associated FPV effect would dramatically impact the performance of these solar cells, which however remains largely unknown. In addition to inorganic solar cells, the FPV effect is also likely to play an important role in flexible and stretchable electronics based on organic and polymeric semiconductors. Not only the bending of flexible organic devices at a macroscopic level[165] but also the folding and entanglement of the polymeric chains in a nanoscale level would generate sizable strain gradients[166], which redistribute the electron cloud of π-molecular orbits, modifying the electronic transport and inducing the FPV effect under illumination[151,167]. The detailed effects of strain gradient and FPV effect on the nanoscale electronic properties remain yet an open question and deserve in-depth investigations.

8.4 Conclusion

We proposed and demonstrated a new photovoltaic effect, namely the flexo-photovoltaic effect which originates from the local noncentrosymmetric structures induced by strain gradients. The flexo-photovoltaic effect separates photo-generated nonequilibrium carriers by asymmetric quantum mechanical processes, instead of the built-in electric field in conventional *p-n* junction solar cells. The flexo-photovoltaic effect is universally allowed in materials of all symmetry groups and advantageously combines the merits of both the existing BPV effect and the semiconductor PV effect, offering new insights and approaches to boost solar energy conversion efficiencies.

Chapter 9. Summary

In present thesis, the bulk photovoltaic effect and other photo-induced effects were studied to get further insight into the coupling between light and non-centrosymmetric structures as well as to enrich the photoferroelectric field. This thesis includes five separate works as summarised below.

The first two works presented in Chapters 4 and 5 relate to the fundamental issues about the bulk photovoltaic effect in $BiFeO_3$ and other ferroelectric materials, namely the electronic origin of the BPV effect and the correlation between the BPV effect and electric polarisation. It has been shown for the first time that the energy levels lying in the bandgap are at the electronic origin of the BPV effect in the bismuth ferrite. Also, the BPV effect is proven as an independent characteristic property of non-centrosymmetric crystals similar to the case of piezoelectricity, rather than induced by the ferroelectric polarisation. In addition, we have shown how to use the activity of sub-bandgap levels to tailor the ultimate performance of the BPV effect.

In Chapter 6, the electronic properties of domain walls in BFO thin films were probed by photoelectric atomic force microscopy to reveal their effective role in the transport of bulk photovoltaic current. We proved that the enhanced photoconductivity of domain walls can effectively facilitate the conduction of the BPV current.

Subsequently, optically induced reversible control of ferroelectric polarisation in BFO thin films was demonstrated in Chapter 7. The giant photocurrent density at the nanoscale tip contact area, which originates from the BPV effect, results in a giant electric field underneath the tip, enabling ferroelectric switching. By tuning the direction of the photocurrent at the tip contact area via two peculiarities of the BPV effect, respectively its dependence on non-centrosymmetric structure and light polarisation, the ferroelectric polarisation under the tip can be reversibly controlled by light.

Finally, in Chapter 8, we proposed and demonstrated a new photovoltaic effect, namely the flexo-photovoltaic effect which originates from the local noncentrosymmetric structures induced by strain gradients. This flexo-photovoltaic effect turns the BPV effect into a universal property allowed in materials of all symmetry groups. This discovery will start a new field of photoflexoelectrics and will largely broaden the scope of present photoferroelectrics.

As summarized above, this thesis covers a wide range of topics in the field of photoferroelectrics. Based on this thesis, several works can be further studied. Some of the examples are listed below.

The present thesis mainly focuses on the BPV effect manifested in the ferroelectric semiconductors while the photovoltaic effect originating from built-in electric field as in the Schottky junction between ferroelectrics and metallic electrodes is excluded. However, in reality, both photovoltaic effects coexist and function simultaneously in real ferroelectric devices under illumination, especially in ferroelectric capacitors. Thus, it is crucial to study the effective way to integrate these two photovoltaic effects in a single device to enhance solar energy conversion efficiency, which remains yet elusive.

Inspired by work on optically-induced ferroelectric switching in BFO, it possible to realize the optical control of multiple ferroic orders simultaneously at room temperature, providing a route to develop the optomagnetoelectric devices for remote control and data storage. Besides, the electric field associated with photocurrent density, of which value can be tuned over several orders of magnitude, will also generate large mechanical strains via either ferroelastic switching or converse piezoelectric effect, enabling the photostriction effect in the short-circuit conditions.

Regarding the flexo-photovoltaic effect, further works are needed to get fundamental insight into it. The first issue to be experimentally and theoretically resolved is the effect of strain gradient on the resultant non-centrosymmetric structure and the BPV effect, especially its tensorial coefficient. Another important issue in this field is the potential effect of the giant strain gradient existing at nanoscale length on the local electronic and photovoltaic effect, which is important in the thin film solar cells and nanoscale electronics.

Bibliography

1 Wadhawan, V. *Introduction to ferroic materials*. (CRC press, 2000).

2 Lines, M. E. & Glass, A. M. *Principles and applications of ferroelectrics and related materials*. (Oxford university press, 1977).

3 Uchino, K. *Ferroelectric Devices 2nd Edition*. (CRC press, 2009).

4 Spaldin, N. A., Cheong, S.-W. & Ramesh, R. Multiferroics: Past, present, and future. *Phys. Today* **63**, 38-43 (2010).

5 Spaldin, N. A. & Fiebig, M. The renaissance of magnetoelectric multiferroics. *Science* **309**, 391-392 (2005).

6 Cheong, S.-W. & Mostovoy, M. Multiferroics: a magnetic twist for ferroelectricity. *Nature Materials* **6**, 13 (2007).

7 Fridkin, V. M. *Ferroelectric Semiconductors*. (Consultants Bureau, 1980).

8 Kreisel, J., Alexe, M. & Thomas, P. A. A photoferroelectric material is more than the sum of its parts. *Nature Materials* **11**, 260 (2012).

9 Fridkin, V. M. *Photoferroelectrics*. Vol. 9 (Springer Science & Business Media, 2012).

10 Sturman, P. J. *Photovoltaic and Photo-refractive Effects in Noncentrosymmetric Materials*. Vol. 8 (CRC Press, 1992).

11 Yang, S. *et al.* Above-bandgap voltages from ferroelectric photovoltaic devices. *Nature Nanotechnology* **5**, 143-147 (2010).

12 Bhatnagar, A., Chaudhuri, A. R., Kim, Y. H., Hesse, D. & Alexe, M. Role of domain walls in the abnormal photovoltaic effect in $BiFeO_3$. *Nature Communications* **4** (2013).

13 Kundys, B., Viret, M., Colson, D. & Kundys, D. Light-induced size changes in BiFeO3 crystals. *Nature Materials* **9**, 803-805 (2010).

14 Valasek, J. Piezo-electric and allied phenomena in Rochelle salt. *Physical Review* **17**, 475 (1921).

15 Scott, J. Applications of modern ferroelectrics. *Science* **315**, 954-959 (2007).

16 Polla, D. L. & Francis, L. F. Processing and characterization of piezoelectric materials and integration into microelectromechanical systems. *Annual Review of Materials Science* **28**, 563-597 (1998).

17 Lang, S. B. Pyroelectricity: from ancient curiosity to modern imaging tool. *Physics Today* **58**, 31 (2005).

18 Garcia, V. & Bibes, M. Ferroelectric tunnel junctions for information storage and processing. *Nature Communications* **5**, 4289 (2014).

19 Chanthbouala, A. *et al.* A ferroelectric memristor. *Nature Materials* **11**, 860-864, doi:10.1038/nmat3415 (2012).

20 Garcia, V. *et al.* Giant tunnel electroresistance for non-destructive readout of ferroelectric states. *Nature* **460**, 81 (2009).

21 Warren, W. & Dimos, D. Photoinduced hysteresis changes and charge trapping in BaTiO3 dielectrics. *Applied Physics Letters* **64**, 866-868 (1994).

22 Sones, C. *et al.* Light-induced order-of-magnitude decrease in the electric field for domain nucleation in MgO-doped lithium niobate crystals. *Applied Physics Letters* **86**, 212901 (2005).

23 Gruverman, A., Rodriguez, B. J., Nemanich, R. & Kingon, A. Nanoscale observation of photoinduced domain pinning and investigation of imprint behaviour in ferroelectric thin films. *Journal of Applied Physics* **92**, 2734-2739 (2002).

24 Jiang, A. Q. *et al.* A resistive memory in semiconducting $BiFeO_3$ thin-film capacitors. *Advanced Materials* **23**, 1277-1281 (2011).

25 Hong, S. *et al.* Large resistive switching in ferroelectric $BiFeO_3$ nano-island based switchable diodes. *Advanced Materials* **25**, 2339-2343 (2013).

26 Seidel, J. *et al.* Conduction at domain walls in oxide multiferroics. *Nature Materials* **8**, 229 (2009).

27 Seidel, J. *et al.* Domain wall conductivity in La-doped $BiFeO_3$. *Physical Review Letters* **105**, 197603 (2010).

28 Catalan, G., Seidel, J., Ramesh, R. & Scott, J. F. Domain wall nanoelectronics. *Reviews of Modern Physics* **84**, 119 (2012).

29 Lee, J. H. *et al.* Spintronic functionality of $BiFeO_3$ domain walls. *Advanced Materials* **26**, 7078-7082 (2014).

30 Rakita, Y. *et al.* Tetragonal $CH_3NH_3PbI_3$ is ferroelectric. *Proceedings of the National Academy of Sciences*, 201702429 (2017).

31 Kojima, A., Teshima, K., Shirai, Y. & Miyasaka, T. Organometal halide perovskites as visible-light sensitizers for photovoltaic cells. *Journal of the American Chemical Society* **131**, 6050-6051 (2009).

32 Dong, Q. *et al.* Electron-hole diffusion lengths>175 μm in solution-grown $CH_3NH_3PbI_3$ single crystals. *Science* **347**, 967-970 (2015).

33 Wei, H. *et al.* Sensitive X-ray detectors made of methylammonium lead tribromide perovskite single crystals. *Nature Photonics* **10**, 333-339 (2016).

34 Rappe, A. M., Grinberg, I. & Spanier, J. E. Getting a charge out of hybrid perovskites. *Proceedings of the National Academy of Sciences*, 201708154 (2017).

35 Chynoweth, A. Surface space-charge layers in barium titanate. *Physical Review* **102**, 705 (1956).

36 Glass, A., Von der Linde, D. & Negran, T. Highvoltage bulk photovoltaic effect and the photorefractive process in $LiNbO_3$. *Applied Physics Letters* **25**, 233-235 (1974).

37 Yang, S. Y. *et al.* Above-bandgap voltages from ferroelectric photovoltaic devices. *Nature Nanotechnology* **5**, 143-147 (2010).

38 Pintilie, L. & Alexe, M. Metal-ferroelectric-metal heterostructures with Schottky contacts. I. Influence of the ferroelectric properties. *Journal of Applied Physics* **98**, 124103 (2005).

39 Blom, P., Wolf, R., Cillessen, J. & Krijn, M. Ferroelectric schottky diode. *Physical Review Letters* **73**, 2107 (1994).

40 Choi, T., Lee, S., Choi, Y., Kiryukhin, V. & Cheong, S.-W. Switchable ferroelectric diode and photovoltaic effect in $BiFeO_3$. *Science* **324**, 63-66 (2009).

41 Pintilie, L., Vrejoiu, I., Le Rhun, G. & Alexe, M. Short-circuit photocurrent in epitaxial lead zirconate-titanate thin films. *Journal of Applied Physics* **101**, 064109 (2007).

42 Lee, D. *et al.* Polarity control of carrier injection at ferroelectric/metal interfaces for electrically switchable diode and photovoltaic effects. *Physical Review B* **84**, 125305 (2011).

43 Spanier, J. E. *et al.* Power conversion efficiency exceeding the Shockley–Queisser limit in a ferroelectric insulator. *Nature Photonics* **10**, 611-616 (2016).

44 Gu, Z. *et al.* Mesoscopic Free Path of Nonthermalized Photogenerated Carriers in a Ferroelectric Insulator. *Physical Review Letters* **118**, 096601 (2017).

45 Ruppel, W., Von Baltz, R. & Wurfel, P. The origin of the photo-emf in ferroelectric and non-ferroelectric materials. *Ferroelectrics* **43**, 109-123 (1982).

46 Alexe, M. & Hesse, D. Tip-enhanced photovoltaic effects in bismuth ferrite. *Nature Communications* **2**, 256 (2011).

47 Alexe, M. Local mapping of generation and recombination lifetime in $BiFeO_3$ single crystals by scanning probe photoinduced transient spectroscopy. *Nano Letters* **12**, 2193-2198 (2012).

48 Zubko, P., Catalan, G. & Tagantsev, A. K. Flexoelectric effect in solids. *Annual Review of Materials Research* **43**, 387-421 (2013).

49 Tagantsev, A. Piezoelectricity and flexoelectricity in crystalline dielectrics. *Physical Review B* **34**, 5883 (1986).

50 Lu, H. *et al.* Mechanical writing of ferroelectric polarisation. *Science* **336**, 59-61 (2012).

51 Catalan, G. *et al.* Flexoelectric rotation of polarisation in ferroelectric thin films. *Nature Materials* **10**, 963-967 (2011).

52 Fousek, J., Cross, L. & Litvin, D. Possible piezoelectric composites based on the flexoelectric effect. *Materials Letters* **39**, 287-291 (1999).

53 Yang, J.-C., He, Q., Yu, P. & Chu, Y.-H. $BiFeO_3$ thin films: a playground for exploring electric-field control of multifunctionalities. *Annual Review of Materials Research* **45**, 249-275 (2015).

54 Kubel, F. & Schmid, H. Structure of a ferroelectric and ferroelastic monodomain crystal of the perovskite $BiFeO_3$. *Acta Crystallographica Section B: Structural Science* **46**, 698-702 (1990).

55 Bucci, J., Robertson, B. & James, W. The precision determination of the lattice parameters and the coefficients of thermal expansion of $BiFeO_3$. *Journal of Applied Crystallography* **5**, 187-191 (1972).

56 Shannon, R. D. Revised effective ionic radii and systematic studies of interatomic distances in halides and chalcogenides. *Acta crystallographica section A: crystal physics, diffraction, theoretical and general crystallography* **32**, 751-767 (1976).

57 Moreau, J.-M., Michel, C., Gerson, R. & James, W. J. Ferroelectric $BiFeO_3$ X-ray and neutron diffraction study. *Journal of Physics and Chemistry of Solids* **32**, 1315-1320 (1971).

58 Naganuma, H. in *Ferroelectrics Physical Effects* (InTech, 2011).

59 Lebeugle, D., Colson, D., Forget, A. & Viret, M. Very large spontaneous electric polarisation in $BiFeO_3$ single crystals at room temperature and its evolution under cycling fields. *Applied Physics Letters* **91**, 022907 (2007).

60 Shvartsman, V., Kleemann, W., Haumont, R. & Kreisel, J. Large bulk polarisation and regular domain structure in ceramic $BiFeO_3$. *Applied Physics Letters* **90**, 172115 (2007).

61 Wang, J. *et al.* Epitaxial $BiFeO_3$ multiferroic thin film heterostructures. *Science* **299**, 1719-1722 (2003).

62 Neaton, J. B., Ederer, C., Waghmare, U. V., Spaldin, N. A. & Rabe, K. M. First-principles study of spontaneous polarisation in multiferroic$BiFeO_3$. *Physical Review B* **71** (2005).

63 Cohen, R. E. Origin of ferroelectricity in perovskite oxides. *Nature* **358**, 136-138 (1992).

64 Seshadri, R. & Hill, N. A. Visualizing the role of Bi 6s “lone pairs” in the off-center distortion in ferromagnetic $BiMnO_3$. *Chemistry of Materials* **13**, 2892-2899 (2001).

65 Zhao, T. *et al.* Electrical control of antiferromagnetic domains in multiferroic $BiFeO_3$ films at room temperature. *Nature Materials* **5**, 823 (2006).

66 Kittel, C. Physical theory of ferromagnetic domains. *Reviews of Modern Physics* **21**, 541 (1949).

67 Giencke, J. E., Folkman, C. M., Baek, S.-H. & Eom, C.-B. Tailoring the domain structure of epitaxial $BiFeO_3$ thin films. *Current Opinion in Solid State and Materials Science* **18**, 39-45 (2014).

68 Chu, Y.-H. *et al.* Nanoscale control of domain architectures in $BiFeO_3$ thin films. *Nano Letters* **9**, 1726-1730 (2009).

69 Chu, Y. H. *et al.* Nanoscale Domain Control in Multiferroic $BiFeO_3$ Thin Films. *Advanced Materials* **18**, 2307-2311(2006).

70 Solmaz, A. *et al.* Domain Selectivity in $BiFeO_3$ Thin Films by Modified Substrate Termination. *Advanced Functional Materials* **26**, 2882-2889 (2016).

71 Chen, D. *et al.* Interface Engineering of Domain Structures in $BiFeO_3$ Thin Films. *Nano Letters* **17**, 486-493 (2017).

72 Chen, Z. *et al.* 180 degrees Ferroelectric Stripe Nanodomains in $BiFeO_3$ Thin Films. *Nano Letters* **15**, 6506-6513 (2015).

73 Folkman, C. M. *et al.* Stripe domain structure in epitaxial (001) BiFeO3 thin films on orthorhombic $TbScO_3$ substrate. *Applied Physics Letters* **94**, 251911(2009).

74 Nelson, C. T. *et al.* Spontaneous vortex nanodomain arrays at ferroelectric heterointerfaces. *Nano Letters* **11**, 828-834 (2011).

75 Bhatnagar, A. Electronic and Photoelectronic Processes in Multiferroic Materials. *PhD Thesis* (2014).

76 Catalan, G. & Scott, J. F. Physics and applications of bismuth ferrite. *Advanced Materials* **21**, 2463-2485 (2009).

77 Ederer, C. & Spaldin, N. A. Weak ferromagnetism and magnetoelectric coupling in bismuth ferrite. *Physical Review B* **71**, 060401 (2005).

78 Lebeugle, D. *et al.* Electric-field-induced spin flop in $BiFeO_3$ single crystals at room temperature. *Physical Review Letters* **100**, 227602 (2008).

79 Zvezdin, A. *et al.* Magnetoelectric interaction and magnetic field control of electric polarisation in multiferroics. *Journal of Magnetism and Magnetic Materials* **300**, 224-228 (2006).

80 Bai, F. *et al.* Destruction of spin cycloid in (111) c-oriented $BiFeO_3$ thin films by epitiaxial constraint: enhanced polarisation and release of latent magnetization. *Applied Physics Letters* **86**, 032511 (2005).

81 Eason, R. *Pulsed laser deposition of thin films: applications-led growth of functional materials*. (John Wiley & Sons, 2007).

82 Fewster, P. F. *X-Ray scattering from semiconductors and other materials*. (World Scientific, 2015).

83 Nye, J. F. & Lindsay, R. Physical properties of crystals. *Physics Today* **10**, 26 (1957).

84 Basu, S. *et al.* Photoconductivity in $BiFeO_3$ thin films. *Applied Physics Letters* **92**, 091905 (2008).

85 Koch, W., Munser, R., Ruppel, W. & Würfel, P. Anomalous photovoltage in $BaTiO_3$. *Ferroelectrics* **13**, 305-307 (1976).

86 Gunter, P. Photovoltages, photocurrents and photorefractive effects in $KNbO_3$: Fe. *Ferroelectrics* **22**, 671-674 (1978).

87 Young, S. M., Zheng, F. & Rappe, A. M. First-principles calculation of the bulk photovoltaic effect in bismuth ferrite. *Physical Review Letters* **109**, 236601 (2012).

88 Zhang, J. *et al.* Surface, bulk, and interface electronic states of epitaxial BiFeO 3 films. *Journal of Vacuum Science & Technology B: Microelectronics and Nanometer Structures Processing, Measurement, and Phenomena* **27**, 2012-2014 (2009).

89 Hauser, A. *et al.* Characterization of electronic structure and defect states of thin epitaxial $BiFeO_3$ films by UV-visible absorption and cathodoluminescence spectroscopies. *Applied Physics Letters* **92**, 222901 (2008).

90 Yamada, Y., Nakamura, T., Yasui, S., Funakubo, H. & Kanemitsu, Y. Measurement of transient photoabsorption and photocurrent of $BiFeO_3$ thin films: Evidence for long-lived trapped photocarriers. *Physical Review B* **89**, 035133 (2014).

91 Yi, H., Choi, T., Choi, S., Oh, Y. S. & Cheong, S. W. Mechanism of the switchable photovoltaic effect in ferroelectric $BiFeO_3$. *Advanced Materials* **23**, 3403-3407 (2011).

92 Moubah, R. *et al.* Photoelectric effects in single domain $BiFeO_3$ crystals. *Advanced Functional Materials* **22**, 4814-4818 (2012).

93 Ji, W., Yao, K. & Liang, Y. C. Bulk photovoltaic effect at visible wavelength in epitaxial ferroelectric $BiFeO_3$ thin films. *Advanced Materials* **22**, 1763-1766 (2010).

94 Kubel, F. & Schmid, H. Growth, twinning and etch figures of ferroelectric/ferroelastic dendritic $BiFeO_3$ single domain crystals. *Journal of Crystal Growth* **129**, 515-524 (1993).

95 Kundys, B. *et al.* Wavelength dependence of photoinduced deformation in $BiFeO_3$. *Physical Review B* **85**, 092301 (2012).

96 DeVore, H. B. Spectral distribution of photoconductivity. *Physical Review* **102**, 86 (1956).

97 Wen, H. *et al.* Electronic origin of ultrafast photoinduced strain in $BiFeO_3$. *Physical Review Letters* **110**, 037601 (2013).

98 Sheu, Y. *et al.* Ultrafast carrier dynamics and radiative recombination in multiferroic $BiFeO_3$. *Applied Physics Letters* **100**, 242904 (2012).

99 Rose, A. Recombination processes in insulators and semiconductors. *Physical Review* **97**, 322 (1955).

100 Mikla, V. V. & Mikla, V. I. *Trap level spectroscopy in amorphous semiconductors*. (Elsevier, 2010).

101 Lee, D. *et al.* Polarity control of carrier injection at ferroelectric/metal interfaces for electrically switchable diode and photovoltaic effects. *Physical Review B* **84** (2011).

102 Fridkin, V. & Sturman, B. The photovoltaic and photorefractive effects in noncentrosymmetric Materials. *Gordon & Breach* (1992).

103 Yang, M., Bhatnagar, A. & Alexe, M. Electronic Origin and Tailoring of Photovoltaic Effect in $BiFeO_3$ Single Crystals. *Advanced Electronic Materials* **1** (2015).

104 Spanier, J. E. *et al.* Power conversion efficiency exceeding the Shockley–Queisser limit in a ferroelectric insulator. *Nature Photonics* **10**, 611 (2016).

105 Seidel, J. *et al.* Efficient photovoltaic current generation at ferroelectric domain walls. *Physical Review Letters* **107**, 126805 (2011).

106 Yang, M.-M., Bhatnagar, A., Luo, Z.-D. & Alexe, M. Enhancement of Local Photovoltaic Current at Ferroelectric Domain Walls in $BiFeO_3$. *Scientific Reports* **7**43070 (2017).

107 Catalan, G., Seidel, J., Ramesh, R. & Scott, J. F. Domain wall nanoelectronics. *Reviews of Modern Physics* **84**, 119-156 (2012).

108 Baek, S. *et al.* Ferroelastic switching for nanoscale non-volatile magnetoelectric devices. *Nature Materials* **9**, 309-314 (2010).

109 Paudel, T. R., Jaswal, S. S. & Tsymbal, E. Y. Intrinsic defects in multiferroic BiFeO3and their effect on magnetism. *Physical Review B* **85** (2012).

110 Yoneda, Y., Kitanaka, Y., Noguchi, Y. & Miyayama, M. Electronic and local structures of Mn-doped $BiFeO_3$ crystals. *Physical Review B* **86**, 184112 (2012).

111 Seidel, J. *et al.* Conduction at domain walls in oxide multiferroics. *Nature Material* **8**, 229-234 (2009).

112 Seidel, J. *et al.* Domain wall conductivity in La-doped $BiFeO_3$. *Phys Rev Lett* **105**, 197603 (2010).

113 Farokhipoor, S. & Noheda, B. Conduction through 71 degrees domain walls in $BiFeO_3$ thin films. *Phys Rev Lett* **107**, 127601 (2011).

114 Sluka, T., Tagantsev, A. K., Bednyakov, P. & Setter, N. Free-electron gas at charged domain walls in insulating $BaTiO_3$. *Nature Communication* **4**, 1808 (2013).

115 Daraktchiev, M., Catalan, G. & Scott, J. F. Landau theory of domain wall magnetoelectricity. *Physical Review B* **81**, 224118 (2010).

116 Jesse, S. *et al.* Direct imaging of the spatial and energy distribution of nucleation centres in ferroelectric materials. *Nature Materials* **7**, 209-215 (2008).

117 Xu, R., Karthik, J., Damodaran, A. R. & Martin, L. W. Stationary domain wall contribution to enhanced ferroelectric susceptibility. *Nature Communications* **5**, 3120 (2014).

118 Karthik, J., Agar, J., Damodaran, A. & Martin, L. Effect of 90 domain walls and thermal expansion mismatch on the pyroelectric properties of epitaxial $PbZr_{0.2}Ti_{0.8}O_3$ thin films. *Physical Review Letters* **109**, 257602 (2012).

119 Bhatnagar, A., Roy Chaudhuri, A., Heon Kim, Y., Hesse, D. & Alexe, M. Role of domain walls in the abnormal photovoltaic effect in $BiFeO_3$. *Nature Communications* **4**, 3835 (2013).

120 Fridkin, V. Bulk photovoltaic effect in noncentrosymmetric crystals. *Crystallography Reports* **46**, 654-658 (2001).

121 Reznik, L., Anikiev, A., Umarov, B. & Scott, J. Studies of optical damage in lithium niobate in the presence of thermal gradients. *Ferroelectrics* **64**, 215-219 (1985).

122 Borkar, H. *et al.* Novel optically active lead-free relaxor ferroelectric $(Ba_{0.6}Bi_{0.2}Li_{0.2})TiO_3$. *Journal of Physics: Condensed Matter* **28**, 265901 (2016).

123 Ji, W., Yao, K. & Liang, Y. C. Evidence of bulk photovoltaic effect and large tensor coefficient in ferroelectric $BiFeO_3$ thin films. *Physical Review B* **84**, 094115 (2011).

124 Buse, K. Light-induced charge transport processes in photorefractive crystals I: Models and experimental methods. *Applied Physics B: Lasers and Optics* **64**, 273-291 (1997).

125 Chiu, Y. P. *et al.* Atomic Scale Evolution of Local Electronic Structure Across Multiferroic Domain Walls. *Advanced Materials* **23**, 1530-1534 (2011).

126 Xiao, Y., Shenoy, V. B. & Bhattacharya, K. Depletion layers and domain walls in semiconducting ferroelectric thin films. *Physical Review Letters* **95**, 247603 (2005).

127 Eliseev, E. A., Morozovska, A. N., Svechnikov, G. S., Maksymovych, P. & Kalinin, S. V. Domain wall conduction in multiaxial ferroelectrics. *Physical Review B* **85**, 045312 (2012).

128 Lampert, M. A. & Mark, P. *Current Injection in Solids*. (Academic Press, 1970).

129 Lambert, C.-H. *et al.* All-optical control of ferromagnetic thin films and nanostructures. *Science* **345**, 1337-1340 (2014).

130 Stanciu, C. *et al.* All-optical magnetic recording with circularly polarized light. *Physical Review Letters* **99**, 047601 (2007).

131 Duong, N. P., Satoh, T. & Fiebig, M. Ultrafast manipulation of antiferromagnetism of NiO. *Physical Review Letters* **93**, 117402 (2004).

132 Manz, S. *et al.* Reversible optical switching of antiferromagnetism in $TbMnO_3$. *Nature Photonics* **10**, 653-656 (2016).

133 van der Ziel, J. P., Pershan, P. S. & Malmstrom, L. D. Optically-Induced Magnetization Resulting from the Inverse Faraday Effect. *Physical Review Letters* **15**, 190-193 (1965).

134 Steigerwald, H. *et al.* Direct writing of ferroelectric domains on the x-and y-faces of lithium niobate using a continuous wave ultraviolet laser. *Applied Physics Letters* **98**, 062902 (2011).

135 Boes, A. *et al.* Direct writing of ferroelectric domains on strontium barium niobate crystals using focused ultraviolet laser light. *Applied Physics Letters* **103**, 142904 (2013).

136 Hadni, A. & Thomas, R. Localized irreversible thermal switching in ferroelectric TGS by an argon laser. *Ferroelectrics* **6**, 241-245 (1973).

137 Steigerwald, H. *et al.* Origin of UV-induced poling inhibition in lithium niobate crystals. *Physical Review B* **82** (2010).

138 Yang, M.-M. *et al.* Bulk photovoltaic effect in monodomain $BiFeO_3$ thin films. *Applied Physics Letters* **110**, 183902 (2017).

139 Nakashima, S., Takayama, K., Shigematsu, K., Fujisawa, H. & Shimizu, M. Growth of epitaxial Mn and Zn codoped $BiFeO_3$ thin films and an enhancement of photovoltage generated by a bulk photovoltaic effect. *Japanese Journal of Applied Physics* **55**, 10TA07 (2016).

140 Sze, S. M. & Ng, K. K. *Physics of Semiconductor Devices*. (John wiley & sons, 2006).

141 Shafer, P. *et al.* Planar electrode piezoelectric force microscopy to study electric polarisation switching in $BiFeO_3$. *Applied Physics Letters* **90**, 202909 (2007).

142 Lampert, M., Many, A. & Mark, P. Space-charge-limited currents injected from a point contact. *Physical Review* **135**, A1444 (1964).

143 Chu, Y.-H. *et al.* Electric-field control of local ferromagnetism using a magnetoelectric multiferroic. *Nature Materials* **7**, 478-482 (2008).

144 Heron, J. *et al.* Deterministic switching of ferromagnetism at room temperature using an electric field. *Nature* **516**, 370-373 (2014).

145 Koch, W., Munser, R., Ruppel, W. & Würfel, P. Bulk photovoltaic effect in $BaTiO_3$. *Solid State Communications* **17**, 847-850 (1975).

146 Shockley, W. & Queisser, H. J. Detailed balance limit of efficiency of p-n junction solar cells. *Journal of Applied Physics* **32**, 510-519 (1961).

147 Tagantsev, A. K. Piezoelectricity and flexoelectricity in crystalline dielectrics. *Physical Review B* **34**, 5883-5889 (1986).

148 Zubko, P., Catalan, G. & Tagantsev, A. K. Flexoelectric Effect in Solids. *Annual Review of Materials Research* **43**, 387-421 (2013).

149 Breneman, K. D., Brownell, W. E. & Rabbitt, R. D. Hair cell bundles: flexoelectric motors of the inner ear. *PLoS One* **4**, e5201 (2009).

150 Bhaskar, U. K. *et al.* A flexoelectric microelectromechanical system on silicon. *Nature Nanotechnology* **11**, 263-266 (2016).

151 Kalinin, S. V. & Meunier, V. Electronic flexoelectricity in low-dimensional systems. *Physical Review B* **77**, 033403 (2008).

152 Očenášek, J. *et al.* Nanomechanics of flexoelectric switching. *Physical Review B* **92** (2015).

153 Lu, H. *et al.* Mechanical writing of ferroelectric polarisation. *Science* **336**, 59-61 (2012).

154 Zubko, P., Catalan, G., Buckley, A., Welche, P. R. & Scott, J. F. Strain-gradient-induced polarisation in $SrTiO_3$ single crystals. *Physical Review Letters* **99**, 167601 (2007).

155 Yang, M. M., Bhatnagar, A., Luo, Z. D. & Alexe, M. Enhancement of Local Photovoltaic Current at Ferroelectric Domain Walls in $BiFeO_3$. *Scientific Reports* **7**, 43070 (2017).

156 Fischer-Cripps, A. C. *Introduction to Contact Mechanics*. (Springer, 2000).

157 Sonntag, M. D., Pozzi, E. A., Jiang, N., Hersam, M. C. & Van Duyne, R. P. Recent advances in tip-enhanced Raman spectroscopy. *The Journal of Physical Chemistry Letters* **5**, 3125-3130 (2014).

158 Guennou, M., Bouvier, P., Kreisel, J. & Machon, D. Pressure-temperature phase diagram of $SrTiO_3$ up to 53 GPa. *Physical Review B* **81**, 054115 (2010).

159 Feng, J., Qian, X., Huang, C.-W. & Li, J. Strain-engineered artificial atom as a broad-spectrum solar energy funnel. *Nature Photonics* **6**, 866-872 (2012).

160 Greil, J., Birner, S., Bertagnolli, E. & Lugstein, A. Nanowires enabling strained photovoltaics. *Applied Physics Letters* **104**, 163901 (2014).

161 Liu, Y. *et al.* Bulk photovoltaic effect at infrared wavelength in strained Bi_2Te_3 films. *APL Materials* **4**, 126104 (2016).

162 Bennett, M. S. & Kramer, J. J. The effect of piezoelectrically coupled stresses on the junction characteristics of CdS-Cu_2S solar cells. *Journal of Applied Physics* **54**, 7159-7165 (1983).

163 Lee, D. *et al.* Giant flexoelectric effect in ferroelectric epitaxial thin films. *Physical Review Letters* **107**, 057602 (2011).

164 Ming-Wen, C. *et al.* Impact of misfit dislocations on the polarisation instability of epitaxial nanostructured ferroelectric perovskites. *Nature Materials* **3**, 87 (2004).

165 Reyes-Martinez, M. A., Crosby, A. J. & Briseno, A. L. Rubrene crystal field-effect mobility modulation via conducting channel wrinkling. *Nature Communications* **6**, 6948 (2015).

166 Tang, Q. *et al.* Organic nanowire crystals combine excellent device performance and mechanical flexibility. *Small* **7**, 189-193 (2011).

167 Dumitrică, T., Landis, C. M. & Yakobson, B. I. Curvature-induced polarisation in carbon nanoshells. *Chemical Physics Letters* **360**, 182-188 (2002).